

Kinetic modeling of coronal loops and wave-particle interactions

Dissertation
zur Erlangung des Doktorgrades
der Mathematisch-Naturwissenschaftlichen Fakultäten
der Georg-August-Universität zu Göttingen

vorgelegt von
Sofiane Bourouaine
aus Constantine, Algerien

Göttingen 2009

Bibliografische Information Der Deutschen Bibliothek

Die Deutsche Bibliothek verzeichnet diese Publikation in der Deutschen Nationalbibliografie; detaillierte bibliografische Daten sind im Internet über <http://dnb.ddb.de> abrufbar.

D7

Referent: Prof. Dr. Wolfgang Glatzel

Korreferent: Prof. Dr. Eckart Marsch

Tag der mündlichen Prüfung: 13.02.2009

ISBN 978-3-936586-99-2

Copernicus Publications 2009

<http://publications.copernicus.org>

© Sofiane Bourouaine

Printed in Germany

Contents

1	General introduction	7
1.1	The solar corona	7
1.1.1	Collisional coronal heating mechanism	15
1.1.2	Collisionless heating mechanism	18
1.2	Coronal loops	21
1.2.1	Coronal loop observations	21
1.2.2	Expansion of coronal loops	22
1.2.3	Nanoflare model for coronal loop	25
1.3	Motivations and outlines of the present thesis work	26
2	Proton heating by oblique fast waves	27
2.1	Introduction	27
2.2	Magnetized dispersion relation	28
2.2.1	General dispersion function	28
2.2.2	Dispersion relation for a bi-Maxwellian VDFs	30
2.3	Oblique fast waves in electron/proton plasma	32
2.3.1	Linear dispersion analysis	32
2.3.2	Quasi-linear theory for reduced VDF	34
2.3.3	Proton heating by oblique fast waves	39
2.4	Conclusion	41
3	On the efficiency of nonresonant ion heating by coronal Alfvén waves	45
3.1	Introduction	45
3.2	Observation of Coronal MHD Alfvén waves	46
3.3	Ion heating by Alfvén waves (test-particle simulation)	48
3.4	Nonresonant wave-particle diffusion	50
3.5	Heating of a collisionless multi-ions plasma	52
3.6	Heating of the collisional lower corona	55
3.7	Conclusion	62
4	Coronal loop model including ion kinetics	63
4.1	Introduction	63
4.2	The model description	64
4.2.1	Coronal loop geometry	64
4.2.2	Theory	66
4.3	Numerical method	69

Contents

4.4	Simulation results	73
4.4.1	General remarks	73
4.4.2	Asymmetric heating	74
4.4.3	Symmetric heating	80
4.5	Conclusion and discussion	84
5	Multi-ions kinetic model for coronal loop	87
5.1	Introduction	87
5.2	Results	88
5.2.1	Plasma loop profiles	88
5.2.2	Wave-absorption mechanism	90
5.2.3	Ion VDFs in case of $\Gamma = 1.48$	91
5.3	Conclusion and discussion	92
6	Multi-strand loop modeling and filter-ratio analysis	99
6.1	Introduction:	99
6.2	Multi-strand coronal loop model:	101
6.3	Filter-ratio analysis:	103
6.4	Conclusion	112
7	Conclusion and outlook	115
	Bibliography	119
	Acknowledgements	129
	Lebenslauf	131

Summary

The solar corona is tenuous, multi-component, weakly collisional and thus mostly not at LTE (Local Thermodynamic Equilibrium). Therefore, it is ideally suited for applying kinetic description of the plasma rather than using the single fluid approach. Recent UVCS observations revealed that the heavy ions are preferentially heated in coronal holes. Furthermore, evidence that the local O^{+5} velocity distribution is anisotropic has been found. These results are interpreted as a signature of the heating by resonant wave-particle interactions, where the ion-cyclotron waves are expected to heat the ions perpendicularly (with respect to the mean magnetic field). This heating mechanism is a fully kinetic process and has nothing to do with the collisional heating mechanism described within the single fluid approach. Therefore, we believe that the microphysics of the solar corona has to be involved in the study of the coronal heating problem. Furthermore, the collisions in the solar corona are not strong enough to provide an efficient heating through the classical Ohmic dissipation or via the damping of the large-scale MHD waves. Moreover, to obtain the necessary heating from the classical collision coefficients, we need very steep variations in the plasma parameters (e.g. the plasma temperature or density) or in the magnetic field. Unfortunately, these needed gradient scales are less or comparable to the mean free path of the collisions.

In the most collisional conditions of the plasma (e.g., in the upper chromosphere), the maximum heating rate that can be provided by the collisional Ohmic dissipation is six order of magnitude less than the cooling rate caused by the radiation.

Therefore, we believe that wave-particle interactions play a major role in the heating of the solar corona. In this mechanism, the small-scale fluctuations can dissipate via a fully kinetic process, whereas the collisions do not play any role in the conversion of the magnetic energy into heat. In such process, the waves having wavelengths much smaller than the MHD scales can dissipate via resonant or nonresonant wave-particle interactions and heat the particles. The nonresonant heating is a slow process, and it is related to the dissipation of waves having frequencies much smaller than the ion gyrofrequency. While the resonant heating is faster (their time scale is close to the ion gyroperiod), and it is subjected to the damping of waves having frequencies close to the ion gyrofrequency (also called ion-cyclotron waves) via ion-cyclotron resonance.

In coronal holes (open structures), the preferential heating and the temperature anisotropy observed in heavy ion distributions can be well reproduced when one assumes heating through the dissipation of ion-cyclotron waves. These waves are assumed to be excited from small-scale reconnection events in the chromosphere, and thus provide the ultimate source for the ion heating. This wave-generation mechanism occurs when many of low-lying closed field lines in the chromosphere are entangled with oppositely directed open field lines, and while reconnecting release fluctuations having scales smaller than MHD scales. Thus waves can dissipate via collisionless kinetic processes and heat the solar corona. In coronal loops (closed structures) the density is higher, and thus the collisions are relatively stronger than in coronal holes. Therefore, if the ions are heated through ion-cyclotron resonance, also the electrons can be heated through ion-electron collisions.

TRACE/SXT observations have shown that the coronal loops can be heated to a few of million kelvins. These closed structures, which are one of the basic components of the lower corona, are brighter than the surrounding plasmas. It has been found that the

warm coronal loops (having $T \sim 1.3$ MK) have roughly a flat temperature profile along their lengths, when the isothermality across the loops is assumed, while the hotter coronal loops are uniformly heated, and mostly they are in hydrostatic equilibrium. There is no decisive answer if the closed and the open structures in the solar corona can be heated by a similar heating process. By adopting the resonant wave-particle interactions as a possible heating mechanism for the coronal loop, a relationship can be obtained between the expansion of the coronal-loop flux-tube and the heating profile along the loop. It is found, from the semi-kinetic model, that the flat temperature profile and the enhanced density in the coronal loop is a consequence of a quasi-homogeneous loop cross-section, whilst a uniform heating profile in the loop can be achieved when the loop flux tube expands from the loop footpoints to the loop top.

On the other hand, there are other spectroscopic loop observations show that the coronal loops are not isothermal along the line-of-sight (they have broad differential emission measures (DEM)), and thus the temperature and the density profiles of the coronal loop often inferred from the filter ratios of imagers are misleading. Indeed, from a multi-strand coronal loop model, when we assume that the coronal loop is composed of small-scale filaments having different temperatures, the loop temperature, as extracted from the filter-ratio technique, is roughly constant along the loop, and its value is biased to be ~ 1.2 MK.

1 General introduction

1.1 The solar corona

The visible solar atmosphere consists of three regions: the photosphere, the chromosphere, and the solar corona. Most of the visible (white) light comes from the photosphere, this is the part of the Sun we actually see. The corona is the sun's outer atmosphere which is viewed above a certain height or above a certain temperature. It can clearly be seen during the total solar eclipse as a bright region that extends more than some solar radii away from the disk of the sun (see Fig. 1.1). The coronal temperature can reach some million kelvins according to analysis of the optical lines originating from highly ionized atoms in corona. These high coronal temperatures were first confirmed in 1946 by the discovery of thermal radio emission at meter waves. Before that, in 1942, Edlén identified forbidden lines of highly ionized atoms and this way established for the first time the million-degree temperature of the corona.

The solar corona is usually subdivided into three zones, which all vary in their sizes

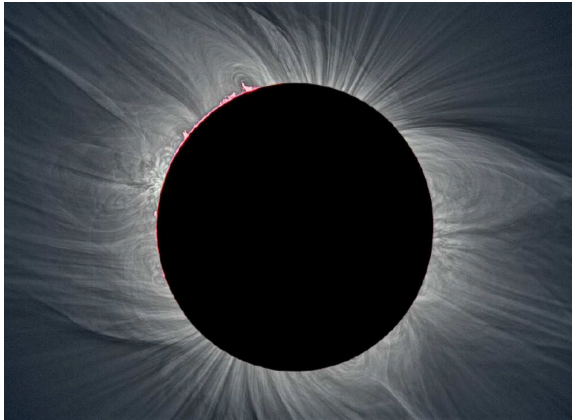


Figure 1.1: This image is a composition of 60 images taken with Canon EOS 5D with 1640 mm lens. The position of the Moon represents the situation 15 seconds after the second contact. Pasachoff et al. (2006)

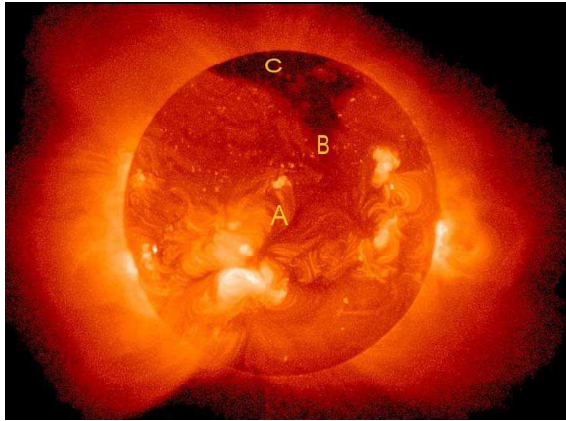


Figure 1.2: Soft X-ray image of the extended solar corona recorded on 26 August 1992 by the Yohkoh Soft X-ray Telescope (SXT). (Courtesy of Yokoh Team)

during the solar cycle: (1) active regions, (2) quiet Sun regions, and (3) coronal holes (See Fig. 1.2).

(1) The active regions (regions A in Fig. 1.2) which make up only a small fraction of the total surface area, are located in areas of strong magnetic field concentrations, also the active regions are connected to the visible sunspot groups in optical wavelengths or magnetograms at the solar surface. A number of dynamic processes such as plasma heating, flares, and coronal mass ejections occur in active regions. Also, in these regions, there is plasma heating in the chromosphere and upflows into coronal loops that are hot and dense.

(2) Quiet Sun (regions B in Fig. 1.2) are the remaining areas outside of active regions. Many dynamic processes may occur in these region, ranging from small-scale phenomena such as network heating events, nanoflares, explosive events, bright points, soft X-ray jets, to large-scale structures, such as transequatorial loops, or coronal arches.

(3) Coronal Holes (regions C in Fig. 1.2) are situated in the northern and southern polar zones of the solar globe. They have generally been found to be darker than the equatorial zones during solar eclipses, and also are the main source of the solar wind. It is fairly clear that these zones are dominated by open magnetic field lines. Because of this efficient transport mechanism, coronal holes contain less plasma most of the time, and thus appear much darker than the Quiet Sun.

The observation of the solar corona

The corona can be observed of corona in different wave-lengths; soft X-rays, ultraviolet lines, optical, and radio waves. The corona emits highly energetic photons (having energies from 0.1 to 10 keV) in the form of soft X-rays and EUV line emissions. Since the

lower atmosphere is cooler than the corona, the lower atmosphere appears as a dark background in the coronal X-ray emission shown in Fig. 1.2. The emission includes both a continuum emitted by free electrons and lines from highly ionized ions. The bright structures outline magnetic loops of high density (typically 10^9 cm^{-3}) and high temperature ($2-3.5 \times 10^6 \text{ K}$). Also the coronal plasma emits thermal radio waves by two physically different mechanisms. One of the dominant processes is "bremsstrahlung emission" of free energetic electrons making collisions with other electrons or ions. The other process may arise in active regions where the enhanced magnetic field strength increases the gyration frequency of electrons in the field (see book of Benz 2003). This makes the so-called "gyroresonance emission" dominates the thermal radiation process between roughly 3 GHz to 15 GHz. This process opens a possibility to measure the coronal magnetic field. High-frequency bremsstrahlung originates usually at high density in the atmosphere. Similarly, the intensity of gyroresonance emission is mainly proportional to the higher magnetic fields strength. Thus, thermal high-frequency sources are generally found at low altitudes in corona.

The solar corona is complex medium that contains many structures having different scales. Below we list the main structures that characterizes the corona;

Helmet Streamers (see Fig. 1.3a): streamers originate at the solar surface, typically in the bright places in the active regions, and they are outwardly directed and extend within large radial range far from the solar surface (a few tenth of a solar radius above the limb at nearly mid-latitudes). Their lower part contains some complex structures of closed field lines crossing a neutral line. Above the helmet, a long, straight, near-radial stalk continues outward into the heliosphere, containing plasma that leaks out from the top of the helmet where the thermal pressure starts to overcome the magnetic confinement.

Loop Arcades (see Fig. 1.3b): They form the basic structure of the lower corona and transition region of the Sun. They are a direct consequence of the twisted solar magnetic flux within the solar body. The bright appearance of such loops is mostly linked with the solar cycle, and for that reason they are often found with sunspots at their footpoints.

Soft X-ray Jets (see Fig. 1.3c): The polar coronal jets were first observed by SOHO instruments (EIT, LASCO, UVCS) during the last solar minimum. They were small, fast ejections originating from flaring UV bright points within large polar coronal holes. They are heated plasma flows constraint by open field lines. Such jet features are visible until the flow fades out or the structure erupts.

Postflare loops (see Fig. 1.3d): Are visible in soft X-rays after the chromospheric evaporation process. Flare (or postflare) loops trace out dipole-like magnetic field lines, after relaxation from flare-related magnetic reconnection processes.

Also there are other structures having different magnetic field configurations, can appear in the corona like : Cusp-shaped loops which have loop-like structure with a pointed shape at the top (see Fig. 1.3e). Also, multiple arcades (see Fig. 1.3f) which arise from multiple neutral lines occur in active regions, that organize the magnetic field into multiple arcades side-by-side.

Magnetic field of the solar corona

The nature of the structures of the outer atmosphere seems to be intimately linked to the magnetic fields at the surface. Dynamo theory predicts that strong magnetic fields are

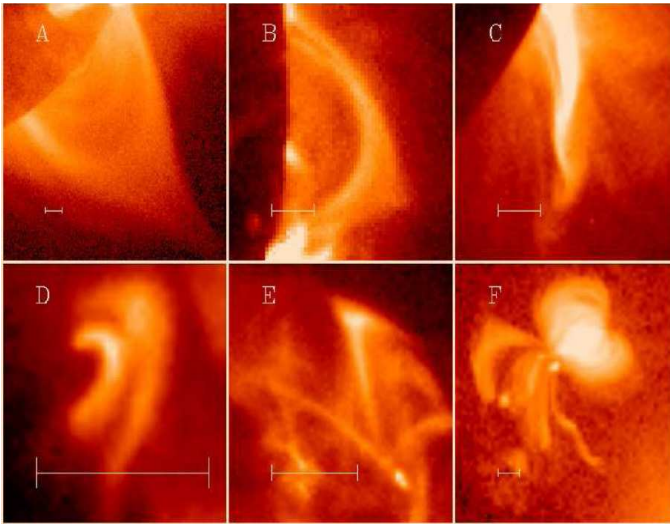


Figure 1.3: (A) Large helmet-type structure; (B) arcade of X-ray loops seen end-on; (C) dynamic eruptive feature which grew at a velocity of about 30 km s^{-1} ; (D) a pair of small symmetrical flaring loops; (E) two cusped loops with heating in the northern loop; (F) a tightly beamed X-ray jet towards the southwest at 200 km s^{-1} . (Acton et al. 1992, Aschwanden 2004).

generated deep in the solar interior, and then the bundles of magnetic flux will float to the surface. The structure created by the field emergence is rooted in the photosphere and extends through the chromosphere and transition region to the corona. The areas where the bundle of field lines related to the coronal structures leaves and reenters the visible surface are generally called the "footpoints".

The strongest magnetic field regions at the surface are in sunspots, at which the field strengths can be in the order of $B = 2000\text{--}3000 \text{ G}$. Sunspot groups are dipolar and slightly closer to the equator, and their strong appearance is reversing every 11-year cycle. Active regions are linked to a larger area around the sunspots, with typical photospheric fields of $B \approx 100\text{--}500 \text{ G}$ (see Fig. 1.4). In the Quiet Sun and in coronal holes, the background magnetic field is of the order of $B = 5\text{--}10 \text{ G}$. The determination of the coronal magnetic field is reconstructed by extrapolation from magnetograms at the lower boundary, using a potential-field or force-free field model (see Fig. 1.5).

In the solar corona, the magnetic pressure mainly dominates the gas pressure especially at lower altitudes (below 1 solar radius), consequently the plasma is generally confined within the magnetic fields that constitutes the structure of the corona. Therefore, it is widely believed that the plasma intensities that appear in some regions in corona trace the magnetic field lines existing in these regions. This is because, in the corona, the magnetic

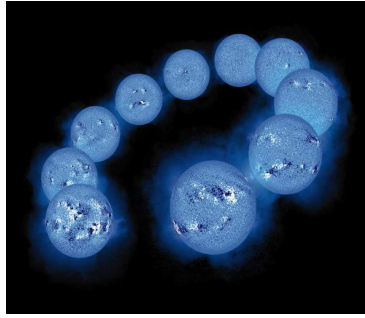


Figure 1.4: The photospheric magnetograms from 1992 January 8 to 1999 July 25, recorded with the Vacuum Telescope of the National Solar Observatory (NSO) at Kitt Peak National Observatory (KPNO), Tucson, Arizona. White and black colours indicate positive and negative magnetic polarity. (courtesy of KPNO).

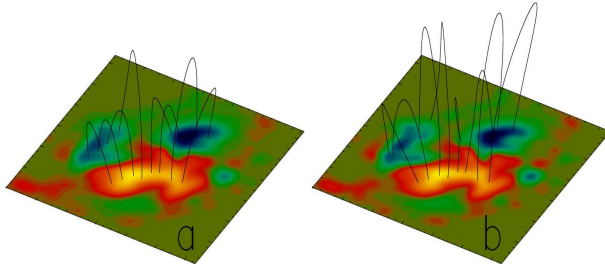


Figure 1.5: AR 7321 measured with SFT-data from October, 26 1992. (a) Potential field reconstruction. (b) Non-linear force-free reconstruction. The field lines start from the same footpoints within regions with $B_z > 0$ in both panels. (Wiegmann et al. 2006).

fields themselves are not directly visible.

There are two different magnetic configurations in the Solar corona, open-field and closed-field regions. Open-field regions (white zones above the limb in Fig. 1.6), which always exist in the polar regions, and sometimes extend towards the equator, connect the solar surface with the interplanetary field and are the source of the fast solar wind. Closed-field regions (grey zones in Fig. 1.6), contain mostly closed field lines in the lower corona (less than one solar radius) and have an open configuration at higher altitudes. It is believed that are the origin of the slow solar wind component. It is noteworthy that the closed-field regions are generally bright due to the high density at lower altitudes (less than 1 solar radius), and usually they form the coronal loops which are produced by filling

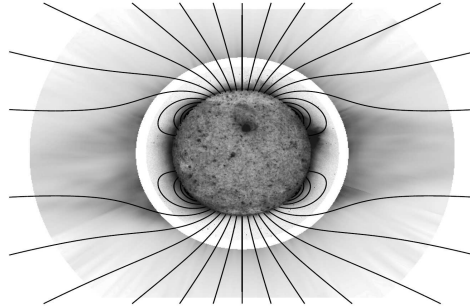


Figure 1.6: The solar corona on 17 August 1996 (near solar minimum), with bright regions plotted as dark. The inner image is the solar disk in Fe XII 195 Å emission, from the EIT instrument on SOHO. The outer image is the extended corona in O VI 1032 Å emission, from the UVCS instrument on SOHO. The axisymmetric field lines are from the model of Banaszekiewicz et al. (1998).

with chromospheric plasma that stays trapped in these closed field lines. Above roughly one solar radius, the plasma pressure may exceed the magnetic pressure, and thus plasma confinement starts to become leaky.

Density and temperature of the solar corona

Electron densities in the solar corona varies from 10^6 cm^{-3} in the upper corona (at height of one solar radius) to 10^9 cm^{-3} at the lower altitude in quiet regions. From Fig. 1.7 which displays the variation of the density and temperature as a function of height above the surface, the density increases by several orders of magnitude over coronal values, and correspondingly the temperature drops below $11 \times 10^3 \text{ K}$ (the ionization temperature of hydrogen) at the transition region. However, there are other over-dense structures with higher density than in quiet regions, and these are the topical density values n_e at the base of different regions in the sun: coronal holes, $n_e \approx (0.5 - 1.0) \times 10^8 \text{ cm}^{-3}$, in quiet sun, $n_e \approx (1 - 2) \times 10^8 \text{ cm}^{-3}$ and in active regions n_e is highest, $n_e \approx 2 \times 10^8 - 2 \times 10^9 \text{ cm}^{-3}$. From the spectral line analysis of coronal emission, it turns out that the coronal temperatures are generally above 1 MK, and still the physical understanding of this high temperature in the solar corona is unclear, and is one of the fundamental problems in astrophysics. This rapid increase in temperature from $T \approx 5800 \text{ K}$ at the photospheric boundary to about 1 MK in corona seems to violate the second thermodynamic law.

The optically thin emissions from the solar corona in soft X-ray or in EUV wavelengths shows that the temperature is completely inhomogeneous. Using the so-called "differential emission measure distribution", it is possible to measure the range of coronal temperatures at different locations on the sun (at lower altitudes) from a broad range of EUV and soft X-ray lines (see Fig. 1.8). For example, in quiet sun the temperature ranges between 1 – 2 MK, in active region is hotter, $T = 2.0 - 6.3 \text{ MK}$, and in coronal hole (open-field regions) the temperature is less than 1 MK. The temperature difference

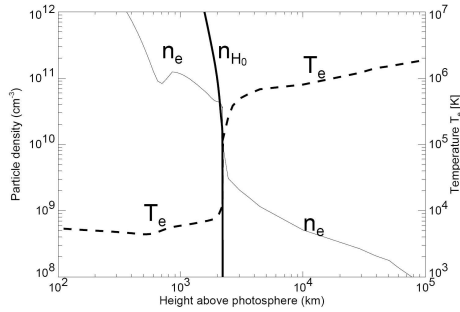


Figure 1.7: Displays of the variation of the density and temperature as a function of height above the surface. This density variation represents an averaged 1-dimensional model for a gravitationally stratified vertical fluxtube. Electron density and temperature model of the chromosphere (Fontenla et al. 1990) and lower corona (Gabriel 1976).

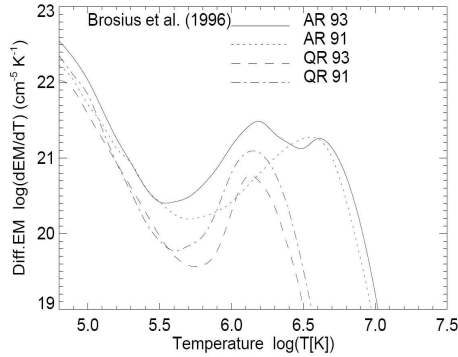


Figure 1.8: Differential emission measure distribution of two active regions (AR 93, AR 91) and two quiet Sun regions (QR 93, QR 91) measured by Brosius et al. (1996)

between Quiet-Sun and active regions gives the impression that the strong heating is most probably related to the enhanced magnetic flux emergence.

Coulomb collisions and plasma beta in the solar corona

The plasma beta, β , is an interesting parameter that indicates which pressure dominates the plasma medium, either magnetic pressure p_m or thermal pressure p_n , or both of

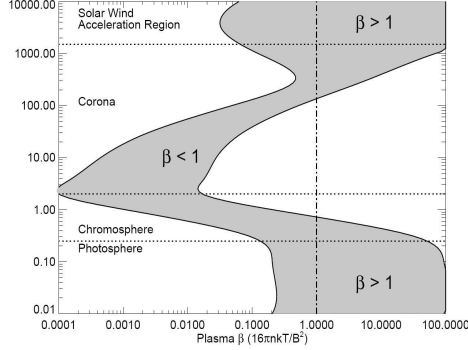


Figure 1.9: Plasma β in the solar atmosphere for two assumed field strengths, 100 G and 2500 G. (Gary 2001)

them. The plasma β is defined as follows

$$\beta = \frac{p_{th}}{p_m} = \frac{2n_e k_B T_e}{B^2/8\pi}, \quad (1.1)$$

where, $k_B = 1.38 \times 10^{-16}$ erg K^{-1} is the Boltzmann constant. B the magnetic field strength and T_e is the electron temperature.

In coronal plasma, the magnetic field B exerts a Lorentz force on the charged particles leading to a gyration motion around the field lines. Only when the kinetic energy exceeds the magnetic energy ($\beta > 1$), particles can escape from the guiding lines and diffuse across the field lines.

A comprehensive model of the plasma- β parameter has been suggested by Gary (2001) (see Fig. 1.9), in which we can see the range variation of the plasma- β (as shown in grey in the figure) for any given height above the surface of the sun. It turns out that in coronal heights $h \gtrsim 140$ Mm the plasma- β takes values above unity. While at lower coronal altitudes ($h \lesssim 30$ Mm), the plasma- β values are very small ($\beta \ll 1$) indicating a strong domination of the magnetic energy. This means that most of coronal structures that characterize the lower part of the corona like e.g. coronal loops are shaped within their magnetic field configurations.

The coronal plasma is weakly collisional but strongly magnetized, which means that the particle gyroradius is much smaller than the collisional free path, $r_{i,e} \ll \lambda_{i,e}$, and the gyrofrequency much larger than the collision frequency, $\Omega_{i,e} \gg \nu_{i,e}$. Numerical values of the Coulomb collision rate, $\nu_{i,e}$, of the electrons and protons can, for example, be found in Braginskii (1965) or Helander and Sigmar (2002):

$$\nu_{i,e} = \frac{\sqrt{2}}{12\pi^{3/2}} \frac{n_i Z_i^2 e^4 \ln \Lambda}{m_e^{1/2} T_e^{3/2} \epsilon_0^2} = (3.44 \times 10^{11})^{-1} \left(\frac{n_e}{1m^{-3}} \right) \left(\frac{1 eV}{T_e} \right)^{3/2} s^{-1}, \quad (1.2)$$

Table 1.1: Typical mean free path, λ_c , estimated for different regions; Chromosphere, corona and solar wind. (Marsch 2006)

Parameter	Chromosphere (1.01 SR)	Corona (1.3 SR)	Solar wind (1 AU)
n (cm^{-3})	10^{10}	10^7	10
T (K)	10^3	$1 - 2 \times 10^6$	10^5
λ_c (km)	1	10^3	10^7

Here the plasma is quasi-neutral, i.e., $Z_i n_i \approx n_e$. The parameters m_e , T_e , n_i , e , ϵ_0 are respectively the mass and the temperature of the electron, the density and the charge number of the ions, the electron electric charge and the electric permittivity in vacuum. The Coulomb logarithm $\ln \Lambda \approx 19$ in corona. The mean free path can easily be obtained from the thermal speed of electrons, v_{te} , and the collision frequency $\nu_{i,e}$ as $\lambda_{i,e} = v_{te} / \nu_{i,e}$.

Some typical values of different parameters in chromosphere, corona and solar wind are given in Tab. 1.1. It seems that collisions are generally rare. Therefore, electrons and ions may strongly violate the requirements of classical transport, which is to say that their collisional free paths are large against any fluid scale, especially in the outer corona and solar wind. In a simple description of collisions one may say that the fast wind from coronal holes is collisionless, and only in some dense coronal structures e.g., loops and plumes where the collisions may play a role, which is still not strong enough, as we will see in the future chapters.

1.1.1 Collisional coronal heating mechanism

Many different heating mechanisms may cause the coronal heating, but the question is which one can be the dominant for this heating. A number of plausible theories for coronal heating have been proposed based on two main mechanisms; direct current (DC), in which the heating can be caused by the collisional current dissipation, and alternating current (AC) where the heating is achieved by collisional wave dissipation. It is widely accepted that mechanical motions in and below the photosphere are the ultimate source of the energy. These motions displace the footpoints of coronal magnetic field lines and either quasi-statically stress the field and thus are generating currents or generate waves, depending on whether the timescale of the motion is long or short compared to the end-to-end Alfvén travel time. Dissipation of magnetic stresses is referred to as direct current (DC) heating, and dissipation of waves is referred to as alternating current (AC) heating.

DC heating

Footpoint motions perform work on the coronal magnetic field and increase its free energy at a rate given by the Poynting flux through the base. Magnetic flux tubes in the photosphere are displaced by turbulent convection and are observed at the surface with a characteristic horizontal velocity of order 10 km s^{-1} (Muller et al. 1994, Berger and Title 1996), and it is shown that the magnetic energy flux transported to the corona is adequate to explain the observed energy losses of both the quiet Sun and active regions. Because

classical dissipation coefficients are extremely small in the corona, significant heating generally requires the formation of very steep gradient and very small spatial scales. Magnetic gradients and their associated electrical current lead to heating by reconnection and Ohmic dissipation. Indeed, the magnetic field lines become twisted and braided as a response to the continual upward advection of magnetic flux from below the photosphere. However, the magnetic field can adapt itself to the motion and evolves between near-magnetostatic equilibrium, thus the coronal currents are almost direct ones (see book of Priest 1984). Since the collision coefficients are small, the dissipation of these current as Joule heating is very negligible. But if the magnetic field lines form localized current sheets at scales less than 100 m, then the ohmic dissipation will be efficient due to high current formation. This also leads to a rapid diffusion of field lines produces the so called magnetic field-line reconnection. This causes the phenomena called flare events with different scales, e.g., microflare, nanoflare and picoflare depending on the scale of energy released in solar corona and solar atmosphere (see e.g., Parker 1988, Berger 1991, 1993, Galsgaard and Nordlund 1996).

One has to note that the magnetic field reconnection often coincides with current sheets that mark a sudden change in the direction of the magnetic field, but a current sheet is not necessary to the formation of a separatrix, or to magnetic reconnection.

Is still not obvious that the small-scale flare events can be responsible for the base heating of solar corona since these events may occurred in an impulsive way in some local positions in corona and upper chromosphere. However, from the entangled magnetic field lines caused by the magnetic carpet (the low-lying close field) and the expanded flux tube, the reconnection may often occurs, leading to a nearly static release of energy. Therefore, this mechanism can be a good candidate to explain the coronal heating.

AC heating

When the velocity field in the photosphere changes on a shorter time scale (shorter than the Alfvén transit time in closed loop) the same turbulent convection (that quasi-statically stresses the coronal field) also generates a large flux of upwardly propagating waves. These waves can be acoustic, Alfvén, and fast and slow magnetosonic plane waves, as well as torsional, kink, and sausage magnetic flux tube waves. At different heights in the atmosphere, these waves undergo mode coupling and processes and transfer the energy between the wave types (see, e.g., Stein et al. 1991). The estimated energy flux of these waves at the top of the convection zone is roughly several times $10^7 \text{ erg cm}^{-2} \text{ s}^{-1}$ (Narain and Ulmschneider 1996). Energy fluxes of this magnitude are more than adequate to heat the corona. However, due to the very steep density and temperature gradients that exist in the chromosphere and transition region, only a small fraction of the flux is able to pass through. Acoustic and slow-mode waves form shocks and usually are strongly damped, while fast-mode waves can be refracted and reflected (Narain and Ulmschneider 1996). Mostly, transversal Alfvénic waves (Alfvén waves, Alfvén-like torsional and kink tube waves), are best able to penetrate into the corona. Because they do not form shocks and their energy is ducted along the magnetic field rather than being refracted across it. Mostly the observed energy flux estimates of such waves is about of $10^7 \text{ erg cm}^{-2} \text{ s}^{-1}$ in regions of strong magnetic field (see e.g., Ulrich 1996). Later In Sec. 3.2 we give some works about the observations of coronal Alfvén waves.

It is widely believed that the dissipation of these MHD waves at different coronal altitudes may provide enough source of energy to heat solar corona (see, e.g., Ofman 2005). However, the classical collision heating processes are only adequate when strong spatial gradients of physical variables like density, velocity, temperature, or magnetic field strength occur. Therefore, several studies have focused on the possible role of the strong cross-field gradient which results for a strongly non-uniform Alfvén speed across the magnetic field lines, thus, leading to an enhanced damping of Alfvén waves by either phase mixing (see e.g., Hood et al. 1997a,b) or absorption of surface waves along loops acting as resonant cavities (Ofman et al. 1995). The phase mixing occurs when the magnetic field is excited by Alfvén waves inducing instabilities and enhancing dramatically the viscous or Ohmic wave dissipation (Heyvaerts and Priest 1983), while resonant absorption occurs when a magnetic loop is excited with a frequency that matches the Alfvén eigenfrequency, $\omega_{res} \sim \frac{v_A}{L}$, so that standing waves are induced in the loop. If there is a wave-speed gradient across the loop, a single thin surface will resonate and the gas velocities will again have large gradients. The wave-speed gradient will also provide surfaces that resonate at different frequencies, and effectively absorb waves (by Ohmic or viscous dissipation) within a large range of frequencies (Ofman et al. 1994).

Problematics in collisional dissipation mechanism

Most of coronal heating models are mainly based on ohmic, conductive, and viscous dissipation of the magnetic energy originated from the random photospheric motion. However, according to the corona and chromosphere plasma collisions shown in Tab. 1.1, the collisional heating rates are too small. Therefore, shock heating is presently favoured there (see e.g., Ulmschneider and Kalkofen 2003).

Here we present the estimation of the different collisional heating rates that characterize the upper chromosphere where the problem starts to arise (see review by Marsch 2006). We consider the typical plasma parameters of density, $n = 10^{10} \text{ cm}^{-3}$, and pressure scale height, $h = 400 \text{ km}$, and assume the perturbation values are: $L = 200 \text{ km}$ (scale length), $\Delta B = 1 \text{ G}$, $\Delta V = 1 \text{ km s}^{-1}$, $\Delta T = 1000 \text{ K}$. With these reasonable parameters the dissipation rates are (in cgs units) as follows: Through viscous shear, $Q_V = \eta(\Delta V/L)^2 = 2 \times 10^{-8}$, through thermal conduction, $Q_c = \kappa(\Delta T/L)^2 = 3 \times 10^{-7}$, and through Ohmic resistance, $Q_J = j^2/\sigma = (c/4\pi)^2(\Delta B/L)^2/\sigma = 7 \times 10^{-7}$. Here j is the plasma current density, and the transport coefficients are viscosity, η , heat conductivity, κ , and electrical conductivity, σ , for which values can be found in Braginskii (1965). When we compare these obtained values with the estimated radiative loss rate $Q_R = n^2\Lambda(T) = 10^{-1} \text{ erg cm}^{-3} \text{ s}^{-1}$, (with the radiative loss functions Λ) (see book of Priest 1984), the radiative loss rate Q_R is a factor of 10^6 or more larger than $Q_{V,c,j}$. Therefore, a much smaller than the assumed scale, (e.g., $L = 200 \text{ m}$), is required to match heating to cooling. Moreover, the gradient scales L assumed for this approach is much larger than the estimated collision mean free path $\lambda_c = 110 \text{ km}$ (within the chromosphere plasma condition), thus the classical Braginskii formulas for obtaining η and σ seriously break down. Much less collisional heating rates are expected when considering coronal conditions where these classical rates have to be enhanced by more than six orders of magnitude, to match the empirical damping of loop oscillations (Nakariakov et al. 1999), or dissipation of propagating waves (Ofman et al. 1999).

Moreover, in coronal regions, most of the arguments given for the conversion mechanism of the magnetic energy in the diffusion area (where the current sheet is formed) are based on the classical ohmic dissipation. This can be misleading, because at this area the electric resistivity is small and the chapmann-Enskog regime can be completely violated, since the magnetic field gradient is smaller than the mean free path. Therefore, the conversion of the magnetic energy in this area has nothing to do with the classical collisional MHD description, and rather the kinetic or multi-fluid approaches have to be involved to describe the conversion mechanism (see e.g., work on the heating via reconnection in weakly collisional plasma Ji et al. 2001).

1.1.2 Collisionless heating mechanism

Coronal heating by collisionless dissipation

Now, it seems that the coronal heating process has to be rather explained by collisionless dissipation mechanism that may convert the magnetic energy density to heating in solar corona and upper chromosphere. In other words, one has to deal with kinetic descriptions of the coronal heating instead of the classical resistive MHD theories.

In collisionless dissipation mechanism, the so-called "ion-cyclotron waves" (small scale fluctuations close to the ion inertial length $1/k_d$) play the major role in the heating of the solar corona and even on the acceleration of ions in solar wind (see, e.g., Cranmer 2001). It is found that, for any plasma beta values β , the ion-cyclotron damping is the dominant dissipation mechanism for parallel propagating waves, however, in low plasma beta, also the damping at the electron Landau resonance can be relevant for oblique propagating waves with $k < k_d$ (see e.g., Gary and Borovsky 2004).

However, there are no direct measurements of ion-cyclotron waves in the solar coronal medium, and it is supposed that these waves get absorbed at distances close to the Sun before they reach the heliosphere. However, the main signatures of the dissipation of these waves were observed in solar wind as well as in solar corona. Indeed, recent observations using Helios data (see e.g., Heuer and Marsch 2007) have confirmed the plateau formation in the velocity distribution functions (VDfs) of proton species, which is interpreted as a consequence of resonant wave-particle interaction caused by the ion-cyclotron waves (see Fig. 1.10). Furthermore, in the corona, the spectroscopic determination of the widths of extreme ultraviolet emission lines, as obtained from measurements made by SUMER and UVCS onboard of SOHO indicate that heavy ions in various ionization stages in the corona are very hot (see, e.g., Kohl et al. 1998, Tu 1988, Wilhelm et al. 1998, Cranmer et al. 1999a, Grall et al. 1996) particularly in the polar coronal holes where electrons are relatively cold (Fig. 1.11).

It is believed that these ion-cyclotron waves are generated at the coronal base when the small-scale reconnection may continuously occurs in the chromospheric network (see, e.g., Axford and McKenzie 1995, Axford et al. 1999). This microflare like-event is produced when the cooled small-scale loops (~ 1 Mm), that arise from the convection motion, reconnect with the expanding flux tube then cause a small-scale reconnection at the chromosphere network, thus can generate high-frequency waves via current-driven microinstability in the diffusion areas when the current sheets are formed. The dissipation of these high-frequency waves occurs close to the Sun within a fraction of solar radius and

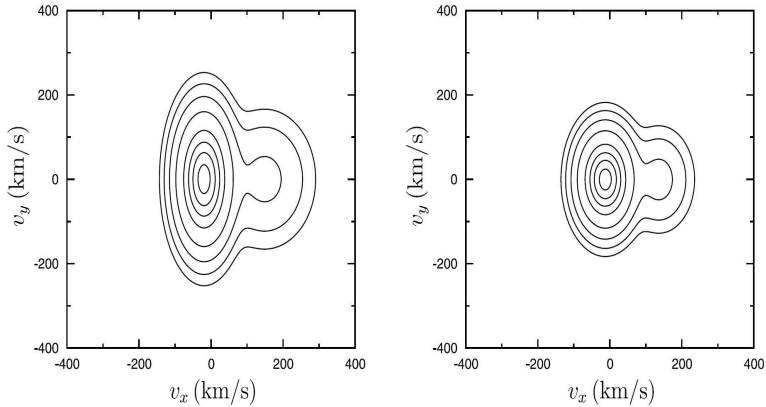


Figure 1.10: Contours of core/beam decompositions of two exemplary proton VDFs. They were obtained by Helios 2 at (left) 10/46/08 on 14 April 1976 and (right) 04/24/52 on 16 March 1976. Both proton core and beam are here represented by drifting bi-Maxwellians. The contours are plotted in the plane spanned by the mean magnetic field (x axis) and the mean proton velocity, which coincides with the origin. The contours correspond to fractions 0.9, 0.7, 0.5, 0.3, 0.1, 0.03, 0.01, and 0.003 of the maximum of each distribution function. (Heuer and Marsch 2007).

involves a linear kinetic mechanism such as Landau damping and ion-cyclotron resonance absorption through the frequency-sweeping mechanism in a rapidly declining magnetic field (Tu and Marsch 1997, Vocks 2002).

Other possible scenario as "MHD cascade mechanism" can be responsible the the generation of ion-cyclotron waves. The high-frequency ion-cyclotron waves may be generated locally through turbulent cascade of low-frequency MHD-type waves towards high frequency ion-cyclotron waves (Hollweg 1986, Tu 1987, 1988, Marsch and Tu 1990, Hu et al. 1999, Hollweg 2000, Ofman et al. 2002). In the turbulence scenario, the large-amplitude, long-wavelength magnetic fluctuations, undergo nonlinear processes that cascade their energy to successively shorter wavelengths. This leads to an ensemble of fluctuations with a random phases and a broad range of wave vectors propagating in the plasma. This picture is well explained by MHD simulations in homogeneous, collisionless, magnetized plasmas (Biskamp and Müller 2000) which satisfy the classical Kolmogorov picture of fluid turbulence so that the magnetic power spectrum is approximately proportional to $k^{-5/3}$, this wave number regime is usually termed the "inertial range".

Turbulence magnetic fluctuations are subject not only to the cascade process but also to collisionless damping in which some of the wave energy is transferred to particles. This collisionless damping can be higher when the wavenumber k is larger so that the wavelength is comparable to the ion or electron inertial range or called "dissipation range". Although magnetic power spectral properties in the inertial range are independent of the

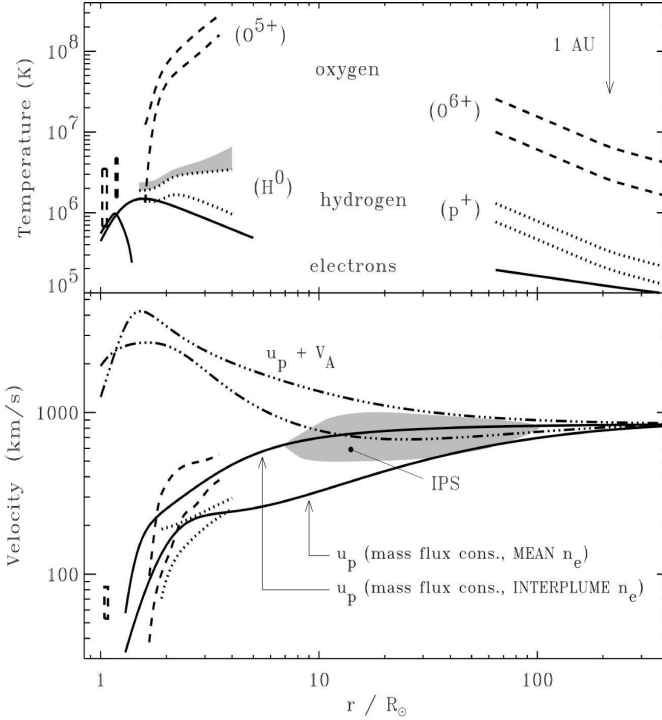


Figure 1.11: Plot of empirically derived temperatures and wind velocities. Upper panel: electron (solid), hydrogen (dotted), and oxygen (dashed) temperatures, with neutral hydrogen and O^{5+} in the corona, and protons and O^{6+} in the far solar wind. Lower panel: proton velocities derived from mass flux conservation (solid lines), Doppler dimming velocities for hydrogen (dotted) and oxygen (dashed), and the summed ($u_p + V_A$) "surfing" speeds (dash-triple-dot). The gray region denotes the range of polar IPS speeds reported by Grall et al. (1996).

cascade processes, the properties of the dissipation range spectra depend upon the damping rate. Also, the turbulence cascade usually leads to $|\delta B|/B_0 \ll 1$ in the dissipation regime which allows to use the linear theory for describing the dispersion properties.

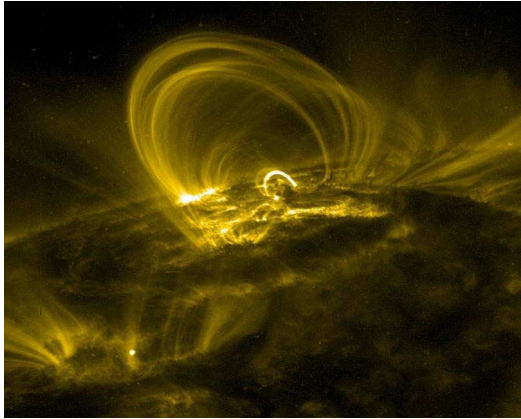


Figure 1.12: Example of solar coronal loops observed by the Transition Region And Coronal Explorer (TRACE), in the 171Å filter. These loops have a temperature of approximately 10^6K .

1.2 Coronal loops

1.2.1 Coronal loop observations

Coronal loops are often observed as isolated bright flux tubes that can extend to altitudes lower than one solar radius (see Fig. 1.12). Therefore coronal loops form the basic structure of the lower corona and transition region of the Sun. These highly structured and elegant loops are a direct consequence of the twisted solar magnetic flux within the solar body. The population of coronal loops can be directly linked with the solar cycle, it is for this reason the coronal loops are often found with sunspots at their footpoints.

The temperatures and densities of loops are found to vary transversely on small scales between adjacent loops (Aschwanden et al. 1999, 2000b, Lenz et al. 1999, Brković et al. 2002). Serio et al. 1981 proposed a hydrostatic loop model including gravity, in which they considered a semi-circle loop with a constant cross section and assumed a constant pressure along the loop with uniform heating. Their model predicts a steep temperature profile that rises from the loop footpoints and increases above the transition to the loop apex. The model was found to be consistent with the high-temperature loops observed with X-ray instruments (e.g., Kano and Tsuneta 1996).

Most of the warm coronal loops ($T \approx 1\text{ MK}$) observed in EUV emission by TRACE and EIT imagers, are over dense compared to what is expected for static equilibrium (Aschwanden et al. 1999, 2001, Winebarger et al. 2003a) or for steady flow equilibrium (Patsourakos et al. 2004). The discrepancy is reduced, but not eliminated, if the heating is assumed to be concentrated near the loop footpoints. Furthermore, under the assumption that the plasma is isothermal across its field lines, several authors (e.g., Lenz et al. 1999, Aschwanden et al. 2000b, Testa et al. 2002, Winebarger et al. 2003a) measured the density

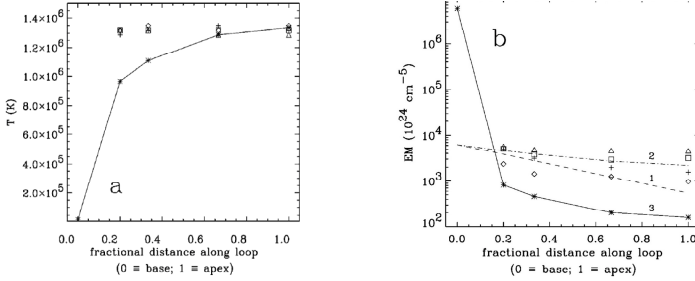


Figure 1.13: (a) Temperature and (b) emission measure as functions of fractional distance along four loops: for loop (1) (plus signs), loop (2) (diamonds), loop (3) (triangles), loop (4) (squares). They are compared with the hydrostatic loop model with $T_{apex} = 1.34 \times 10^6$ K and uniform line-of-sight depth $D = 10^{10}$ cm (connected asterisks). (Lenz et al. 1999).

and temperature profiles along coronal loops using data from TRACE and EIT on board SOHO. Their results show that the warm coronal loops visible in the extreme ultraviolet (EUV) light are dense and have a roughly constant temperature along their segments (see Fig. 1.13-1.14).

In contrast, from Fig. 1.15, hot loops, $T > 2$ MK (or often called SXR loops) observed by Yohkoh are under dense compared to static equilibrium (Kano and Tsuneta 1996, Winebarger et al. 2003a). Loops of intermediate temperature observed by the SXI instrument on GOES-12 have about the right density (Lopez Fuentes et al. 2004, Klimchuk 2006). This may indicate three physically distinct classes of loops, perhaps heated in completely different ways, but there is another possibility that unifies the results into a single picture. The over and under densities are related to the ratio of the radiative to conductive cooling times (τ_r/τ_c). Radiation and thermal conduction losses are comparable in equilibrium loops (Vesecy et al. 1979), and therefore the cooling time ratio should be close to unity for loops that are near equilibrium.

The isothermality assumption across the field has recently been debated. Some works had the conclusion that the cross-field temperature is roughly constant. Using TRACE images and coalignment data from the Coronal Diagnostic Spectrometer (CDS) on SOHO, they found the similar features of warm EUV loops given above (see e.g., Cirtain et al. 2007, Landi and Landini 2004, Warren et al. 2008). However, some other observations (see e.g., Schmelz et al. 2001, Martens et al. 2002) indicate that a loop can have varying cross-field temperature, which means that loops are composed of many strands that are heated differently (i.e., different heating scales and heated at different times).

1.2.2 Expansion of coronal loops

According the force-free models, the flux tubes of coronal loops expand with height leading to thicker widths at the loop top than at the footpoints (or the end-points of the coronal loop which are situated near the transition region) (see e.g., Klimchuk 2000, Watko and Klimchuk 2000). However, from the observations, it is shown that loop widths of most of

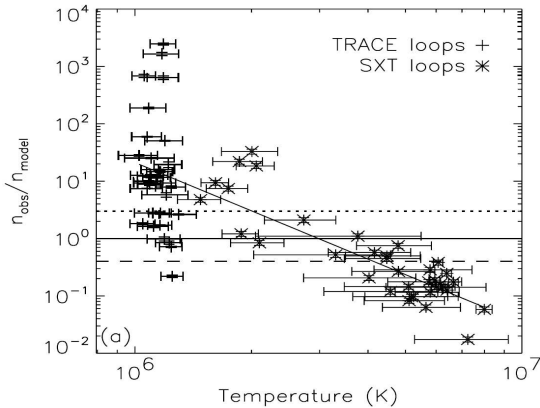


Figure 1.14: Ratio of observed densities to predicted densities as a function of temperature. If the observations agreed with static solutions of hydrodynamic equations with uniform heating, the points would lie on the solid line. Footpoint heating has the potential to increase the density in a loop by a factor of 3 over uniform heating; this is shown in the figure panels as a dotted line. Apex heating has the potential to decrease the density in a loop by a factor of 2.5; this is shown in the figure panels as a dashed line, ((Winebarger et al. 2003a).

EUV and SXR loops does not vary too much, and the flux tubes have a small expansion with height.

Klimchuk (2000) has examined the widths (radius of cross section) of 43 soft X-ray loops observed by Yohkoh (hot loops having temperature more than 2 MK). He deduced that the loop tends to be slightly (≈ 30 per cent) wider at their midpoints than at their footpoints (see Fig. 1.15), implying less-than expected expansion factor $\Gamma = w_{top}/w_f \approx 1.3$ (where w_{top} and w_f are the width at the loop top and at footpoints, respectively). While it is found that warm loops observed by TRACE/EUV emission (in 171 Å passbands) have roughly constant widths, $\Gamma \approx 1$, (see Fig. 1.15-1.16).

The loop widths are determined from the straightened (symmetric axis of the loop), background-subtracted images and the cross variation intensity at each segment. The loop width is defined as the second moment of the intensity profile i.e.,

$$\sigma = \left[\frac{\sum (x_i - \mu)^2 I_i}{\sum I_i} \right]^{1/2}, \quad (1.3)$$

where μ is the mean position, $\mu = \sum x_i I_i / \sum I_i$. Because the three-dimensional geometry of the loops is not known, it was attempted to eliminate possible projection effects by selecting loops from a variety of different positions on the disk and at the limb. The hope is that any such effects would then average out statistically and not influence the results. The obtained results of small-varying loop cross sections have recently been confirmed

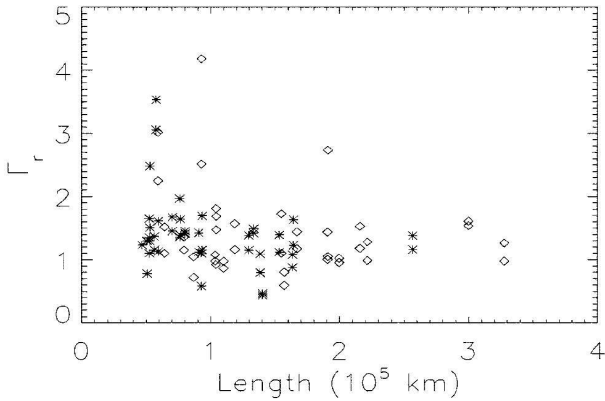


Figure 1.15: Expansion factor (ratio of midpoint radius to footpoint radius) as a function of loop length. Stars and diamonds are for full- and half- resolution observations, respectively. (Klimchuk 2000).

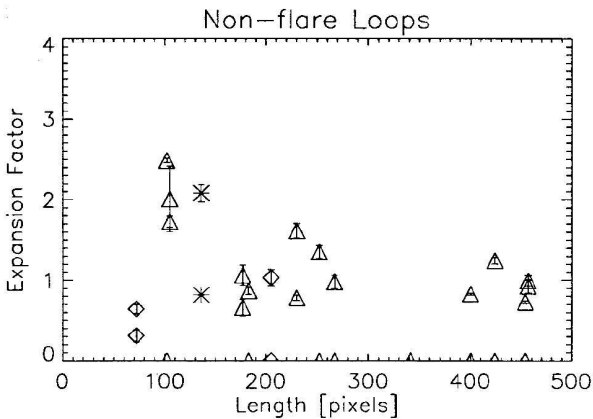


Figure 1.16: Loop radius expansion factors are plotted versus loop length for all 15 non-flare loops. Triangles, diamonds, and asterisks indicate 171, 195, and 284 Å measurements, respectively. (Watko and Klimchuk 2000).

by López Fuentes et al. (2008) where they have shown that a constant loop widths is not an artifact of the background and the spatial resolution.

1.2.3 Nanoflare model for coronal loop

In the most of the coronal loop models, a semi-circle geometry with varying or constant cross section is assumed for the bundles of the coronal magnetic field lines. Also, because the plasma and magnetic field are frozen together (low-beta condition is valid) and the cross-field thermal conduction is weak relatively to the thermal conduction driven by electrons along the fields, it is possible to treat the strand loop with 1D hydrodynamics (HD) or magnetohydrodynamics (MHD) models to describe the plasma response to the energy dissipated in the loop. Furthermore, often the magnetic field is assumed to be rigid and plays only a passive role by channelling the plasma and thermal energy along the field lines. Therefore, the loop can be treated as individual magnetic flux strands being mini-loops for which the heating and plasma properties are approximately uniform on a cross section.

As we already mentioned, the coronal loops may have broad differential emission measure distributions within their cross sections; i.e., they are multithermal. Given that heat transport is inefficient across magnetic field lines in the solar corona, this indicates that loops are composed of multi-subresolution magnetic strands. In most of the impulsive coronal loop heating models, they suggest that each of the strands is heated impulsively and at different times from its neighbours. Although each strand evolves rapidly, the unresolved bundle that is the loop appears to change slowly compared to a cooling time (Winebarger et al. 2003b).

The nanoflare heating is dating back to Parker's idea (1988) who introduced the idea of the impulsive releases of roughly 10^{24} ergs of energy (some 9 orders of magnitude smaller than large scaleflares). Parker's mechanism is a part of the DC heating mechanism. He suggested that the random, slow motions of the footpoints of field lines in the photosphere make the magnetic field in the corona entangled and braided and increase its free energy. When the angle between adjacent misaligned flux strands reaches a threshold, usually related to the secondary instability (Dahlburg et al. 2003, 2005), current sheets will form and via the reconnection, a thermal energy can be released via ohmic dissipation. If nanoflares now indeed energies of 10^{24} erg, and if coronal loops contain a large number of strands then the observed heating requirements of loops implies that the repeat time for successive nanoflares in a given strand must be longer than a cooling time. Cargill (1994), and later Klimchuk and Cargill (2001) and Cargill and Klimchuk (2004) modeled the properties of loops in the context of this basic framework. They found that nanoflare-heated strands initially cool by thermal conduction and later cool by radiation. The first phase of cooling is characterized by underdensities relative to static equilibrium, and the second phase is characterized by overdensities (Warren et al. 2002, Klimchuk et al. 2004, Spadaro et al. 2003, Cargill and Klimchuk 2004).

This impulsive multistrands heating may explain the multithermality across the field found by Schmelz et al. (2001). A critical aspect of this picture is that the nanoflare repetition time is long compared to a cooling time. If it were significantly shorter than a cooling time, each strand would be in a state of quasi-static equilibrium (e.g. Walsh et al. 1997, Mendoza-Briceño et al. 2002, Testa et al. 2005). This would be the case if the loop contained only a few strands, since the observed heating requirements imply a certain rate of 10^{24} erg nanoflares across the whole loop. The nanoflare model thus implies roughly constant cross-field temperature.

1.3 Motivations and outlines of the present thesis work

For the reasons we mentioned in subsection 1.1.1, the heating of solar corona seems difficult to be achieved via the classical collisional transport theory. Indeed, the gradient scales in the plasma parameters need to be much smaller than the mean free path that characterizes the collisions in corona. This condition is certainly far from the validity regime of the magnetohydrodynamics (MHD) or hydrodynamics (HD). This conclusion is further confirmed given the temperature anisotropy and the preferential heating of heavy ions observed in corona. These observations provide a good indication that the plasma of the corona is far from the local thermal equilibrium (LTE), thus its heating cannot be described by the collisional MHD or HD. Therefore, a kinetic approach involving collisionless heating mechanism is inevitably needed to describe the heating of solar corona. In such description the heating via ion-cyclotron resonance could be relevant for the solar corona. As we mentioned in subsection 1.1.2, the heating via ion-cyclotron resonance may explain the observed temperature anisotropy and preferential heating at higher coronal altitudes, and the plateau formation found in the proton velocity distribution function (VDFs) measured in heliosphere regions.

In our present work, we focus on the collisionless heating of solar corona based on the resonant and nonresonant wave-particle interactions described within the quasi-linear theory of the Vlasov equation. Here, the collisions are included especially when we deal with the lower corona, and they are evaluated kinetically using the Fokker-Planck equation (Rosenbluth et al. 1957).

The thesis is organized as follows; In Chap. 2, we study the heating of a collisionless plasma through the dissipation of oblique propagating fast ion-cyclotron waves. The damping is achieved via resonant wave-particle interactions. In Chap. 3, we study the heating of the corona by the collisionless dissipation of low-frequency Alfvén waves (having frequencies much smaller than the ion gyrofrequency, $\omega \ll \Omega_i$). Then, Chaps. 4-6 are devoted to the coronal loop modeling, where a semi-kinetic model (time-dependent model) is adopted to describe the heating along the loop length. In these last Chapters, we aim to produce the observed features of warm EUV and SXR coronal loops given in Sec. 1.2.

2 Proton heating by oblique fast waves

2.1 Introduction

Recent observations from the Ultraviolet Coronagraph Spectrometer (UVCS) and Solar Ultraviolet Measurements of Emitted Radiation (SUMER) on board SOHO have shown that the preferential heating and acceleration of ions (e.g., oxygen ions) occurs in the first few solar radii of the high-speed solar wind (Kohl et al. 1998, Li et al. 1998, Wilhelm et al. 1998, Cranmer et al. 1999c, Frazin et al. 2003, Telloni et al. 2007). Also, it is concluded that not only do the oxygen ions flow faster than protons at a speed of 400 km s^{-1} at roughly $3 R_S$, but also have a large temperature anisotropy at the same distance (see e.g., Li et al. 1998). These observed phenomena have revived the interest in the energizing of ions by the fast kinetic dissipation of the small-scale wave-field fluctuations (in the range of ion inertial length). It is believed that the dissipation of these waves, in the solar wind, via the ion-cyclotron resonance mechanism may cause such phenomena. The acceleration and heating of minor ions by ion-cyclotron wave absorption has been studied in several theoretical works (e.g., Cranmer et al. 1999b, Cranmer 2000, Hollweg 1999a,b, Li et al. 1999, Vocks and Marsch 2002, Bourouaine et al. 2008a). However, in situ measurements have not indicated strong enough ion-cyclotron waves, hence, it has been assumed that these waves are probably launched from the Sun and already damped in interplanetary space (see e.g., Tu and Marsch 1997, Marsch and Tu 1997, Li et al. 1999, Heuer and Marsch 2007).

Most studies of resonant heating of the corona and acceleration of the fast solar wind have considered parallel-propagating waves. This limited consideration is for the reason of simplicities. However, it is intuitively reasonable to expect that high-frequency waves can obliquely propagate due to several sources or processes that can generate oblique propagating waves. For example, the phase-mixing mechanism that could result from the inhomogeneity across the magnetic field lines (e.g., Voitenko and Goossens 2000a,b), forces the parallelly launched waves into oblique propagation. Also, magnetohydrodynamics (MHD) turbulence in the Kolmogorov picture favours a cascade to high transverse wave number (Cranmer and van Ballegoijen 2003).

The dissipation of the high obliquely propagating waves (e.g., Kinetic Alfvén waves) can strongly suffer from Landau damping at lower-frequencies (frequencies much less than ion-cyclotron frequency) when the perpendicular wavenumber is approaching the inverse of the proton gyroradius (see e.g., Hollweg 1999c).

In this chapter, we study the heating of the protons by the obliquely propagating fast waves. In Sec. 2.2 we establish the the linear dispersion relation for a magnetized and homogeneous plasma. In Sec. 2.3 we study the properties of the of the oblique fast waves

propagating in homogeneous electron/proton plasma. Finally, based on the quasi-linear theory (QLT) for reduced velocity distribution function, we study the energization of the protons by oblique propagation fast waves via resonant wave-particle interaction.

2.2 Magnetized dispersion relation

2.2.1 General dispersion function

In the following section, we remind of the general wave kinetic dispersion relation of linear waves that can propagate in a homogeneous and collisionless plasma in the presence of a constant magnetic field \mathbf{B}_0 . In this study, we consider a vanishing external electric field, \mathbf{E}_0 . The presence of the magnetic field produces an anisotropy in the plasma by affecting the perpendicular particle motions through the Lorentz force.

First we recall the famous Vlasov equation that describes the evolution of the velocity distribution function (VDF) f of non-relativistic moving particles in collisionless plasma

$$\left(\frac{\partial}{\partial t} + \mathbf{v} \cdot \nabla + \frac{q}{m} (\mathbf{E} + \mathbf{v} \times \mathbf{B}) \cdot \frac{\partial}{\partial \mathbf{v}} \right) f(\mathbf{v}, \mathbf{x}, t) = 0, \quad (2.1)$$

where \mathbf{v} and \mathbf{x} are the velocity and the position vectors, q and m are the charge and the mass of the species, s . \mathbf{E} and \mathbf{B} , respectively, are the electric and magnetic field acting on the plasma species.

After considering a linear perturbation for the different quantities in the Vlasov equation (2.1), we get the following linear form of the Vlasov equation

$$\left(\frac{\partial}{\partial t} + \mathbf{v} \cdot \nabla + \frac{q}{m} \mathbf{v} \times \mathbf{B}_0 \cdot \frac{\partial}{\partial \mathbf{v}} \right) \delta f(\mathbf{v}, \mathbf{x}, t) = -\frac{q}{m} (\delta \mathbf{E} + \mathbf{v} \times \delta \mathbf{B}) \cdot \frac{\partial f_0(\mathbf{v}, \mathbf{x}, t)}{\partial \mathbf{v}}, \quad (2.2)$$

where δf , $\delta \mathbf{B}$ and $\delta \mathbf{E}$, respectively are the perturbed quantities of respectively the velocity distribution function (VDF), the magnetic field \mathbf{B} and the electric field \mathbf{E} (with $\mathbf{E}_0 = 0$), i.e.,

$$\begin{aligned} f &\approx f_0 + \delta f, \\ \mathbf{B} &\approx \mathbf{B}_0 + \delta \mathbf{B}, \\ \mathbf{E} &\approx \mathbf{E}_0 + \delta \mathbf{E}. \end{aligned} \quad (2.3)$$

The response of the plasma due to these perturbations is represented by the perturbations occurred in the electric current $\delta \rho_e$ and charge density $\delta \mathbf{j}$ such that

$$\begin{aligned} \delta \rho_e &= \sum_s q_s \int d^3 v \delta f_s, \\ \delta \mathbf{j} &= \sum_s q_s \int d^3 v \mathbf{v} \delta f_s. \end{aligned} \quad (2.4)$$

Since δf depends on the time, t and the six phase-space coordinates of the vectors \mathbf{v} and \mathbf{x} , the left-hand side of (2.2) is the total time derivative of δf along a particle phase space orbit, and the right-hand side describes the change of the distribution function along

this orbit under the effect of the wave field. Thus this equation can be written as

$$\frac{d}{dt}\delta f(\mathbf{v}(t), \mathbf{x}(t), t) = -\frac{q}{m}[\delta \mathbf{E}(\mathbf{x}(t), t) + \mathbf{v}(t) \times \delta \mathbf{B}(\mathbf{x}(t), t)] \times \frac{\partial f_0(\mathbf{v}(t), \mathbf{x}(t), t)}{\partial \mathbf{v}}, \quad (2.5)$$

and then the calculation of δf needs an integration of the above equation over the time

$$\delta f(\mathbf{v}(t), \mathbf{x}(t), t) = -\frac{q}{m} \int_{-\infty}^t dt' [\delta \mathbf{E}(\mathbf{x}(t'), t') + \mathbf{v}(t') \times \delta \mathbf{B}(\mathbf{x}(t'), t')] \times \frac{\partial f_0(\mathbf{v}(t'), \mathbf{x}(t'), t')}{\partial \mathbf{v}}. \quad (2.6)$$

At this stage, the knowledge of the phase-space orbit of all particles for all times $t' < t$ is required to evaluate this integral. This is not possible, but within this linear approach where the nonlinear terms are completely neglected, it is possible to consider approximately the particle orbit when the plasma is in its unperturbed state and only under the effect of the background magnetic field \mathbf{B}_0 . Then, the equations of motion of particles that move under the effect of an external constant magnetic field can be expressed in terms of the gyrofrequency Ω ,

$$\mathbf{v}(\tau) = \{v_{\perp} \cos[\Omega(\tau) + \psi], v_{\perp} \sin[\Omega(\tau) + \psi], v_{\parallel}\}, \quad (2.7)$$

where ψ is the initial phase angle, $\tau = t' - t$ and v_{\parallel} (v_{\perp}) is the parallel (perpendicular) component of the velocity vector \mathbf{v} with respect to \mathbf{B}_0 . The time integral of the velocity equation (2.7) gives the position of the particle,

$$\mathbf{x}(\tau) - \mathbf{x} = \Omega^{-1} \{v_{\perp} \sin[\Omega(\tau) + \psi], -v_{\perp} \cos[\Omega(\tau) + \psi], v_{\parallel}(\tau)\}. \quad (2.8)$$

Now assuming the plane wave form for the small perturbed wave field and considering the Faraday's law, yielding $\mathbf{k} \times \delta \mathbf{E} = \omega \delta \mathbf{B}$ (where \mathbf{k} is the wavenumber vector and ω is the frequency), then eq. (2.6) becomes

$$\delta f = -\frac{q\delta \mathbf{E}(\mathbf{k}, \omega)}{m\omega} \cdot \int_0^{\infty} d\tau e^{i(\omega\tau + \mathbf{k}(\mathbf{x}(\tau) - \mathbf{x}))} [\mathbf{I}(\omega - \mathbf{k} \cdot \mathbf{v}(\tau)) + \mathbf{k}\mathbf{v}] \cdot \frac{\partial f_0(\tau)}{\partial \mathbf{v}(\tau)}. \quad (2.9)$$

By using the expressions (2.4) and (2.9) which connect between the linear current and the perturbed VDF, it is possible to extract the linear conductivity σ of the magnetized plasma from Ohm's law ($\delta \mathbf{j} = \sigma \delta \mathbf{E}$).

On the other hand, the general linear wave equation of the fluctuating electric field $\delta \mathbf{E}$ (with $\mathbf{E}_0 = 0$) can easily be obtained from the known Maxwell equations and is given by

$$\nabla^2 \delta \mathbf{E} - \nabla(\nabla \cdot \delta \mathbf{E}) - \epsilon_0 \mu_0 \frac{\partial^2 \delta \mathbf{E}}{\partial t^2} = \mu_0 \frac{\partial \delta \mathbf{j}}{\partial t}. \quad (2.10)$$

This equation is applicable to any medium with a linear response to an applied field fluctuation. Its left-hand side is independent of the presence of any medium and represents the electromagnetic part. The response of the medium is included on the right side via the

conductivity tensor that connects the current with the fluctuation electric field.

The wave equation (2.10) can be then written in its Fourier transform as follows:

$$\left[\left(k^2 - \frac{\omega^2}{c^2} \right) \mathbf{I} - \mathbf{kk} - i\omega\mu_0\sigma(\omega, \mathbf{k}) \right] \cdot \delta\mathbf{E} = 0. \quad (2.11)$$

The nontrivial solution of this equation requires that the determinant of the tensor in brackets vanishes, thus yielding the general dispersion relation

$$\begin{aligned} & \det \left[\left(k^2 - \frac{\omega^2}{c^2} \right) \mathbf{I} - \mathbf{kk} - i\omega\mu_0\sigma(\omega, \mathbf{k}) \right] \\ &= \det \left[\frac{k^2 c^2}{\omega^2} \left(\frac{\mathbf{kk}}{k^2} - \mathbf{I} \right) + \epsilon(\omega, \mathbf{k}) \right] \\ &= \det \mathbf{D} = 0, \end{aligned} \quad (2.12)$$

where \mathbf{D} is the dispersion tensor, and $\epsilon(\omega, \mathbf{k})$ is the dielectric tensor

$$\epsilon(\omega, \mathbf{k}) = \mathbf{I} + \frac{i}{\omega\epsilon_0} \sigma(\omega, \mathbf{k}). \quad (2.13)$$

From the Ohm's law and the equations (2.9) and (2.13) we extract the expression of the kinetic dielectric tensor in homogenous magnetized plasmas:

$$\begin{aligned} \epsilon(\omega, \mathbf{k}) &= \left(1 - \sum_s \frac{\omega_{ps}^2}{\omega^2} \right) \mathbf{I} - \sum_s \sum_{l=-\infty}^{l=\infty} \frac{2\pi\omega_{ps}^2}{n_{0s}\omega^2} \\ &\int_0^\infty \int_{-\infty}^\infty v_\perp dv_\perp dv_\parallel \left(k_\parallel \frac{\partial f_{0s}}{\partial v_\parallel} + \frac{l\Omega_s}{v_\perp} \frac{\partial f_{0s}}{\partial v_\perp} \right) \frac{\mathbf{S}_{ls}(v_\perp, v_\parallel)}{k_\parallel v_\parallel + l\Omega_s - \omega} \end{aligned} \quad (2.14)$$

where the tensor \mathbf{S}_{ls} has the form

$$\mathbf{S}_{ls}(v_\perp, v_\parallel) = \begin{bmatrix} \frac{l^2 \Omega_s^2}{k_\perp^2} J_l^2 & \frac{iv_\perp \Omega_s}{k_\perp} J_l J_l' & \frac{l v_\parallel \Omega_s}{k_\perp} J_l^2 \\ -\frac{iv_\perp \Omega_s}{k_\perp} J_l J_l' & v_\perp^2 J_l^2 & -iv_\parallel v_\perp J_l J_l' \\ \frac{l v_\parallel \Omega_s}{k_\perp} J_l^2 & iv_\parallel v_\perp J_l J_l' & v_\parallel^2 J_l^2 \end{bmatrix} \quad (2.15)$$

and the Bessel function and its derivative, $J_l, J_l' = dJ_l/d\eta_s$, depend on the argument $\eta_s = k_\perp v_\perp / \Omega_s$. Here ω_p is the plasma frequency, and k_\parallel (k_\perp) is the parallel (perpendicular) component of the wave vector \mathbf{k} with respect to \mathbf{B}_0 .

Notice that, when considering $\delta\mathbf{B} = 0$, only the dispersion of the electrostatic (or longitudinal $\delta\mathbf{E} \times \mathbf{k} = 0$) modes can be obtained, and the dispersion function simplifies considerably.

2.2.2 Dispersion relation for a bi-Maxwellian VDFs

Now, assume that each species in the plasma is described by a background bi-Maxwellian:

$$f_{0,s}(v_{\parallel}, v_{\perp}) = \frac{n_{0s}}{\pi^{3/2} v_{th\parallel,s} v_{th\perp,s}^2} \exp\left(-\frac{(v_{\parallel} - U_s)^2}{v_{th\parallel,s}^2} - \frac{v_{\perp}^2}{v_{th\perp,s}^2}\right), \quad (2.16)$$

where $v_{th\parallel,s}$, $v_{th\perp,s}$ respectively are the parallel and the perpendicular thermal speed defined in terms of parallel and perpendicular temperature $T_{\parallel,s}$, $T_{\perp,s}$ as: $v_{th\parallel,s} = (2k_B T_{\parallel,s}/m)^{1/2}$, $v_{th\perp,s} = (2k_B T_{\perp,s}/m)^{1/2}$, and U_s is the bulk speed, n_{0s} is the density of the species s .

The dielectric tensor given in (2.14) would take the following expression when considering a bi-Maxwellian unperturbed f_0 (see Baumjohann and Treuman 1996):

$$\epsilon(\omega, \mathbf{k}) = \mathbf{I} + \sum_s \begin{pmatrix} \epsilon_{s1} & \epsilon_{s2} & \epsilon_{s4} \\ -\epsilon_{s2} & \epsilon_{s1} - \epsilon_{s0} & -\epsilon_{s5} \\ \epsilon_{s4} & \epsilon_{s5} & \epsilon_{s3} \end{pmatrix} \quad (2.17)$$

where the components of the tensor inside the sum are given by

$$\epsilon(\omega, \mathbf{k}) = \mathbf{I} + \sum_s \left(\mathbf{e}_s \mathbf{e}_z \frac{2\omega_p^2}{\omega k_{\parallel} v_{th\perp}^2} v_d + \frac{\omega_p^2}{\omega} \sum_{l=-\infty}^{\infty} e^{-l} L_l(\eta) \right), \quad (2.18)$$

with

$$L_l(\eta) = \begin{pmatrix} \frac{l^2 I_l A_j}{\eta} & -ilCA_l & \frac{k_{\perp} l I_l B_l}{\Omega} \\ ilCA_l & FA_l & \frac{ik_{\perp} C B_l}{\Omega} \\ \frac{k_{\perp} l I_l B_l}{\Omega} & -\frac{ik_{\perp} C B_l}{\Omega} & \frac{2(\omega - l\Omega)}{k_{\parallel} v_{th\perp}^2} I_l B_l \end{pmatrix}, \quad (2.19)$$

where $I_l(\eta)$ is the modified Bessel function depends on the argument η . The following definitions are used:

$$\begin{aligned} \eta &= \frac{k_{\perp}^2 v_{\perp}^2}{2\Omega^2}, \\ F &= \frac{l^2}{\eta} I_l + 2\eta I_l - 2\eta I_l', \\ C &= I_l - I_l', \\ I_l' &= \frac{d}{d\eta} I_l(\eta) \\ A_l &= \frac{1}{\omega} \frac{T_{\perp} - T_{\parallel}}{T_{\parallel}} + \\ &\quad \frac{1}{k_{\parallel} v_{th\parallel}} \frac{(\omega - k_{\parallel} U - l\Omega) T_{\perp} + l\Omega T_{\parallel}}{\omega T_{\parallel}} Z_0(\zeta_l), \\ B_j &= \frac{1}{\omega k_{\parallel}} (\omega - k_{\parallel} U) + \frac{\omega - l\Omega}{k_{\parallel}} R_l, \end{aligned} \quad (2.20)$$

where $Z_0(\zeta_j)$ is the known dispersion function which depends of the cyclotron resonance argument

$$\zeta_j = \frac{\omega - k_{\parallel} U - l\Omega}{k_{\parallel} v_{th\parallel}}, \quad l = \pm 1, \pm 2, \pm 3, \dots \quad (2.21)$$

and the Landau resonance factor is determined by the case that $l = 0$. The polarization

P of the waves can be defined as (Stix, 1992)

$$P = i \frac{E_x \omega_r}{E_y |\omega_r|}, \quad (2.22)$$

where ω_r is the real part of the frequency $\omega = \omega_r - i\gamma$ (γ is the damping or the growth rate). E_x, E_y are the coordinates of the vector electric field $\delta\mathbf{E}$ along x and y axis.

2.3 Oblique fast waves in electron/proton plasma

2.3.1 Linear dispersion analysis

We study the properties of the fast waves in an electron-proton plasma in thermal equilibrium. Both species have isotropic Maxwellian VDFs, $T_{p\perp}/T_{p\parallel} = T_{e\parallel}/T_{e\perp} = 1$, describing the background state of the plasma. Here, we consider equivalent electron and proton plasma betas, i.e., a plasma with $\beta_e = \beta_p = 0.01$.

By solving the dispersion relation from eqs. (2.12) and (2.18), several plasma modes could appear. Among them we only deal with the fast mode which could be relevant for the heating and acceleration of protons. Here, we ignore the possible mode conversion of the fast waves with ion Bernstein waves than can occur in highly oblique propagation.

The top panels in Fig. 2.1 display the normalized real frequency, ω_r/Ω_p , of the fast waves propagating with angles $\theta = 20^\circ, 40^\circ, 60^\circ$ and 80° as well as the corresponding normalized damping rates, γ/Ω_p . In the right bottom panel of Fig.2.1, also the real and the imaginary part of the wave polarization are plotted for the same branches. It is clear that the fast mode is linear and corresponds to compressive Alfvén waves when $k v_A/\Omega_p \ll 1$ (v_A is Alfvén speed). At this limit, in the case of $\theta = 20^\circ$, the waves are linearly polarized, while the waves tend to be more circularly polarized ($Re(P) \sim 1$) when $k v_A/\Omega_p \sim 0.8$. For the same propagation angle, in Fig.2.1b the damping rate of the modes is weaker, and at certain values of $k v_A/\Omega_p$ the damping is slightly enhanced. These values of $k v_A/\Omega_p$ correspond to the region $\omega_r/\Omega_p \sim 1$ in Fig.2.1a, where the first harmonic cyclotron resonance condition $\omega_r \approx k_{\parallel} v_{\parallel} + \Omega_p$ is fulfilled. Notice that the enhancement in the damping rate is related to the enhancement in the imaginary part of the wave polarizations $Im(P)$. For the branch with propagation angle $\theta = 60^\circ$ a second visible bump appears in the damping rate and corresponds to $\omega_r \approx 2\Omega_p$. This enhancement also corresponds to a second enhancement in $Im(P)$, while, a second enhancement in the damping rate for $\theta = 20^\circ$ does not appear.

Fig.2.2 displays the snapshot of the the normalized real part of the frequency (ω_r/Ω_p) (left panel) and the damping rate (γ/Ω_p) as a function of $k v_A/\Omega_p$ (right panel) and the propagation angle θ . It turns out that the first, second and the third harmonic proton cyclotron resonance can help in dissipation of the fast mode. The first harmonic cyclotron resonance ($\omega_r \approx \Omega_p$), which belongs to the regions close to $k v_A/\Omega_p \sim 1$ in Fig.2.1b, starts occurring when the waves propagate with angles above 20° to quasi-perpendicular propagations. However, the damping via the second harmonic cyclotron resonance $\omega_r \approx 2\Omega_p$, which corresponds to the region with $k v_A/\Omega_p \sim 1.5$, is related to the waves propagating with angles above 40° . Furthermore, the strong dissipation of the waves having frequencies ($\omega_r \approx 2\Omega_p$) occurs when $\theta > 60^\circ$. The fast waves dissipation via the third harmonic

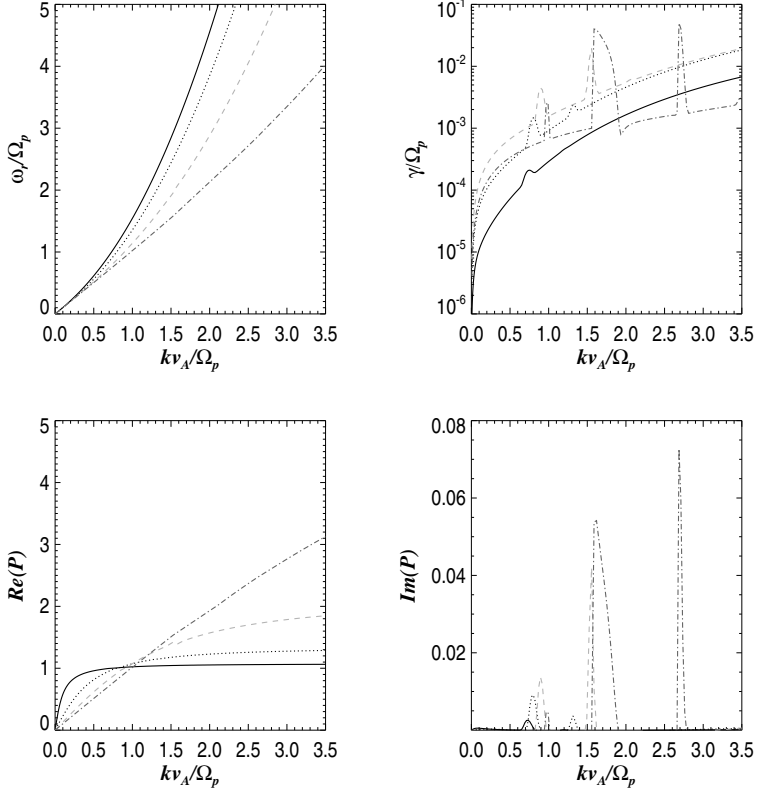


Figure 2.1: (a) and (b): The normalized frequency and the normalized damping rate, (c) and (d): The real and imaginary part of the polarization. All figures plotted, vs. the normalized wave vector for $\theta = 20^\circ$ (line), $\theta = 40^\circ$ (dotted-line), $\theta = 60^\circ$ (dashed-line) and $\theta = 80^\circ$ (dash-dotted line).

cyclotron resonance ($\omega_r \approx 3\Omega_p$) is very weak, and could be relatively strong only if $\theta > 80^\circ$ i.e., for quasi-perpendicular waves (see Fig.2.2b when $kv_A/\Omega_p \sim 2.7$).

Notice that the damping of the fast waves having nonresonant frequencies, $\omega_r \neq l\Omega_p$ ($l = 1, 2, 3$) shown by red color in Fig.2.2b, primarily comes from electron Landau resonance, $\omega_r = k_{\parallel}v_{\parallel,e}$. Within the domain of these nonresonant frequencies, both proton Landau and cyclotron damping are negligible. This is because, in low- β , the proton thermal velocity $v_{th,p} \ll v_{ph}$, which leads to the inequality $\omega_r \gg k_{\parallel}v_{\parallel,p}$ (where $v_{\parallel,p}$ is the proton velocity). Hence, proton Landau resonance condition would not be fulfilled. However,

due to the smallness of the electron mass relatively to the proton mass, the electron thermal speed $v_{th,e} \gg v_{th,p}$ when the thermal equilibrium condition is satisfied ($T_e = T_p$). Therefore, electron Landau resonance ($\omega_r \approx k_{\parallel} v_{\parallel,e}$) might be satisfied, then the dissipation of the fast waves can be achieved via electron Landau damping.

The damping of the fast mode by electron Landau resonance is more efficient for oblique waves having, $20^\circ < \theta < 80^\circ$, and then starts to decrease dramatically for quasi-perpendicular waves (see Fig.2.2b). Moreover, the electron Landau damping of these waves is proportional to the normalized wave number k_{VA}/Ω_p . There is no dissipation of the parallel and quasi-parallel fast waves neither via proton-cyclotron resonance nor via Landau damping.

Notice that for highly obliquely propagating fast waves with $\theta > 75^\circ$, the fast waves could convert into ion Bernstein waves. Hence, they also suffer from a first, second and third harmonic proton cyclotron absorption (see e.g., Li and Habbal 2001). The enhanced values of the imaginary part of the wave polarization $Im(P)$ displayed in Fig. 4.3, corresponds to the enhanced damping rate in the regions when the proton cyclotron resonances take place as shown in Fig.2.2b. In the regions where $Re(P) \sim 1$ and $Im(P)$ is small, the waves are right-handed circularly polarized.

Before we discuss the heating of the protons via their diffusion by fast magnetosonic waves in the next section, we reiterate some of the basic equations on the diffusion of the ions in general dispersive waves within the quasi-linear theory framework. In our analysis, we rather deal with the diffusion equation for reduced VDFs proposed by Marsch (1998, 2002) to compute the different fluid moment parameters.

2.3.2 Quasi-linear theory for reduced VDF

A detailed description of the QLT has been given in the text books by Stix (1992). QLT is quadratically nonlinear in the coupling terms between the plasma distributions and wave fields fluctuations. However, in this theory, still the linear wave dispersion with slowly time-varying VDFs and power spectrum density (PSD) is used for the wave field fluctuations.

The general quasi-linear diffusion equation that describes the evolution of the usual VDFs, $f(v_{\parallel}, v_{\perp}, t)$, of a homogeneous and magnetized plasma under the influence of an ensemble of fluctuation modes with index M , is given by

$$\frac{\partial f_s}{\partial t} = \sum_M \sum_{l=-\infty}^{\infty} \frac{1}{(2\pi)^3} \int_{-\infty}^{\infty} dk \mathfrak{B}_M \frac{1}{v_{\perp}} \frac{\partial}{\partial \alpha} \left(v_{\perp} v_s(\mathbf{k}, l; v_{\perp}, v_{\parallel}) \frac{\partial f_s}{\partial \alpha} \right), \quad (2.23)$$

where the gradient of the pitch-angle α is

$$\frac{\partial}{\partial \alpha} = v_{\perp} \frac{\partial}{\partial v_{\parallel}} - \left(v_{\parallel} - \frac{\omega_M(\mathbf{k})}{k_{\parallel}} \right) \frac{\partial}{\partial v_{\perp}}. \quad (2.24)$$

\mathfrak{B}_M is the power spectrum density (PSD) normalized to the background-magnetic field energy density, and the ion-wave relaxation rate ν_s is defined as

$$\nu_s(\mathbf{k}, l; v_{\perp}, v_{\parallel}) = \pi \Omega_s^2 \delta(\omega_M(\mathbf{k}) - s\Omega_s - k_{\parallel} v_{\parallel}) \times$$

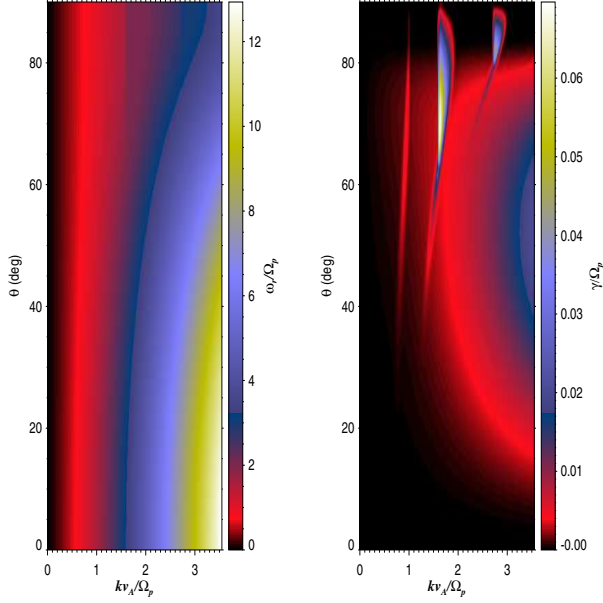


Figure 2.2: Snapshots showing in colour coding the normalized frequency (left panel) and the normalized damping rate (right panel) as a function of the normalized wave vector and the propagation angle θ .

$$\left| \frac{1}{2} (J_{s-1}(\eta)E_M^+ + J_{s+1}(\eta)E_M^-) + \left(\frac{\omega_M(\mathbf{k}) - s\Omega_s}{v_\perp k_\parallel} \right) J_s(\eta)E_{Mz} \right|^2, \quad (2.25)$$

where $\eta = \frac{k_\perp v_\perp}{\Omega}$, and the left (right) handed components of the wave polarization vector, E^+ (E^-), are defined by

$$E^\pm = E_x \pm iE_y. \quad (2.26)$$

Note that, the pitch-angle α designates the angle between the vector velocity and the mean magnetic field \mathbf{B}_0 in the wave frame of reference. Therefore, the vanishing of the angle gradient ($\partial/\partial\alpha$) leads to the so-called quasi-linear plateau formation whereby the plasma relaxes in its steady state. Also, in the case of a low β , the VDFs saturates and its evolution switches off when the bulk speed of the species reaches the phase speed.

In the following, we demonstrate that diffusion equations for the reduced VDFs in the moving frame of the species s that can be obtained from the general diffusion eq. (2.23). The k -th order reduced VDFs is defined as (Marsch 1998)

$$F_k(v_\parallel) = 2\pi \int_0^\infty v_\perp^{2k+1} f(v_\parallel, v_\perp) dv_\perp, \quad k = 0, 1, 2, \dots \quad (2.27)$$

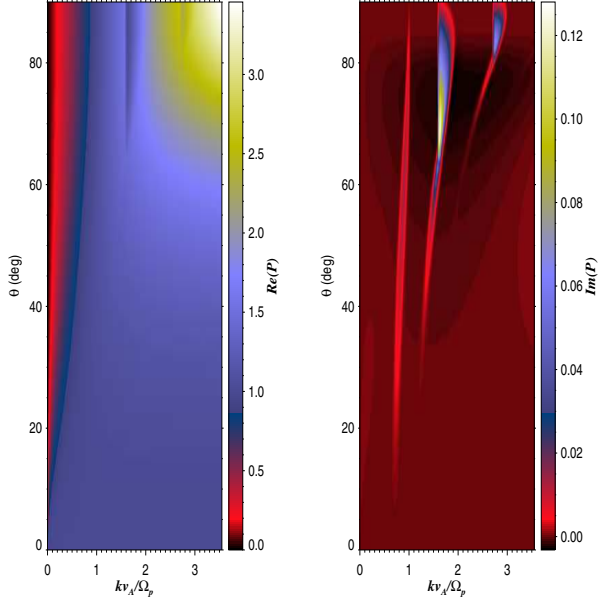


Figure 2.3: Snapshots showing in colour coding the real part (left panel) and the imaginary part (right panel) of the wave polarization as a function of the normalized wave vector and the propagation angle θ .

Here, the parallel velocity is shifted, $v_{\parallel} \rightarrow v_{\parallel} - U_s$ in order to express the different equations in the moving frame of the species, s . From the first two reduced VDFs, F_0 and F_1 , it is now possible to obtain all the relevant plasma fluid parameters. By integration of F_0 over various powers of v_{\parallel} we get the particle density N , drift velocity U_s parallel temperature T_{\parallel} , and heat flux. Considering also the moments of F_1 , the perpendicular temperature T_{\perp} and the perpendicular heat flux component can be obtained.

The diffusion equation of the two first reduced velocity distribution functions can be calculated by taking the corresponding moments of the diffusion eq. (2.23), i.e.,

$$\frac{\partial F_0(v_{\parallel})}{\partial t} = 2\pi \int_0^{\infty} dv_{\perp} v_{\perp} \frac{\partial f(v_{\parallel}, v_{\perp}, t)}{\partial t}, \quad (2.28)$$

$$\frac{\partial F_1(v_{\parallel})}{\partial t} = 2\pi \int_0^{\infty} dv_{\perp} v_{\perp}^3 \frac{\partial f(v_{\parallel}, v_{\perp}, t)}{\partial t}. \quad (2.29)$$

By inserting (2.23) and integrating over v_{\perp} , the evolution equation of $F_0(v_{\parallel})$ and $F_1(v_{\parallel})$

take the following general form

$$\frac{\partial F_0(v_{\parallel})}{\partial t} = \frac{\partial}{\partial v_{\parallel}} \left(D(v_{\parallel}) \frac{\partial F_1(v_{\parallel})}{\partial v_{\parallel}} \right) - \frac{\partial}{\partial v_{\parallel}} (A^+(v_{\parallel}) F_0(v_{\parallel})), \quad (2.30)$$

$$\begin{aligned} \frac{\partial F_1(v_{\parallel})}{\partial t} &= \frac{\partial}{\partial v_{\parallel}} \left(D(v_{\parallel}) \frac{\partial F_2(v_{\parallel})}{\partial v_{\parallel}} \right) - 2 \frac{\partial}{\partial v_{\parallel}} (A^+(v_{\parallel}) F_0(v_{\parallel})) \\ &\quad + A^-(v_{\parallel}) \frac{\partial F_1(v_{\parallel})}{\partial v_{\parallel}} - H(v_{\parallel}) F_0(v_{\parallel}), \end{aligned} \quad (2.31)$$

where D , A^{\pm} and H respectively are the diffusion, acceleration and heating coefficients. These reduced VDFs forms given by (2.30) and (2.31) are obtained assuming $f(v_{\parallel}, \infty) = f(\infty, v_{\perp}) = 0$, and also vanishing derivative at infinity such that $|\partial f / \partial v_{\perp}|_{v_{\perp}=\infty} = 0$.

In order to explicitly extract the forms of the diffusion operators, D , A^{\pm} and H , we simply chose the typical value, $v_{th\perp}$ for the perpendicular velocity, v_{\perp} , in the relaxation rate. Then we have

$$\begin{pmatrix} D_s(v_{\parallel}) \\ A_s(v_{\parallel}) \\ H_s(v_{\parallel}) \end{pmatrix} = \sum_M \sum_{l=-\infty}^{\infty} \frac{1}{(2\pi)^3} \int_{-\infty}^{\infty} dk \hat{\mathfrak{B}}_M \bar{v}_s(\mathbf{k}, l; v_{\parallel}) \begin{pmatrix} 1 \\ \frac{l\Omega_s}{k_{\parallel}} \\ \left(\frac{l\Omega_s}{k_{\parallel}}\right)^2 \end{pmatrix}, \quad (2.32)$$

where

$$\begin{aligned} \bar{v}_s(\mathbf{k}, l; v_{\parallel}) &= \pi \Omega_s^2 \delta(\omega_M(\mathbf{k}) - s\Omega_s - k_{\parallel}v_{\parallel}) \\ &\quad \times \left| \frac{1}{2} (J_{s-1}(\bar{\eta}) E_M^+ + J_{s+1}(\bar{\eta}) E_M^-) + \left(\frac{\omega_M(\mathbf{k}) - s\Omega_s}{k_{\parallel}} \right) J_s(\bar{\eta}) E_{Mz} \right|^2, \end{aligned} \quad (2.33)$$

with $\bar{\eta} = \frac{k_{\perp} v_{th\perp}}{\Omega}$.

Note that for higher order reduced VDFs with, $k > 1$, a Gaussian approximation in v_{\perp} is assumed, which allows us to introduce the following closure relations:

$$F_k(v_{\parallel}) = k! (2v_{th\perp})^{k-1} F_1(v_{\parallel}), \quad k = 2, 3, 4, \dots \quad (2.34)$$

Now, it is possible to calculate the acceleration and heating rates. Then the first moment gives the bulk acceleration:

$$\frac{\partial}{\partial t} U = \int_{-\infty}^{\infty} dv_{\parallel} v_{\parallel} \frac{\partial F_0(v_{\parallel})}{\partial t}, \quad (2.35)$$

and the second moment of F_0 and zeroth moment of F_1 give the parallel and perpendicular heating rates:

$$\frac{\partial}{\partial t} v_{th\parallel}^2 = \int_{-\infty}^{\infty} dv_{\parallel} v_{\parallel}^2 \frac{\partial F_0(v_{\parallel})}{\partial t}, \quad (2.36)$$

$$\frac{\partial}{\partial t} v_{th\perp}^2 = \int_{-\infty}^{\infty} dv_{\parallel} \frac{\partial F_1(v_{\parallel})}{\partial t}. \quad (2.37)$$

By performing these integrations over v_{\parallel} after inserting the diffusion operators given

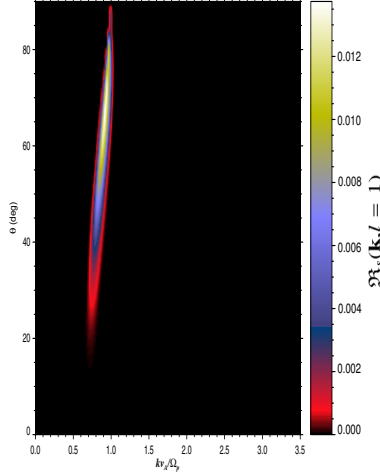


Figure 2.4: Snapshot showing the first harmonic resonance function as a function of the normalized wave vector and the propagation angle θ .

by eq. (2.32) into equations (2.35), (2.36) and (2.37), the final forms of the different rates are (Marsch 2001):

$$\begin{aligned} \left(\begin{array}{c} \frac{\partial}{\partial t} U_s \\ \frac{\partial}{\partial t} v_{th\parallel,s}^2 \\ \frac{\partial}{\partial t} v_{th\perp,s}^2 \end{array} \right) &= \sum_M \frac{1}{(2\pi)^3} \int_{-\infty}^{\infty} d^3k \mathfrak{B}_M(\mathbf{k}) \left(\frac{\Omega}{k_{\parallel}} \right)^2 \\ &\times \sum_{j=-\infty}^{\infty} \mathfrak{R}_s(\mathbf{k}, l) \left(2k_{\parallel} \left(\frac{\omega_M(\mathbf{k}) - j\Omega_s}{k_{\parallel}} - U_s \right) \right). \end{aligned} \quad (2.38)$$

These rates are expressed in terms of integrals over the normalised PSD and sums over the mode number, M , and resonance harmonic number l , and the resonant function $\mathfrak{R}_s(\mathbf{k}, l)$ which depends on the wave number \mathbf{k} and on the reduced VDFs $F_{\parallel s}(v_{\parallel})$ and $F_{\perp s}(v_{\perp})$ such that

$$\begin{aligned} \mathfrak{R}_s(\mathbf{k}, l) &= (2\pi)^2 \frac{k_{\parallel}}{|k_{\parallel}|} \left| \frac{1}{2} (J_{s-1}(\eta) E_M^+ + J_{s+1}(\eta) E_M^-) + \left(\frac{\omega_M(\mathbf{k}) - s\Omega_s}{k_{\parallel}} \right) J_s(\eta) E_{Ms} \right|^2 \\ &\times \left[\left(\frac{l\Omega}{k_{\parallel}} F_{\parallel s} - \frac{\partial}{\partial v_{\parallel}} F_{\perp s} \right) \right]_{v_{\parallel} = \frac{\omega_M(\mathbf{k}) - s\Omega_s}{k_{\parallel}} - U_s}. \end{aligned} \quad (2.39)$$

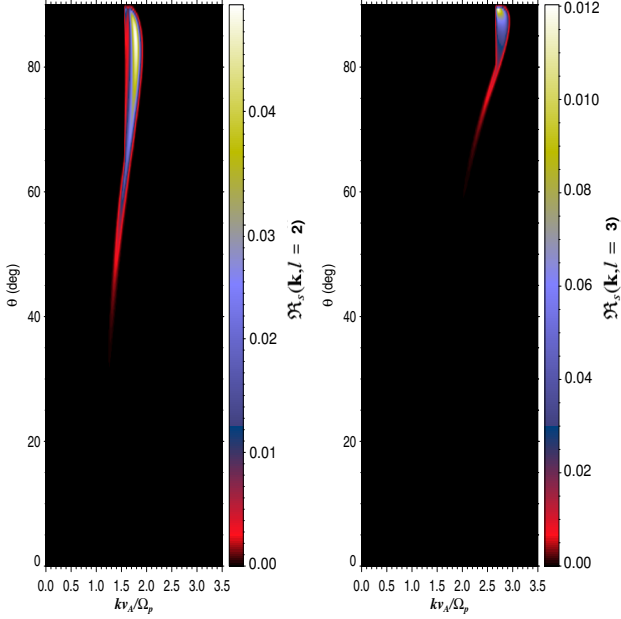


Figure 2.5: Snapshots showing the second harmonic (left) and third harmonic (right) resonance function as a function of the normalized wave vector and propagation angle θ .

2.3.3 Proton heating by oblique fast waves

Now we investigate the heating and the acceleration of the protons through the diffusion of these latter by the oblique fast waves studied in subsection (2.3.1). For this purpose, we compute the different rates given by eq. (2.38). Here, we approximate the evolving proton VDFs by a bi-Maxwellian, with $v_{th\parallel}$ and $v_{th\perp}$ being the parallel and perpendicular thermal speed of the proton. Hence, the general expressions of $F_0(v_{\parallel})$ and $F_1(v_{\parallel})$ as obtained from standard bi-Maxwellian VDFs $f(v_{\parallel}, v_{\perp})$ can be computed from eq. (2.34),

$$F_0(v_{\parallel}) = \frac{n_0}{\sqrt{2\pi}v_{th\parallel}} \exp\left(-\frac{(v_{\parallel} - U)^2}{2v_{th\parallel}^2}\right), \quad (2.40)$$

$$F_1(v_{\parallel}) = \frac{n_0}{\sqrt{2\pi}} \frac{v_{th\perp}^2}{v_{th\parallel}} \exp\left(-\frac{(v_{\parallel} - U)^2}{2v_{th\parallel}^2}\right). \quad (2.41)$$

From these expressions, the harmonic resonance function can be explicitly computed, and is found to depend also on $v_{th\parallel}$ and $v_{th\perp}$ in addition to the wave polarizations and wave frequency ω , i.e.:

$$\mathfrak{R}_s(\mathbf{k}, l) = (2\pi)^2 \frac{k_{\parallel}}{|k_{\parallel}|} \left| \frac{1}{2} (J_{s-1}(\eta) E_M^+ + J_{s+1}(\eta) E_M^-) + \left(\frac{\omega_M(\mathbf{k}) - l\Omega_s}{k_{\parallel}} \right) J_s(\eta) E_{Mz} \right|^2 \quad (2.42)$$

$$\times \left[\frac{\omega_M(\mathbf{k}) - l\Omega_s}{k_{\parallel} v_{th\parallel}^2} \frac{v_{th\perp}^2}{v_{th\parallel}} + \frac{l\Omega_s}{k_{\parallel} v_{th\parallel}} \right] \exp \left(-\frac{1}{2} \left(\frac{\omega_M(\mathbf{k}) - l\Omega_s}{k_{\parallel} v_{th\parallel}} \right)^2 \right), \quad (2.43)$$

where the integer number l is related to the harmonic proton-cyclotron resonance condition, $\omega_r - kv_{\parallel} - l\Omega$. Due to the exponential term this function is very small for all values of k except close to the domain (k, θ) when the l harmonic proton-cyclotron resonance condition is fulfilled.

At initial time, $t = 0$, the electron-proton plasma is assumed to be in equilibrium state (the VDF is a Maxwellian) with $v_{th\parallel}/v_A = v_{th\perp}/v_A = \sqrt{\beta}$ with $\beta = 0.01$. The initial plasma is at the same conditions for which the fast-wave dispersion is computed (see subsection 2.3.1).

Fig.2.4 and Fig.2.5 show the numerically computed resonance function $\mathfrak{R}_s(\mathbf{k}, l)$ at $t = 0$ plotted for $l = 1, 2, 3$. It turns out that the resonance function does not vanish only near those regions of kv_A/Ω_p where resonant interactions are taking place, $\omega_r \approx l\Omega_p$, i.e. the harmonic resonance function computed via quasi-linear theory reflects the same behaviour of the linear damping rate as plotted in Fig.2.2b. However, in the case of the harmonic resonance function only the wave-proton interactions are considered, and it turns out that the harmonic resonance function for $l = 1, 2$ and 3 describes the possible wave-proton interactions via first, second and third harmonic proton-cyclotron resonance as shown before in Fig.2.2 in the case of linear wave analysis. For $l = 1$ (see Fig.2.4), only oblique waves having propagation angles between 40° and 80° contribute to the resonance function \mathfrak{R}_s , and waves propagating with angles above 40° contribute to the second harmonic resonance function (see Fig.2.5a). Furthermore, Fig.2.5b displays the third harmonic \mathfrak{R}_s , which shows the contribution of the quasi-perpendicular fast waves to the heating and acceleration of the protons.

Notice that, when $l = 0$, the resonance function $\mathfrak{R}_s \approx 0$, which means that the contribution of proton Landau damping in the heating and acceleration of protons is negligible. However in the case of electrons, $\mathfrak{R}_s(l = 0)$ would more or less contribute in electron diffusion, since electron Landau damping is considerable for obliquely propagating fast waves as indicated in subsection. (2.3.1).

The heating and acceleration rates can be computed once the normalized PSD, such that $\mathfrak{B}_M(\mathbf{k})$, of the branch is given. Here, we estimate the heating rate caused by a monochromatic wave with propagation angle θ . In our calculation, the power-law form for the normalized PSD is assumed, $\mathfrak{B}_M(\mathbf{k}) = \alpha/\bar{k}$, where α is a constant dimensionless parameter, and the normalized wave number $\bar{k} = kv_A/\Omega_p$. Here, to compute the heating and acceleration of the proton species by the oblique fast waves, we approximate the evolving VDFs to a bi-Maxwellian in which $v_{th\parallel}$, $v_{th\perp}$ and U are self-consistently updated from the diffusion equation (2.38) at each time step. Also, within the time-evolution interval, we assume that the fast wave dispersion is slowly varying in time, therefore, the dispersion of the waves is evaluated at larger time step.

In our calculation we have used normalized parameters such as normalized frequency,

$\bar{\omega} = \omega/\Omega_p$, normalized proton parallel and perpendicular speed, $\bar{V}_{\parallel,\perp} = v_{th\parallel,\perp}/v_A$, normalized proton drift speed, $\bar{U} = U/v_A$, and finally, the effective normalized time, $\tau = \alpha\Omega_p t$. Also, we denote by $Q_{\parallel,\perp} = \partial\bar{V}_{\parallel,\perp}^2/\partial\tau$, and $\mathbb{U} = \partial\bar{U}/\partial\tau$, respectively, the normalized parallel (perpendicular) heating rate, and the normalized acceleration rate.

Fig.2.6 and Fig.2.6 respectively display the evolution of the normalized bulk speed and perpendicular proton thermal speed as a function of the propagation angle of the fast waves with respect to the mean magnetic field \mathbf{B}_0 . It turns out that the fast mode heats perpendicularly the protons, since the heating in the parallel direction is very small. Therefore, the waves produce an anisotropic proton temperature with a preferential perpendicular heating ($T_{\perp} > T_{\parallel}$). Furthermore, the waves can also accelerate the protons from zero bulk speed to a value of about $0.01v_A$ when $\tau \sim 1$. If we assume that the normalized PSD is about 10^{-4} , then the proton can be heated roughly by a factor of two within time $t \sim \frac{10^4}{\Omega_p}$.

The oblique propagating waves with, $40^\circ < \theta < 80^\circ$ have a large impact on the heating and acceleration of the protons. However, parallel waves have no influence on the diffusion of the proton, and a negligible effect of the fast waves having θ less than 20° on the proton diffusion. Fast waves propagating with $60 \leq \theta \leq 65^\circ$ heat the protons more in the perpendicular direction, and strongly accelerate the proton in the direction of the mean magnetic. The heating and the acceleration of the protons comes primarily from the first and the second harmonic proton cyclotron absorption. However, the protons are less energized by waves propagating with θ below 25° since, the first resonance function $\mathfrak{R}_s(\mathbf{k}, l = 1) \ll 1$ within the domain of those waves.

2.4 Conclusion

In this chapter, the linear analysis of the wave dispersion in magnetized homogeneous and collisionless plasma is adopted to study the oblique fast waves (waves having phase speed $v_{ph} \geq v_A$). This approach can be applied to the outer corona and solar wind medium where the Coulomb collisions are negligible and the wave energy density is smaller than the background magnetic field energy density.

In this study, it is shown that the dissipation of the fast mode can be achieved via the three first harmonic proton-cyclotron resonances, $l = 1, 2, 3$. Furthermore, the dissipation of the fast mode via electron Landau resonance is considerable for obliquely propagating waves, while the damping via proton Landau is negligible. Moreover, only fast waves having propagation angle, $\theta > 20^\circ$ can dissipate. The dissipation of the fast waves via the third harmonic proton-cyclotron resonance can be achieved only in case of quasi-perpendicular propagation. The heating and the acceleration of the protons by the fast mode is described by the quasi-linear diffusion theory of the reduced velocity distribution function, where it is shown that the protons are more heated and accelerated through the dissipation of the fast waves propagating with angle close to 62° .

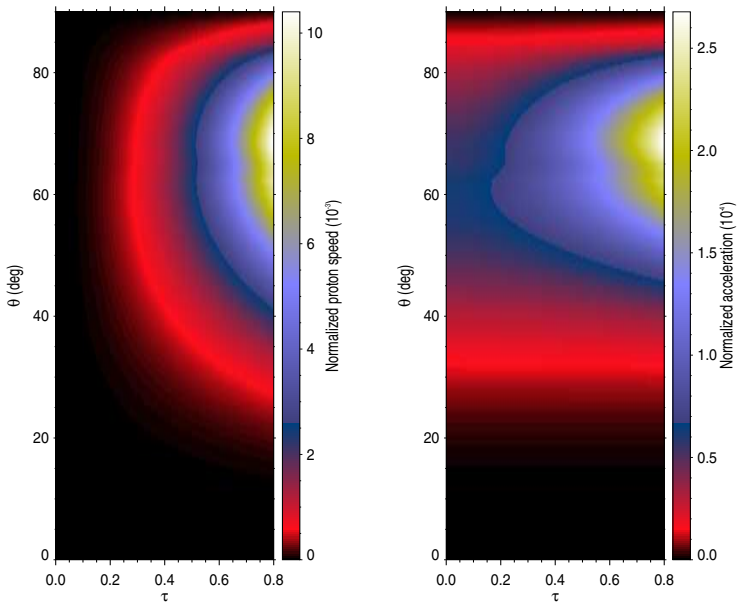


Figure 2.6: Snapshots showing the normalized proton drift speed (left panel), and the normalized acceleration rate (right panel) as a function of the normalized time and the propagation angle θ .

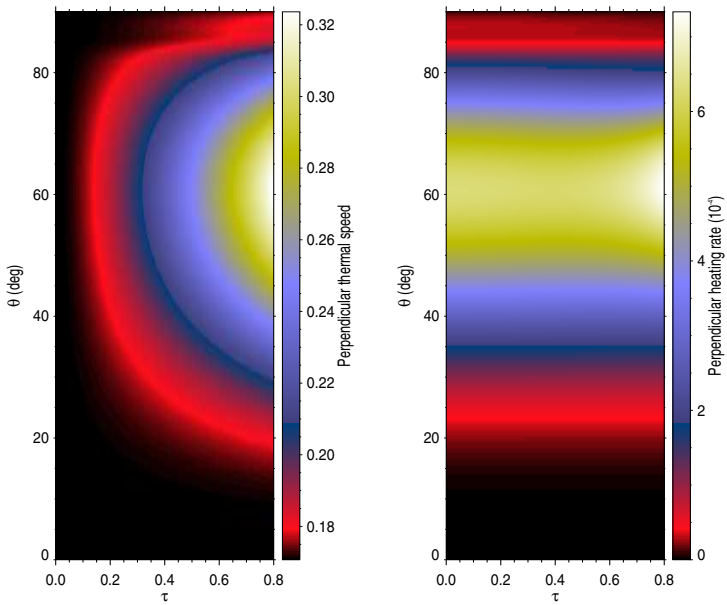


Figure 2.7: Snapshots showing the normalized perpendicular proton thermal speed (left panel), and the normalized perpendicular heating rate (right panel) as a function of the normalized time and the propagation angle θ .

3 On the efficiency of nonresonant ion heating by coronal Alfvén waves

3.1 Introduction

Low-frequency waves in the solar corona have for decades been studied using fluid theory (see, e.g., the recent review by Ofman (2005), and often been proposed to heat the corona via collisional dissipation, and to accelerate the solar wind by the wave pressure-gradient force. However, Coulomb collisions are rare in the solar corona and wind, and thus can not dissipate wave energy close to the sun (below the sonic point) by classical transport processes. Much less work has been done by employing kinetic theory. Recently, using the well known quasilinear theory (QLT) of weak plasma microturbulence in a novel approach, Wu and Yoon (2007) showed that wave-particle interactions can lead to proton heating by low-frequency Alfvén waves (i.e., by waves having much lower frequencies than the proton gyrofrequency) that interact nonresonantly with the protons in a strongly magnetized collisionless plasma. Their analytical results also appear to be consistent with the conclusions previously reached by Wang et al. (2006) and Li et al. (2007) using test-particle simulations.

Here we will show that this nonresonant heating, which occurs perpendicularly to the mean magnetic field, may be relevant for the heating of coronal ions. Thus our finding may alter the widely spread opinion that the ion temperature anisotropy observed in coronal holes (see e.g., Kohl et al. 1997, Frazin et al. 2003) must be a consequence of resonant ion-cyclotron wave absorption. These important remote-sensing observations support the idea that heavy ions are perpendicularly heated by cyclotron resonance. Furthermore, in-situ observations in the solar wind lead one to believe that mostly resonant diffusion in the ion-cyclotron-wave field causes the observed plateau formation in measured proton VDFs (Heuer and Marsch 2007). All these phenomena can well be described using traditional QLT, if the wave amplitudes are sufficiently small, as indeed can be assumed in the corona. Results have been successfully obtained with this approximation, e.g., in coronal funnel by Vocks and Marsch (2002), to explain the preferential heating of heavy minor ions like O^{3+} and Fe^{12+} . More recently, this approach was used also to model the thermal structure and extrem ultraviolet and X-ray emissions of coronal loops (Bourouaine et al. 2008a,b).

This Chapter is organized as follows: In Sec. 3.2 we present some recent observations of coronal Alfvén waves. Then, in Sec. 3.3 we mention some recent theories on the heating by low-frequency Alfvén waves. In Sec. 4 we briefly describe these interactions within quasi-linear theory. Then a parametric study of the ion heating and some numerical

results are given in Sec. 3.5. In Sec. 3.6, we study, including Coulomb collisions, the application of the wave heating mechanism to the lower corona. Finally, we summarize the obtained results in Sec. 3.7.

3.2 Observation of Coronal MHD Alfvén waves

The Alfvén mode is an incompressible transverse oscillation that propagates along the magnetic field lines. Researchers realized that Alfvén waves could transport energy from the oscillating turbulent solar photosphere into the solar corona, and thus, they might dissipate in the plasma leading to the coronal heating.

Alfvén waves have been detected through in-situ measurements in the solar wind for several decades (Tu and Marsch 1997). However, their observation in the solar corona has been lacking for two reasons. First, Alfvén waves are not visible as intensity fluctuations since they are incompressible, and therefore the intensity imagers used for coronal observations cannot detect them. Second, velocity fluctuations inferred from Doppler shifts emission lines require spectrograph or narrow-band graph filter measurements. Then, in most of observational works one used spectrographs that cannot observe over a large enough field and with a cadence sufficiently high to resolve the wave frequencies.

More recently, using the Fe^{+12} 1074.7 nm coronal emission line with the Coronal Multi-Channel polarimeter (CoMP) instrument, Tomczyk et al. (2007) have detected ubiquitous upward propagating waves, with phase speeds of 1 to 4 Mm s^{-1} propagating parallel to the magnetic field as it was inferred from the linear polarization measurements. These waves have been observed in the corona at altitudes between 1.05 and 1.35 R_{sun} . Fig. 3.2, shows CoMP solar observations. A Fourier analysis of the region of bright active region loops shows an enhanced, broad peak in the power spectrum of velocity fluctuations centred at ~ 3.5 mHz (5-min period) with a width of about 1 mHz. However, no peak appears in the corresponding power spectrum of intensity fluctuations or line width. The authors concluded that this result, besides the calculation of the phase speed and the almost zero propagation angle with respect to the magnetic field which is inferred from the linear polarization measurements, are a good indication that these waves are incompressible Alfvén waves having phase speed much larger than the sound speed (~ 2 Mm s^{-1}). It is also shown that the nonthermal component of coronal emission line widths is typically ~ 30 km s^{-1} .

Oscillations with 5-min period are not surprising because fluctuations in the corona with periods near 5-min have been widely observed as acoustic oscillation modes originating from the escaping photospheric 5-min acoustic oscillation (p modes) into higher layers via interactions with surface magnetic field.

More recently, Alfvén waves have also been observed by De Pontieu et al. (2007). The authors used images of high temporal (5 s) and spatial (150 km on the sun) resolution obtained with the Solar Optical Telescope (SOT) on board the Japanese Hinode satellite to reveal the existence of Alfvén waves in chromosphere and lower corona. These observed waves have strong amplitudes on the order of 10 to 25 km s^{-1} and periods of 100 to 500 s. By analysing several times series of chromospheric Ca II H-line (3968Å), it is found that the chromosphere is dominated by a multitude of thin (200 Km wide), dynamic, jetlike extrusions called spicules (see Fig. 3.3) that can reach heights between 2 and 10

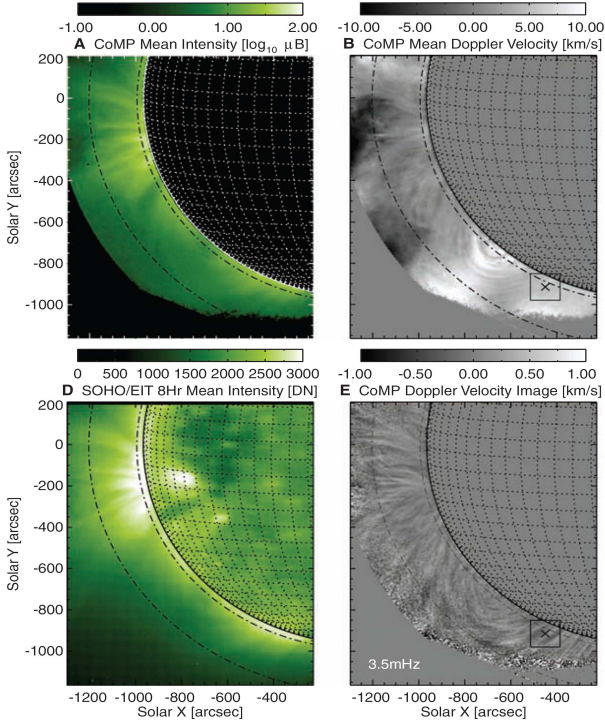


Figure 3.1: The CoMP observations of time-averaged intensity (A), Doppler velocity (B), 3.5-mHz filtered Doppler velocity (E). (D) SOHO/EIT 19.5-nm image averaged over the same time. Dot-dashed lines are representing distances of 5 and 25 percent of of solar radii. Tomczyk et al. (2007)

Mm. Many of these chromospheric spicules undergo substantial transverse displacements on the order of 500 to 1000 km during their short lifetimes of 10 to 300 s. It shown that, some longer-lived spicules undergo oscillatory motion in a direction perpendicular to their own axis (see Fig. 3.3a), with the displacement varying sinusoidally in time with a period of 3 min. Since the the spicules are formed at heights where the plasma-beta is small, they outline the direction of the magnetic field. As a result, these transverse oscillatory motions to the long axis of spicules implies the presence or passage of Alfvénic waves motions. Also, these waves could be interpreted as MHD kink-mode waves.

By taking the value of the observed nonthermal velocity $\delta v \approx 20$ km/s, the spicule mass density, $\rho = 2.2 \times 10^{-11}$ to 2.2×10^{-10} kg m $^{-3}$, and spicules magnetic fields $B \approx 10^{-3}$, the estimated energy flux of these waves in the chromosphere is $E = \rho < \delta v^2 > v_A = 4$ to 7 kW m $^{-2}$ (with Alfvén speed that is taken between 50 to 200 km/s). This energy flux

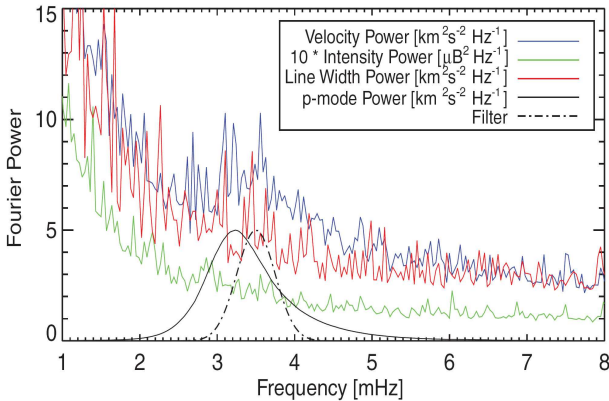


Figure 3.2: Fourier power spectrum of the Comp Doppler velocity (blue), intensity (green), and line width (red). The Gaussian filter applied in the analysis (dot-dashed black line) and the average power spectrum of intermediate degree photospheric oscillations (solid black line). Tomczyk et al. (2007)

carried by these waves indicate that such Alfvén waves are energetic enough to accelerate the solar wind and possibly to heat the quiet corona.

3.3 Ion heating by Alfvén waves (test-particle simulation)

Using test-particle simulation, (Wang et al. 2006, Li et al. 2007) demonstrate that the ions can be heated by Alfvén waves (having higher frequencies than the observed Alfvén waves) via nonresonant nonlinear interaction. Thus, it is shown that the lower the plasma beta value, the more effective is the heating process. Furthermore, the authors showed that the heating of ions is more prominent along the perpendicular direction.

Their simulation is based on the 1D equation of motion of a particle under the effect of a constant magnetic field, $\mathbf{B}_0 = B_0 \mathbf{i}_z$, and parallel propagating Alfvén waves, i.e.,

$$m \frac{d\mathbf{v}}{dt} = q [\delta \mathbf{E}_w + \mathbf{v} \times (\mathbf{B}_0 + \delta \mathbf{B}_w)], \quad (3.1)$$

$$\frac{dz}{dt} = v_z, \quad (3.2)$$

with the wave electromagnetic field $\delta \mathbf{E}_w$ and $\delta \mathbf{B}_w$ are chosen to have right-hand circular polarization:

$$\delta \mathbf{B}_w = B_k (\cos \phi_k \mathbf{i}_x + \sin \phi_k \mathbf{i}_y), \quad (3.3)$$

$$\delta \mathbf{E}_w = -\frac{v_A \mathbf{B}_0}{c B_0} \times \delta \mathbf{B}_w, \quad (3.4)$$

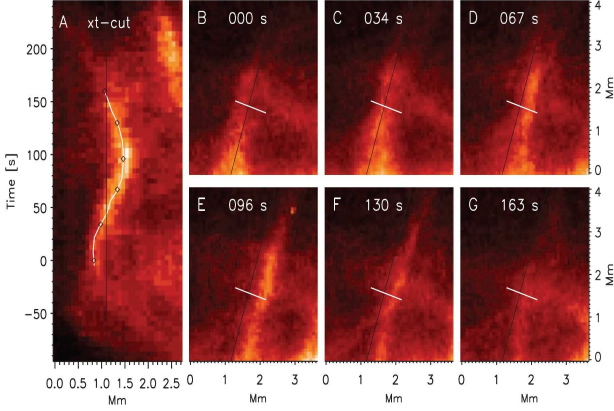


Figure 3.3: Example of the transverse displacement of a spicule: (A) the intensity as a function of time (represents the bulk motion) along the spatial cut (in Mm) shown by the white line in (B) to (F). This motion is consistent with the propagation along the spicule of an Alfvén wave with a large wavelength (>4 Mm). (B) to (G); A time series of Ca II H 3968 Å images from the Hinode SOT (movie S1), and the white line shows the extent of the transverse displacement of the spicule (black guide line). De Pontieu et al. (2007)

where $(\hat{\mathbf{i}}_x, \hat{\mathbf{i}}_y, \hat{\mathbf{i}}_z)$ are the unit vectors, and $\phi_k = k(v_A t - z)$ denotes the wave phase.

When a low β is assumed and by considering Alfvén waves having frequencies ranging between $0.01\Omega_p < \omega < 0.05\Omega_p$, i.e., the wave frequencies are much lower than the proton gyrofrequency, Ω_p , it is shown that the protons can be heated along the perpendicular direction with respect to the direction of the mean magnetic field, \mathbf{B}_0 . The amount of energy transferred to the protons is proportional to, $\delta B_\omega^2 / |\mathbf{B}_0|^2$ which is the averaged energy content of the Alfvén waves normalized to the magnetic energy density.

Fig. 3.4 displays the scattered test particles in the $v_{\parallel} - v_{\perp}$ plane at different time evolution and for input parameters $(\delta B_\omega^2 / B_0^2, v_{th,p} / v_A) = (0.05, 0.07)$. In this plot the initial particle velocities (at $\Omega_p t = 0$) are assumed to have a Maxwellian distribution with thermal speed, $v_{th,p}$ which is less than v_A to ensure that the cyclotron resonance condition cannot be fulfilled by the ions for these low-frequency Alfvén waves. When $\Omega_p t = 7$, it is clear that protons are scattered more towards the perpendicular direction. This means that Alfvén waves can result in nonresonant pitch-angle scattering of protons in low-beta plasma. This process is more efficient for proton heating when the averaged wave energy is large. Moreover, from Fig. 3.5, it turns out that as long as the plasma beta is low the wave energy can effectively randomize the proton orbits, and this leads to higher kinetic temperatures in the directions transverse than the ambient magnetic field, \mathbf{B}_0 .

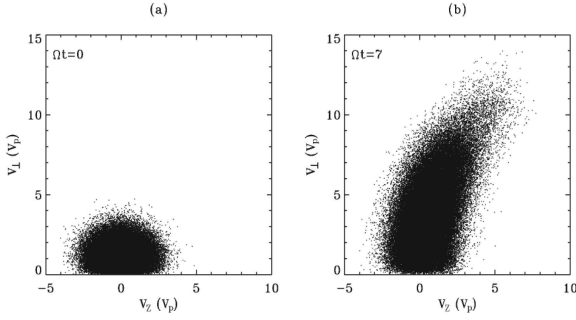


Figure 3.4: The Velocity scatter plots of the test particles with parallel (V_z) and perpendicular (V_\perp) velocity components (normalized to the proton thermal speed), at $\Omega t = 0$ (a) and $\Omega t = 7$ (b) for input parameters $(\delta B_w^2/B_0^2, v_p/v_a) = (0.05, 0.07)$. Li et al. (2007)

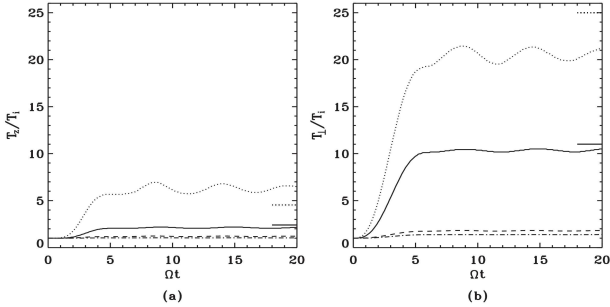


Figure 3.5: The temporal evolution of the parallel (a) and perpendicular (b) kinetic temperatures normalized to their initial values T_i : both plots are for input parameters, $(\delta B_w^2/B_0^2, v_p/v_a) = (0.05, 0.07), (0.12, 0.07), (0.05, 0.35)$ and $(0.12, 0.35)$. The results are represented by the solid line, the dots, the dash-dots, and the dashed line, respectively. The analytical results are indicated by the horizontal short lines for the cases $(\delta B_w^2/B_0^2, v_p/v_a) = (0.05, 0.07)$ and $(0.12, 0.07)$. Li et al. (2007)

3.4 Nonresonant wave-particle diffusion

Following the work of Marsch (1998, 2002), Vocks (2002), and Vocks and Marsch (2002) we derive below the different diffusion-type operators for the nonresonant wave-particle interaction terms in the kinetic equation. Starting point is the quasi-linear theory (see equations of the previous chapter) for a homogeneous magnetized plasma. In the case of

parallel propagating dispersionless Alfvén waves, this equation can be written as

$$\frac{\partial f_s}{\partial t} = \frac{1}{2} \int dk \frac{|\delta \mathbf{E}_k|^2}{B_0^2} \left(\frac{ck}{\omega_k} \right)^2 \frac{\gamma_k}{(\omega_k \pm \Omega_s - kv_{\parallel})^2 + \gamma_k^2} \frac{\partial}{\partial \alpha} \left(v_{\perp} \frac{\partial f_j}{\partial \alpha} \right), \quad (3.5)$$

with the gradient of pitch-angle diffusion is defined in eq(*), and the the spectral energy density of the electric field $|\delta \mathbf{E}_k|^2 = (v_A/c)^2 |\delta \mathbf{B}_k|^2$; γ_k is growth rate.

In the case of resonant quasilinear diffusion theory, the factor $\gamma_k [(\omega_k \pm \Omega_s - kv_{\parallel})^2 + \gamma_k^2]^{-1}$ can be approximated by $\pi \delta(\omega_k \pm \Omega_s - kv_{\parallel})$ in the limit $\gamma_k \rightarrow 0$. However, for Alfvén waves in low- β plasmas the inequalities, $\Omega_s \gg \omega_k \gg kv_{\parallel}$ and $\Omega_s \gg \gamma_k$, apply which means that the conditions for resonant interaction is not satisfied and instead we have:

$$\frac{\gamma_k}{(\omega_k \pm \Omega_s - kv_{\parallel})^2 + \gamma_k^2} \approx \frac{\gamma_k}{\Omega_s^2}. \quad (3.6)$$

By inserting this equality into eq. 3.5, we get

$$\frac{\partial f_s}{\partial t} = \int dk \frac{\partial}{4\partial t} \left(\frac{|\delta \mathbf{B}_k|^2}{B_0^2} \right) \frac{\partial}{\partial \alpha} \left(v_{\perp} \frac{\partial f_j}{\partial \alpha} \right) \quad (3.7)$$

In deriving the above equation we have made use of the evolution equation for the spectral wave energy density, i.e., $2\gamma_k |\delta \mathbf{B}_k|^2 = \partial |\delta \mathbf{B}_k|^2 / \partial t$.

Then, in the nonresonant limit, the diffusion operator for non-dispersive Alfvén waves can be written in a concise nonresonant form as

$$\frac{\partial f_s}{\partial \tau} = \frac{1}{4v_{\perp}} \frac{\partial}{\partial \alpha} \left(v_{\perp} \frac{\partial f_s}{\partial \alpha} \right), \quad (3.8)$$

where $\tau = \int dk B_k^2 / B_0^2$ is the integrated wave spectrum normalized to the energy density of the mean magnetic field. The variable τ plays the role of an effective diffusion time. This parameter has an upper limit, which should not exceed a value of say 0.05, in order to stay within the quasi-linear regime and fulfill the requirement of perturbation theory.

Here the treatment is not fully self-consistent in the sense that the Alfvén waves are assumed to be excited by an external source (e.g., a beam of high energetic ions) and propagate in the plasma. Here we do not study the mechanism that could generate these waves with growth γ_k .

In what follows we make use of the approximations made by Marsch (1998) for the diffusion equation and integrate equation (3.8) over the perpendicular speed. At this stage we therefore have to define the l th-order reduced VDF as follows:

$$F_l(v_{\parallel}) = 2\pi \int_0^{\infty} v_{\perp}^{2l+1} f(v_{\parallel}, v_{\perp}) dv_{\perp} \quad l = 0, 1, 2, \dots \quad (3.9)$$

Relevant plasma parameters (e.g., density, temperatures, and heat flux) can be obtained from $F_0(v_{\parallel})$ and $F_1(v_{\parallel})$. Generally, for any waves propagating parallel to the mean magnetic field, the combined diffusion equations for the two reduced VDFs can be written

(Marsch 1998) in the compact form:

$$\frac{\partial F_{j,0}}{\partial \tau} = \frac{\partial}{\partial v_{\parallel}}(D_j(v_{\parallel}) \frac{\partial F_{j,1}}{\partial v_{\parallel}}) - \frac{\partial}{\partial v_{\parallel}}(A_j^+(v_{\parallel}) F_{j,0}), \quad (3.10)$$

$$\begin{aligned} \frac{\partial F_{j,1}}{\partial \tau} &= \frac{\partial}{\partial v_{\parallel}}(D_j(v_{\parallel}) \frac{\partial F_{j,2}}{\partial v_{\parallel}}) - 2 \frac{\partial}{\partial v_{\parallel}}(A_j^+(v_{\parallel}) F_{j,1}) \\ &\quad + A_j^-(v_{\parallel}) \frac{\partial F_{j,1}}{\partial v_{\parallel}} - H_j(v_{\parallel}) F_{j,0}, \end{aligned} \quad (3.11)$$

where D_j , A_j^{\pm} and H_j respectively are the diffusion, acceleration and heating coefficients. In the case considered here of nonresonant wave-particle interactions, by using equations (3.8), (3.10) and (4.11), these coefficients simplify and read: $D_j = \frac{1}{8}$, $A_j^{\pm} = \pm \frac{1}{4}(v_A - v_{\parallel})$ and $H_j = -\frac{1}{2}(v_A - v_{\parallel})^2$. Similarly to the resonant case, here the diffusion process also switches off when the pitch-angle gradient in the wave frame of reference vanishes. Furthermore, the heating and acceleration cease when the particles' mean drift speed parallel to the background field matches the Alfvén speed. This final state may not be reached, though, since the averaged normalized wave energy (variable τ) is usually finite. Thus for a given value of τ , the achievable heating as well as acceleration of the ions will be limited.

If the collisions between the different ion species have to be taken into account (e.g., when we deal with the lower corona), the Coulomb collision term has to be added to the diffusion equation (3.5). Within the approximation of the reduced VDFs, the Coulomb collision term has in detail been calculated and evaluated by Vocks (2002). The diffusion equation now includes the sum of the wave-particle term given in (3.8) and the Coulomb collision term:

$$\frac{\partial F_{j,k}}{\partial \tau} = \left(\frac{\partial F_{j,k}}{\partial \tau} \right)_{w-p} + \left(\frac{\partial F_{j,k}}{\partial \tau} \right)_{Col}. \quad (3.12)$$

3.5 Heating of a collisionless multi-ions plasma

In the following parametric study, we discuss what is required for an efficient ion heating via nonresonant wave-particle diffusion without collisions. We consider a multi-ions, magnetized and homogeneous plasma, which consists of protons, helium and oxygen ions He^{2+} and O^{5+} (with the abundances $N_{\text{He}}/N_p = 0.1$ and $N_{\text{O}}/N_p = 10^{-3}$), and assume non-dispersive Alfvén waves propagating parallel to the magnetic field. Since we are interested in the nonresonant wave-particle interactions, the low-frequency Alfvén waves are assumed to have frequencies $|\gamma_k| < \omega_k \ll \Omega_i$. Also, since the plasma is assumed to be homogeneous on scales smaller than the density scale length, $L = n/(\partial n/\partial s)$ (with spatial coordinate s), the frequency range of the waves is limited by the inequality, $v_A/L < \omega_k \ll \Omega_i$, e.g., at lower heights in the corona $v_A/L \approx 1 \text{ s}^{-1}$, and the proton cyclotron frequency Ω_p could reach some 10^4 s^{-1} for a field B_0 of several gauss, and $|\gamma_k|$ can have values below 1 s^{-1} .

At the initial value of $\tau = 0$, which corresponds to no waves propagating in the plasma, all species are assumed to have the same initial temperature, $T_0 = 0.2 \text{ MK}$ (with initial proton thermal speed v_{th0}), and a Maxwellian velocity distribution. The diffusion of the

ions by Alfvén waves is connected to the evolution of the averaged wave amplitude. Here, we assume that the normalized wave energy τ ranges between 0.0 and 0.05. Within this interval, the QLT is still valid, as the wave amplitude is sufficiently small.

The numerical results for the heating profiles of the ion species are plotted in Fig. 3.6 for plasma $\beta = 2 \times 10^{-2}$ and 2.6×10^{-3} . It turns out that heating of the ions up to temperatures of (≥ 1 MK) is in fact possible via nonresonant wave-particle interactions. This heating requires a relatively large averaged wave amplitude and a small plasma β , since the heating mainly depends on the differential speed ($v_A - v_{||}$) in the diffusion coefficients, which can be high in very-low-beta plasma ($v_A \gg v_{||}$).

In accord with the results obtained by the test particle simulations (Wang et al. 2006, Li et al. 2007) shown in Fig. 3.4 and 3.5, our Fig. 3.6a,b show that the all ion species suffer strong perpendicular heating. In Fig. 3.6c,d, the anisotropy ratio is much larger in case of O^{3+} , which can reach up to 35 when the normalized wave amplitude is at its maximum value $\tau = 0.05$ and $\beta = 2.6 \times 10^{-3}$. A smaller anisotropy will be achieved when the waves interact with a lighter ion species, such as protons and helium ions. The protons are hardly heated up when the plasma β is about 10^{-2} (see Fig. 3.6b). This is so even when the wave amplitude reaches maximal values. However, the oxygen ions can be efficiently heated, and their perpendicular temperature can exceed 1 MK when the normalized wave amplitude obeys $\tau > 0.01$.

The preferential heating of heavy ions can clearly be seen in the results of our study. Fig. 3.6 shows that the ion temperature is proportional to the wave amplitude. A closer inspection of the numerical values for different ions in Figs. 3.6a,3.6b reveals that the temperature is inversely proportional to the plasma β , and proportional to the mass ratio m_i/m_p (with m_i and m_p being, respectively, the ion and proton mass).

Interestingly, this heating process does not involve the dissipation, and is reversible. Here the reversibility means that the temperature increases as the waves get amplified and decreases when the waves get damped having γ_k negative. It might be that this process will not provide a real heating which is irreversible, but rather gives an apparent or pseudo-heating which leads to an apparent temperature that is hardly distinguishable from the real temperature. This is still an open question of how to deal with this situation. But when the collisions are included (see next section), the reversibility can be broken and this pseudo heating can turn to a real heating. In the following, we simply adopt the previous appellation which is "heating" when dealing with the nonresonant interactions.

The perpendicular temperature of the three ions, proton, helium and oxygen ions are plotted as a function of the effective time evolution τ and the plasma beta that ranges between 10^{-4} and 10^{-3} (see Figs. 3.7,3.8). At a given beta value, one can clearly see the linear dependence of the perpendicular temperature on the effective time τ that represents the averaged wave-energy. While, at a fixed value of τ , the perpendicular temperature of the species is inversely proportional to beta. Moreover, Fig. 3.9 displays the ratio $(T_{\perp}/T_0) - 1$ of each species plotted as function of beta for several values of τ . As expected, as long as the wave power is high, the ratio $(T_{\perp}/T_0) - 1$ increases. Also this quantity is proportional to the ion mass and seems to satisfy the proportionality relation $(T_{i,\perp}/T_0 - 1) \propto (\tau/\beta) \times (m_i/m_p)$. These numerical results of nonresonant ion heating are consistent with analytical ones obtained previously by Wu and Yoon (2007), who derived them for the case of proton heating only.

The heating can be interpreted in terms of the diffusion of the full f and the reduced

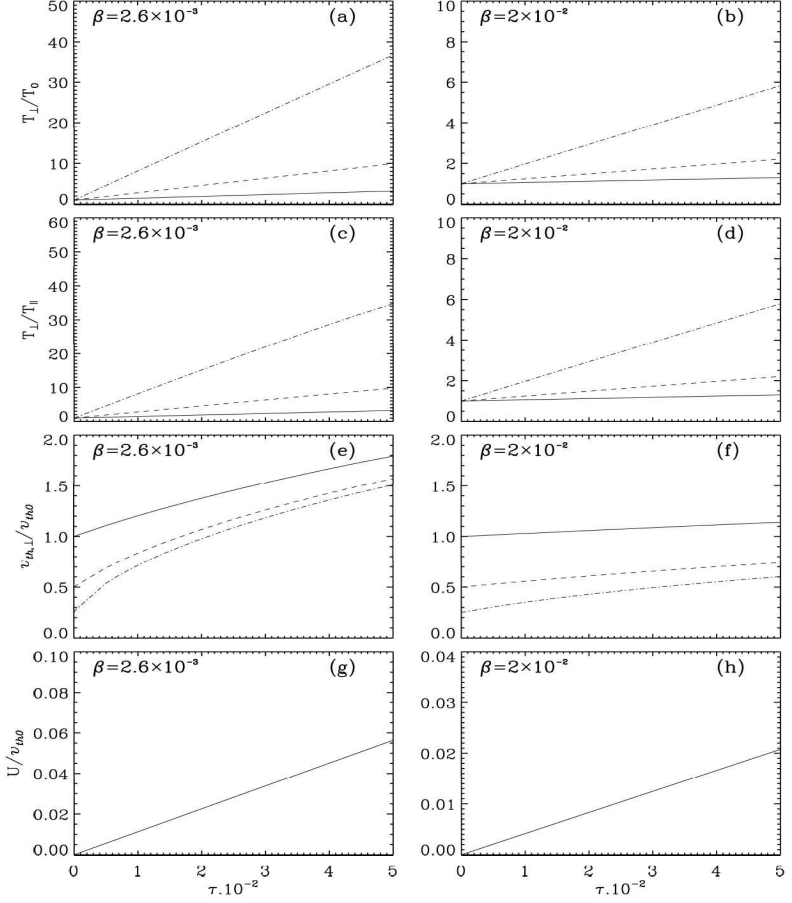


Figure 3.6: Various plasma parameters of the ions are plotted, on the left for $\beta = 2.6 \times 10^{-3}$ and the right for $\beta = 2 \times 10^{-2}$, versus the normalized wave energy τ : (a) and (b): Perpendicular temperature normalized to the initial temperature; (c) and (d): Ratio of the perpendicular over parallel temperature indicating the thermal anisotropy; (e) and (f): Normalized perpendicular thermal speeds; (g) and (h): Normalized drift speed which is the same for all ion species. Proton, helium and oxygen parameters are represented by solid, dotted and dash-dotted lines, respectively

(F_0, F_1) VDFs. The two reduced VDFs of oxygen ion are plotted in Fig. 3.10 for beta value $\beta = 2.6 \times 10^{-3}$. The solid-line in this figure represent the initial reduced F_0 and F_1 at $\tau = 0$, after a time designed by $\tau = 0.035$, the two reduced VDFs diffused and represented by the dot-line in the figure. It turns out that F_0 hardly evolves, while F_1 is more diffused by Alfvén waves. The diffusion process acts mainly on the ions with negative velocity since the Alfvén waves propagate along the direction of the mean magnetic field. For negative value of v_{\parallel} the heating diffusion operator H increases, consequently the diffusion of F_1 (which determines T_{\perp}) also increases, and thus the heating is more dominant in the perpendicular direction. Since F_0 (which determines T_{\parallel}) does not evolve considerably a slight increase in T_{\parallel} is expected.

The gyrotopropic VDF, f , which has an effective perpendicular temperature determined by F_1 , can be constructed from F_0 and F_1

$$f(v_{\parallel}, v_{\perp}) = \frac{F_0^2(v_{\parallel})}{F_1(v_{\parallel})} \exp \left[-\frac{v_{\perp}^2 F_0(v_{\parallel})}{F_1(v_{\parallel})} \right] \quad (3.13)$$

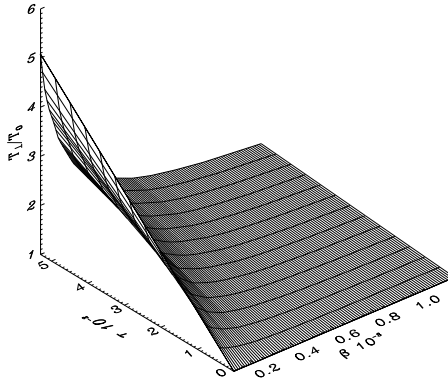
The resulting VDFs of the helium and oxygen ions are plotted in Fig. 3.11 for $\beta = 2 \times 10^{-2}$, 2.6×10^{-3} and $\tau = 0.035$. For heavy oxygen ions, the shape of these VDFs in the presence of low-frequency Alfvén waves is completely deformed from its initial Maxwellian form. This is due to the diffusion term which enforces motion on a circle centered in the Alfvén speed, and diffusion only comes to a stop for a vanishing pitch-angle gradient in the wave frame of reference. This process, which before was a consequence of a resonant interaction between cyclotron waves and particles (e.g., Heuer and Marsch (2007)), is now in the low-beta plasma a consequence of nonresonant interaction with low-frequency Alfvén waves, which drive the minor heavy ions more strongly to attain a VDF with vanishing pitch-angle gradient in the wave frame. This mechanism gives all minor heavy ions the same thermal speed when collisions are negligible and the wave energy is relatively large, as found in the solar wind (von Steiger et al. 1995).

It was shown in previous works (see, e.g., Ofman et al. 2001, 2002) that a perpendicularly heated ion VDF might in turn become unstable and produce ion-cyclotron fluctuations, if the temperature anisotropy exceeds a certain threshold value that depends on the plasma beta. In our model, the reached anisotropy could become a source of small-amplitude ion-cyclotron waves, in case of $\beta = 2.6 \times 10^{-3}$ and if τ is large enough, i.e., it must exceed roughly a value of 0.04. However, this possible instability does not affect the results essentially. Furthermore, in case of $\beta = 2 \times 10^{-2}$, the anisotropy obtained is not large enough for causing an instability. Certainly, the cyclotron-resonance instability provides a kinetic mechanism for limiting the anisotropy obtained nonresonantly.

3.6 Heating of the collisional lower corona

From the parametric study given in Sec. 3.3, it turns out that the nonresonant Alfvén waves may heat a collisionless model corona in which the plasma is highly dominated by the magnetic field pressure. However, in the real corona at lower altitudes collisions have to be accounted for. Here they still are efficient in comparison with the outer corona and the solar wind. Also, the time between ion collisions is shorter than the periods of the waves considered. To study the evolution including Coulomb collisions of the reduced

Perpendicular proton heating



Perpendicular helium ion heating

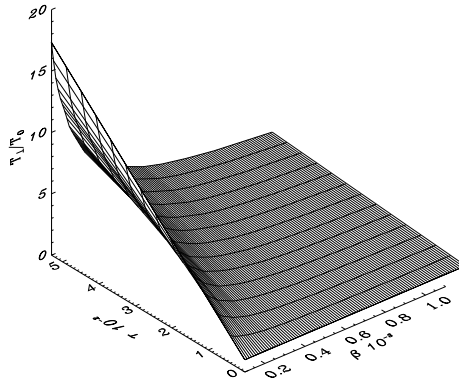


Figure 3.7: Perpendicular temperature normalized to the initial temperature plotted vs. plasma beta β and the effective time τ .

Perpendicular oxygen ion heating

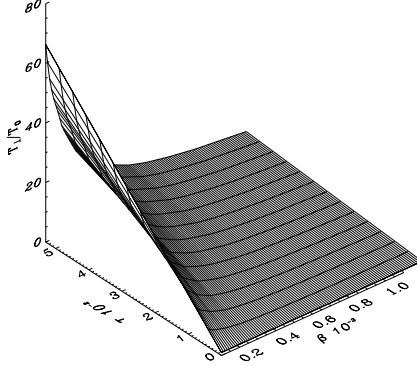


Figure 3.8: Perpendicular temperature normalized to the initial temperature plotted vs. plasma beta β and the effective time τ .

VDFs in dependence on τ , we consider a typical (at some lower altitudes in corona) proton density of $N_p = 10^{14} \text{ m}^{-3}$ with a helium abundance of $N_{He} = 0.1N_p$, and $N_{O^{5+}} = 10^{-3}N_p$, and assume $\partial\tau/\partial t \sim \tau\gamma$ with $\gamma \approx 1 \text{ s}^{-1}$.

One result from the collisional kinetic model is plotted in Fig. 3.12 for two values of the plasma β . All ion temperature profiles coincide, and thermal isotropy is now ensured due to the efficient collisions. The Alfvén waves tend to heat ions preferentially in the perpendicular direction, whilst the dominant collisions succeed in thermalizing all ions at the same temperature. Recent observations show that ion temperatures in the low corona do not differ drastically, yet there is weak evidence for preferential ion heating with mass per charge, which may be attributed to resonant cyclotron heating (e.g., see Dolla and Solomon (2008)). Collisions can thus help in rising the temperatures of protons and helium ions with respect to heavy ions. It appears that Alfvén waves can heat the lower corona, whereby collisions enforce isothermal conditions. The wave heating discussed here is of purely kinetic nature and has nothing to do with fluid-type dissipation through viscosity or resistivity. It does not rely on the existence of small gradient scales assumed in current and vorticity sheets, but occurs everywhere in a space-filling manner whenever there are Alfvén waves.

Past and recent observations of the coronal waves (see e.g., Nakariakov et al. (1999); (2001); Aschwanden et al. (2002); Ofman and Wang (2008); Wilhelm et al. (2007), Tomczyk et al. (2007)) show that the nonthermal velocity fluctuation amplitude δv , resulting possibly from Alfvén waves (with periods longer than three minutes), does not exceed 40 km s^{-1} . Then everything hinges on the Alfvén speed in the region of wave activ-

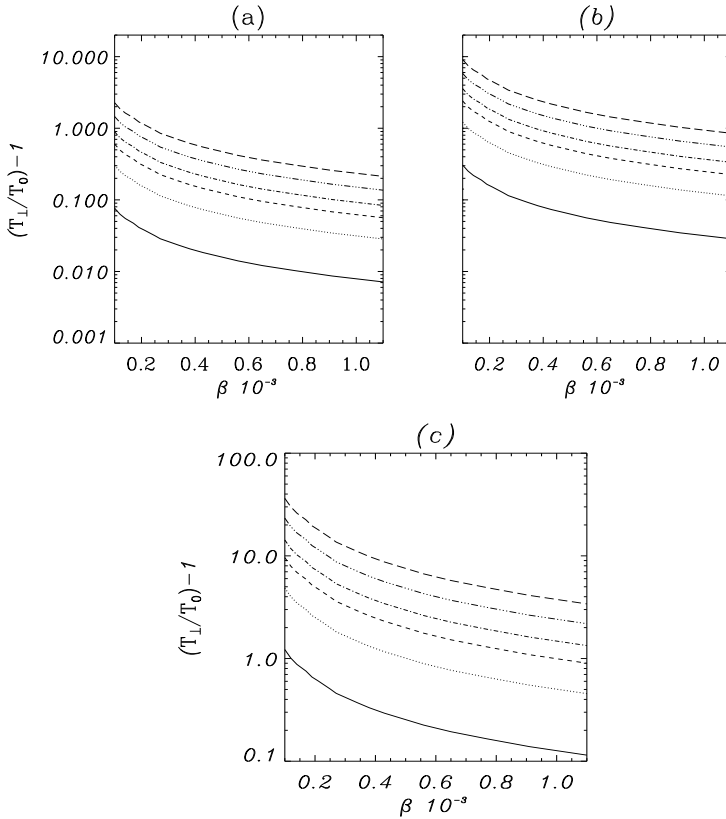


Figure 3.9: Anisotropy ratio given as function of plasma beta plotted for proton (a), helium (b) and oxygen (c). All plots refer to different values of τ : $\tau = 0.001$ (solid line), $\tau = 0.004$ (dotted line), $\tau = 0.0078$ (dashed line), $\tau = 0.012$ (dot-dash line), $\tau = 0.02$ (triple-dot dashed line) and $\tau = 0.03$ (long dashed line).

ity. If we take a realistic value of $v_A \approx 1000 \text{ km s}^{-1}$, for example, this will provide a value of $\tau = (\delta v/v_A)^2 \approx 0.001$, i.e. smaller by one order of magnitude than the value needed for efficient oxygen heating, as we found in our parametric study. Furthermore, for higher frequencies (with period less than 1 s) even smaller wave amplitudes are expected. According to the model proposed by Cranmer and van Ballegoijen (2005) of wave amplitudes in the lower corona, it is found that the normalized velocity fluctuation $\delta v/v_A$ of the Alfvén waves (with period higher than 3 s) is merely ~ 0.01 . This result, which justifies the linear approximation, is found to be in good agreement with observed

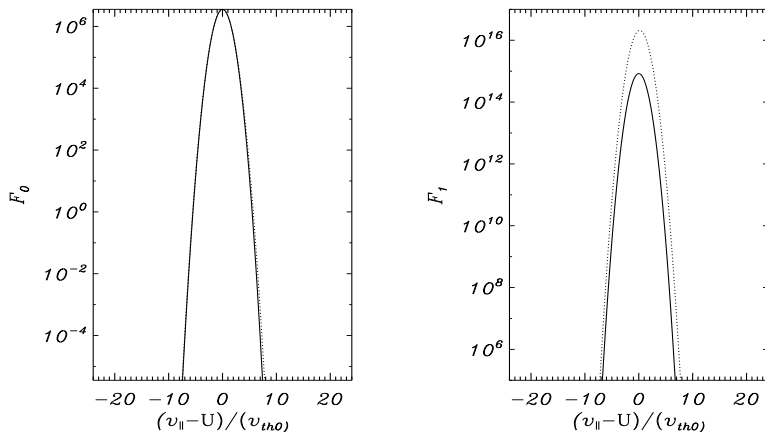


Figure 3.10: The zeroth-order reduced VDFs F_0 (left panel) and first-order reduced VDFs F_1 (right panel) as a function of $v_{||}$ normalized to the initial oxygen thermal speed. The plots are for, $\tau = 0$ (solid line) and $\tau = 0.035$ (dot line).

off-limb nonthermal line widths from SUMER and UVCS (Wilhelm et al. 2007, Kohl et al. 1997).

On the other hand, MHD turbulence can be another possible scenario that may generate low-frequency Alfvén waves (in the range of the frequencies proposed for nonresonant interactions) in the corona. From a pre-existing population of very low-frequency MHD waves (with periods longer than 3 minutes), it is possible to generate small fluctuations by the so-called turbulent cascade mechanism (see, e.g., Cranmer and van Ballegooijen (2003) and references therein) in the corona. The frequency-dependent energy spectrum of these small-scale fluctuations follows a power-law $\propto \omega^{-\eta}$, where η is the spectral index which is found to vary between 1 and 5/3. Thus, the wave amplitudes of those waves having frequencies higher than the observed ones (including waves with periods < 1 s) are expected to be less than the observed normalized velocity fluctuations.

Therefore, in the lower corona, the low-frequency Alfvén waves may not be able to efficiently heat the major ions via nonresonant interactions due to insufficient energy content. Also, we doubt that these waves can efficiently heat protons in the outer corona, since there the plasma beta is higher than in the lower corona. Then, relatively speaking, even more, relatively speaking, wave energy is required for efficient ion heating. However, nonresonant heating could be an important contribution to basal coronal heating, since it can help in overcoming the low initial temperature in the upper chromosphere and transition region. More importantly, it is a mechanism that gives all minor heavy ions the same thermal speed, and especially helps the cold heavy species to attain (without collisional friction) in this way the same gravitational scale height in the lower corona, where otherwise gravity tends to hold back the heavys and thus to produce gravitational

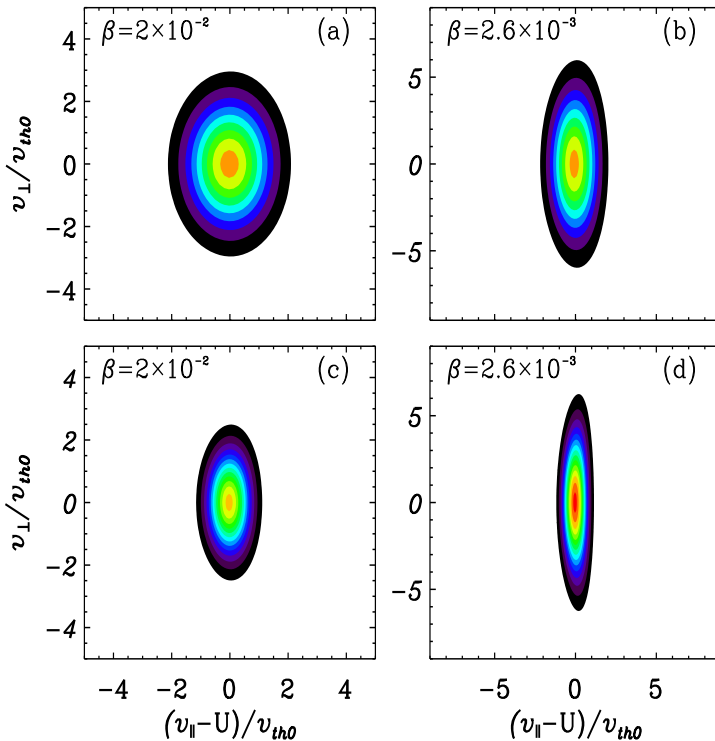


Figure 3.11: (a) and (c): Helium VDFs plotted for different plasma beta values and for $\tau = 0.035$; (b) and (d): Oxygen VDFs plotted for different plasma beta values at $\tau = 0.035$. Here the velocity components are normalized to the initial thermal speed of the helium ions.

settling. Furthermore, we also believe that ion-cyclotron waves which can be generated via several mechanisms, e.g., ion drifts and beams induced by the nonuniform coronal density and magnetic field structure (see, e.g., the recent work of Mecheri and Marsch 2007, 2008), remain the most powerful candidate for preferential ion heating, and the

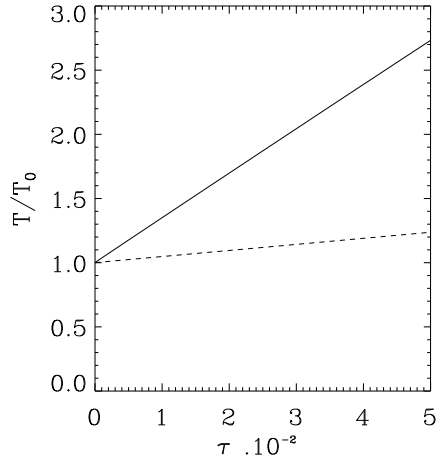


Figure 3.12: Temperature (the same for all three ion species considered) for $\beta = 2.6 \times 10^{-3}$ (continuous line), and $\beta = 2 \times 10^{-2}$ (dashed line) is plotted versus the relative wave energy τ .

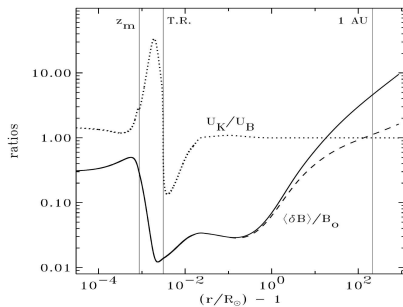


Figure 3.13: Kinetic-to-magnetic energy density ratio (dotted line), dimensionless magnetic amplitude for the undamped linear model (solid line) and for the nonlinearly damped model (dashed line). Cranmer and van Ballegoijen (2005)

likely source of the very high oxygen-ion temperature anisotropy that is observationally inferred to exist in the outer coronal holes.

3.7 Conclusion

In this chapter, we have studied the heating of ions, which can be achieved via nonresonant wave-particle interactions in a low-beta plasma and for large averaged wave amplitudes. Non-dispersive Alfvén waves were assumed to propagate parallel to the field in a homogeneous magnetized plasma, which consists of many ion species. In our treatment, the quasi-linear theory (QLT) for the reduced velocity distribution functions (VDFs) of the ions has been used, and on this basis different diffusion operators and kinetic equations have been derived. As a result, in a strongly magnetized low-beta plasma, the enhanced low-frequency Alfvén waves, with $\omega_k \ll \Omega_p$, can lead to significant perpendicular ion heating. That process yields the same conic-like VDFs as found by Wang et al. (2006) in their test-particle simulations. It was shown that the heavy ions (represented by oxygen ions) are preferentially heated due to their larger inertia, i.e., in proportion to their masses as compared with the protons or helium ions. Thus all ions will acquire the same thermal widths of their distributions, given there is sufficient wave power.

Since heating by low-frequency waves needs a strongly magnetized plasma, this process may happen only in the lower corona, where very constricted flux tubes at the photosphere start to expand strongly above the upper chromosphere. However, at these altitudes the expected values of the average amplitudes of the Alfvén waves is smaller by more than one order of magnitude than the needed values. Even more wave energy may be required to heat the outer corona, and to compensate for the increase in plasma β . In compliance with the solar wind in-situ measurements, the wave energy existing in the outer corona might also not be large enough. However, the low-frequency Alfvén waves can provide a global contribution to coronal heating, especially at lower altitudes, since these waves can be easily generated by an MHD mechanism, and thus rise the heavy ion temperatures, a process leading to the same thermal width for all ion species. Thus nonresonant wave heating may also explain the kinetic feature found by in-situ measurements in solar wind, which is that the heavy ion temperatures are proportional to their masses (von Steiger et al. 1995, Marsch 2006).

4 Coronal loop model including ion kinetics

4.1 Introduction

Coronal plasma loops are often observed as isolated bright flux tubes which are fairly homogeneous along their length. Whereas the loops longitudinally appear to be nearly isothermal, the temperatures and densities of loops are found to vary transversely on small scales between adjacent loops (Aschwanden et al. 1999, 2000a, Lenz et al. 1999, Brković et al. 2002). In 1981, Rosner, Tucker, Vaina, & Serio (RTVS) proposed a hydrostatic loop model including gravity, in which they considered a semi-circle loop with a constant cross section and assumed a constant pressure along the loop with uniform heating. The RTVS model predicts a steep temperature profile that rises from the loop footpoints and increases above the transition to the loop apex. The model was found to be consistent with the high-temperature loops observed with X-ray instruments (e.g., Kano and Tsuneta 1996).

However, under the assumption that the plasma is isothermal along the loop segments, several observations made in the extreme ultraviolet (EUV), e.g. by TRACE and the EUV Imaging Telescope (EIT) on SOHO (Lenz et al. 1999, Schrijver et al. 1999, Aschwanden et al. 2001, Winebarger et al. 2003a) seem to show that the warm EUV coronal loops (with a temperature $T \approx 1 - 1.5$ MK) in active region generally have enhanced densities (yielding bright emission) with enhanced pressure scale heights in comparison to the RTVS model and flat temperature profiles along the entire loop lengths. The properties of these observed EUV coronal loops can therefore not be reconciled with the RTVS model, no more than with the hydrostatic models assuming uniform heating. Aschwanden et al. (2001) have tried to model the observed EUV coronal loops with hydrostatic solutions obtained from the hydrodynamic equations and used a nonuniform heating function (without involving scaling laws). Fitting the hydrostatic solutions to 41 observed EUV loops, only 30% of them were found to be consistent with the results from a model that uses footpoint heating with a small heating scale length (strongly nonuniform), and none of the observed loops were consistent with uniform heating.

Winebarger et al. (2002) and Marsch et al. (2004) detected with SUMER steady flows along EUV loops with line-of-sight speeds of several 10 km s^{-1} . In accord with these observations, we believe that asymmetric heating in the presence of steady flows in loops can give better fits to the observed EUV loops. However, Patsourakos et al. (2004) have concluded that, according to his model, also models with steady flows are unable to explain the properties of the EUV coronal loops. Although such models show density en-

hancements, their temperature profiles appear to be inconsistent with loop observations. In a similar approach considering mass flows in coronal loops, Li and Habbal (2003) and O'Neill and Li (2005) modeled the EUV loops and proposed a heating mechanism that is based on heating by dissipation of turbulence-driven Alfvén waves within a two-fluid dynamic model. The studied loops have lengths ranging from 10 Mm to 600 Mm. It is assumed that Alfvén waves originate below the transition region, enter the loop from one footpoint and further up lead to proton heating. Due to heat exchange and conduction the electrons are also heated. Recently, Petrie (2006) further studied the influence of steady flows on the scale heights in expanding flux tubes of stratified loops and deduced that, when the tube cross-sectional area increases sufficiently with altitude, the scale height could be enhanced by steady flows.

On the other hand it has been shown that the plasma of the solar corona is usually far from local thermal equilibrium (see, e.g., Kohl et al. 1998); Wilhelm et al. (1998), Frazin et al. (2003). Furthermore, evidence that the local O^{5+} velocity distribution is anisotropic has been found (see, e.g., Telloni et al. 2007). These observations have been explained by the ion-cyclotron heating mechanism that may lead to preferential heating and acceleration of heavy ions within a kinetic model (Vocks and Marsch 2001, Vocks 2002), and to heating and acceleration of protons in terms of a fluid model for the magnetic funnels of coronal holes (Marsch and Tu 1997, Tu and Marsch 1997).

In this chapter we present a semi-kinetic model for coronal loop heating, and we study the signatures and effects of cyclotron waves in the heating of coronal loops. Collisions also have to be accounted for as they still are relatively efficient in comparison with the outer corona and solar wind. The here proposed kinetic model includes the effects the magnetic field has through the gyrofrequency on the dynamics and heating of the coronal loop, and it is therefore possible to study and understand the connections between the plasma kinetics and the magnetic structure of the loop confining the plasma. Fortunately, as was already mentioned, a lot of observations have been made of a variety of EUV and X-ray coronal loops, and their plasma parameter profiles have been inferred. But much less theoretical work on, or accurate observation of, the magnetic-field structure of coronal loops has been done. Yet, that is important for a better understanding of possible wave heating mechanisms.

The Chapter is organized as follows: in Sec. 4.2 we give a description of the model including the coronal loop geometry. Then in Sec. 4.3 we present the numerical methods used in the code. The numerical results will be given in Sec. 4.4, and finally in Sec. 4.5 we discuss the physical results and give some perspectives.

4.2 The model description

4.2.1 Coronal loop geometry

Before studying the coronal loop plasma model, we start with the geometry or rather the magnetic field structure that confines the plasma of the coronal loop. Here we neglect the back-reaction of the plasma on the coronal loop structure of the magnetic field. This is understandable since the magnetic pressure is assumed to strongly dominate the plasma pressure.

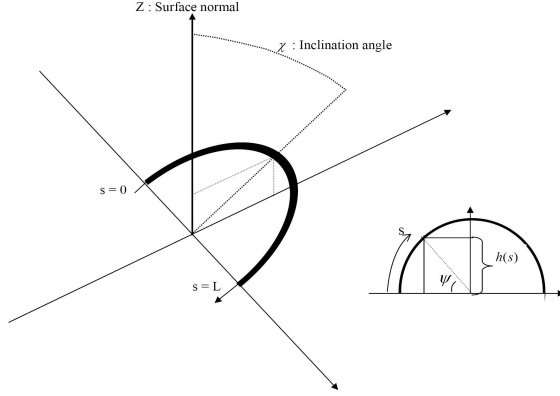


Figure 4.1: The geometry used for the inclination, χ , and the arc angle ψ . These angles are used to determine the gravity given by eq. (4.4).

The loop geometry is considered to be that of a semi-circular cylindric and symmetric flux tube. The footpoints of the loop are assumed to be emerging in the transition region, i.e., the height of the footpoints from solar surface is around ~ 2 Mm, where L is the loop length, and $s = 0$ refers to the left footpoint and $s = L$ to the right one. L/π is the altitude of the loop top relative to the footpoints. The tube that determines the bundle of magnetic field lines has a symmetrically expanding cross-section area from the footpoints to the loop apex located at ($s = L/2$). The variation of the normalized cross section, shown in Fig. 4.2, is suggested to obey the following formula:

$$\frac{A(s)}{A_0} = \left[\frac{1}{\Gamma^2} + \left(1 - \frac{1}{\Gamma^2} \right) \left(\frac{2s}{L} - 1 \right)^2 \right]^{-1}, \quad (4.1)$$

where $\Gamma = \sqrt{A_1/A_0} = w_1/w_0$ is the parameter of homogeneity or the expansion factor, with A_1 and w_1 being the cross section and the width at the loop top and A_0 , w_0 at its footpoint. This means that if $\Gamma = 1$, then the tube is homogeneous.

The magnetic flux is assumed to be conserved which means $A(s).B(s) = A_0.B_0$ (B_0 is the magnitude of the magnetic field at $s = 0$), thus the variation of the magnetic field along the loop is

$$\frac{B(s)}{B_0} = \left[\frac{1}{\Gamma^2} + \left(1 - \frac{1}{\Gamma^2} \right) \left(\frac{2s}{L} - 1 \right)^2 \right]. \quad (4.2)$$

Then, the situation when $\chi = 0$ implies that the plane of the loop is perpendicular to the solar surface. In this case, the gravity forces along the loop have their maximal influence on the dynamics of coronal loop ions.

4.2.2 Theory

The model is based on the Vlasov equation for the reduced velocity distribution function's (VDFs) as described in the papers of Vocks and Marsch (2001) and Vocks and Marsch (2002), where an open-field structure was considered. Here we apply this model to a closed coronal loop. The basic equation is the reduced Vlasov equation which describes the evolution in space and time of the gyrotropic reduced VDF $F_k(s, t, v_{\parallel})$. This kinetic equation reads:

$$\begin{aligned} & \frac{\partial F_k}{\partial t} + v_{\parallel} \frac{\partial F_k}{\partial s} + \left(\frac{q}{m} E_{\parallel} - g \cos \psi \right) \frac{\partial F_k}{\partial v_{\parallel}} + \frac{1}{2A} \frac{\partial A}{\partial s} \left(\frac{\partial F_{k+1}}{\partial v_{\parallel}} + 2v_{\parallel}(k+1)F_k \right) \\ & = \left(\frac{\delta F_k}{\delta t} \right)_{w-p} + \left(\frac{\delta F_k}{\delta t} \right)_{coul}, \end{aligned} \quad (4.3)$$

where $A(s)$ is the area function of the flux/flow tube, q and m are the charge and mass of the particle, E_{\parallel} is the parallel electric field, g the solar gravitational acceleration given later by eq. (4.4), ψ the angle of inclination of the magnetic field with respect to the direction normal to the solar surface. The reduced VDFs depend only upon one velocity v_{\parallel} and one spatial coordinate s along the mean magnetic field, and v_{\parallel} and v_{\perp} are the parallel and perpendicular velocity components. The right-hand side of (4.3) are the wave-particle interaction and Coulomb collision operators defined below. The k th-order reduced VDF is given by eq. (2.27). Here, we will only deal with the first two moments, where a closure relation is introduced to avoid the higher orders in k .

From the first two reduced velocity distribution functions, F_0 and F_1 , it is possible to obtain all relevant plasma parameters. For example, by integration of F_0 over various powers of v_{\parallel} we get the particle density N , drift velocity U , parallel temperature T_{\parallel} , and heat flux q_{\parallel} . Considering also the moments of F_1 , the perpendicular temperature T_{\perp} and heat flux vector component q_{\perp} can be obtained.

The gravity acceleration g showing up in eq. (4.3) can be written, in case of inclined loop, as follows:

$$g(s) = \frac{GM_{\text{Sun}}}{[R_{\text{S}} + h(s) \cos \chi]^2} \cos \chi, \quad (4.4)$$

where the length h is shown in Fig. 4.1, G is the constant of gravity. M_{S} , R_{Sun} are, respectively, the mass and the radius of the sun. It should be noted that there is an extra $\cos \chi$ term in eq. (4.4) that decreases the gravity effect on the ion dynamics in case of inclined loops.

In our model we treat the electrons as a fluid in hydrostatic equilibrium and neglect their inertia, and thus the electric field E_{\parallel} arising from charge separation is determined from the electron momentum equation and quasi-neutrality ($N_e \approx \sum_j q_j N_j$) as follows:

$$-eE_{\parallel} = \frac{1}{N_e} \frac{\partial}{\partial s} (k_{\text{B}} T_e N_e), \quad (4.5)$$

where q_j and N_j are the charge and number density of ion species j , e and N_e are the elementary charge unit and electron number density, and k_{B} is the Boltzmann constant. Here T_e is the electron temperature which can be obtained in electron-ions plasma through

the following energy equation

$$\frac{\partial T_e}{\partial t} = \frac{2}{3N_e k_B A} \frac{\partial}{\partial s} (A \kappa_e \frac{\partial T_e}{\partial s}) + 2 \sum_i v_{ie} (T_i - T_e) - \frac{2}{3N_e k_B} L_{rad}, \quad (4.6)$$

where κ_e is the electron heat conductivity which is expressed in terms of electron collision period, τ_e , as follows:

$$\kappa_e = 3.2 \frac{N_e k_B T_e}{m_e} \tau_e, \quad (4.7)$$

$$\tau_e = 3.44 \times 10^5 \frac{T_e^{3/2}}{N_e \lambda} (\text{sec}). \quad (4.8)$$

Thus, we use $\kappa_e = 1.2 \times 10^{-7} T_e^{5/2}$ (in cgs units) when the Coulomb logarithm $\lambda \approx 19$. v_{ie} is the ion-electron collision frequency given by Braginski (1965),

$$v_{ie} = \frac{16\pi N_e e_i^2 e^2 \lambda}{3 m_i m_e} \left(\frac{2k_B T_e}{m_e} \right)^{-\frac{3}{2}}, \quad (4.9)$$

where m_i (m_e) is ion mass (electron mass). e and e_i , respectively are the electron and ion charges. L_{rad} is the radiative energy loss function as calculated by Rosner et al. (1978), which can be written in $\text{erg cm}^{-3} \text{ s}^{-1}$ units as

$$L_{rad} = -\frac{N_e^2}{4} P(T), \quad (4.10)$$

where $P(T)$ is a function which can be approximated by a sequence of power laws as follows:

$$\begin{aligned} P(T) &\approx 10^{-21.85}, & 10^{4.3} < T < 10^{4.6} K, \\ &\approx 10^{-31} T^2, & 10^{4.6} < T < 10^{4.9} K \\ &\approx 10^{-21.2}, & 10^{4.9} < T < 10^{5.4} K, \\ &\approx 10^{-10.4} T^{-2}, & 10^{5.4} < T < 10^{5.75} K \\ &\approx 10^{-21.94}, & 10^{5.75} < T < 10^{6.3} K \\ &\approx 10^{-17.73}, & T^{-2/3} 10^{6.3} < T < 10^7 K. \end{aligned} \quad (4.11)$$

The wave-particle interaction is treated self-consistently by considering the evolution of the wave spectral energy density for waves entering from the left footpoint of the loop, $\mathfrak{B}_\omega^{Lf}(t, s)$, and from the right side, $\mathfrak{B}_\omega^{Rf}(t, s)$, that are described by the following equations:

$$\frac{\partial \mathfrak{B}_\omega^{Lf}}{\partial t} + \frac{1}{A} \frac{\partial}{\partial s} (|A v_{ph}| \mathfrak{B}_\omega^{Lf}) + \mathfrak{B}_\omega^{Lf} \frac{1}{2A} (A U_m) = \left(\frac{\delta \mathfrak{B}_\omega^{Lf}}{\delta t} \right)_{w-p}, \quad (4.12)$$

$$\frac{\partial \mathfrak{B}_\omega^{Rf}}{\partial t} - \frac{1}{A} \frac{\partial}{\partial s} (|A v_{ph}| \mathfrak{B}_\omega^{Rf}) + \mathfrak{B}_\omega^{Rf} \frac{1}{2A} (A U_m) = \left(\frac{\delta \mathfrak{B}_\omega^{Rf}}{\delta t} \right)_{w-p}, \quad (4.13)$$

where U_m is the plasma's center-of-mass velocity, and the symbol $v_{ph} = \frac{\omega}{k}$ denotes the phase velocity. The term on the right-hand side of the equations (4.12) and (4.13) upon

integration ensures energy conservation between waves and particles in the form:

$$\begin{aligned}
 & - \int \left(\frac{\delta \mathfrak{B}_\omega^{Lf}}{\delta t} \right)_{w-p} d\omega - \int \left(\frac{\delta \mathfrak{B}_\omega^{Rf}}{\delta t} \right)_{w-p} d\omega \\
 = & \sum_j \frac{m_j}{2} \int d v_\parallel \left[v_\parallel^2 \left(\frac{\delta F_{j,0}}{\delta t} \right)_{w-p} + \left(\frac{\delta F_{j,1}}{\delta t} \right)_{w-p} \right]. \quad (4.14)
 \end{aligned}$$

The wave-particle interactions are evaluated within the framework of quasilinear theory for cyclotron resonance (Marsch, 1998). For simplicity we disregard the wave dispersion and here merely consider nondispersive Alfvén waves, an assumption which will be discussed and justified in the next section. Then, the kinetic particle equations including resonant wave-particle effects can be written as:

$$\left(\frac{\delta F_{j,0}}{\delta t} \right)_{w-p} = \frac{\partial}{\partial v_\parallel} (D_j(v_\parallel) \frac{\delta F_{j,1}}{\partial v_\parallel}) - \frac{\partial}{\partial v_\parallel} (A_j^+(v_\parallel) F_{j,0}), \quad (4.15)$$

$$\begin{aligned}
 \left(\frac{\delta F_{j,1}}{\delta t} \right)_{w-p} &= \frac{\partial}{\partial v_\parallel} (D_j(v_\parallel) \frac{\delta F_{j,2}}{\partial v_\parallel}) - 2 \frac{\partial}{\partial v_\parallel} (A_j^+(v_\parallel) F_{j,1}) \\
 &+ A_j^-(v_\parallel) \frac{\delta F_{j,1}}{\partial v_\parallel} - H_j(v_\parallel) F_{j,0}, \quad (4.16)
 \end{aligned}$$

where D_j , A_j^\pm and H_j respectively are the diffusion, acceleration and heating coefficients:

$$D_j = \frac{\pi \mu_0}{2B^2} \Omega_j \left(\frac{|v_{ph}|}{|v_{ph}| - v_\parallel} \mathfrak{B}_{\omega = \frac{|v_{ph}|\Omega_j}{|v_{ph}| - v_\parallel}}^{Lf} + \frac{|Av_{ph}|}{|v_{ph}| + v_\parallel} \mathfrak{B}_{\omega = \frac{|v_{ph}|\Omega_j}{|v_{ph}| + v_\parallel}}^{Rf} \right), \quad (4.17)$$

$$\begin{aligned}
 A_j^\pm &= \pm (|v_{ph}| - v_\parallel) \frac{\pi \mu_0}{B^2} \Omega_j \frac{|v_{ph}|}{|v_{ph}| - v_\parallel} \mathfrak{B}_{\omega = \frac{|v_{ph}|\Omega_j}{|v_{ph}| - v_\parallel}}^{Lf} \\
 &\mp (|v_{ph}| + v_\parallel) \frac{\pi \mu_0}{B^2} \Omega_j \frac{|v_{ph}|}{|v_{ph}| + v_\parallel} \mathfrak{B}_{\omega = \frac{|v_{ph}|\Omega_j}{|v_{ph}| + v_\parallel}}^{Rf}, \quad (4.18)
 \end{aligned}$$

$$\begin{aligned}
 H_j &= -2(|v_{ph}| - v_\parallel)^2 \frac{\pi \mu_0}{B^2} \Omega_j \frac{|v_{ph}|}{|v_{ph}| - v_\parallel} \mathfrak{B}_{\omega = \frac{|v_{ph}|\Omega_j}{|v_{ph}| - v_\parallel}}^{Lf} \\
 &+ 2(|v_{ph}| + v_\parallel)^2 \frac{\pi \mu_0}{B^2} \Omega_j \frac{|v_{ph}|}{|v_{ph}| + v_\parallel} \mathfrak{B}_{\omega = \frac{|v_{ph}|\Omega_j}{|v_{ph}| + v_\parallel}}^{Rf}. \quad (4.19)
 \end{aligned}$$

Here μ_0 is the free-space permeability, and B the magnetic field magnitude. The gyrofrequency of species j is defined as $\Omega_j = q_j B / m_j$. In the expressions given above only the left-hand polarization part is considered for both forward and backward propagating waves having the spectrum \mathfrak{B}^{Lf} or \mathfrak{B}^{Rf} .

The initial model spectra are assumed to vary inversely with the wave frequency. The Coulomb collision term on the right side of (4.3) has in detail been calculated and evaluated within the approximation of reduced VDFs by Vocks (2002) using the full Focker-Planck operator. Notice that also ion-electron collisions have entirely been included in the Coulomb collision term, but they are small in comparison with the ion-ion collisions owing to the smallness of the mass ratio (m_e/m_p). The role of collisions is significant,

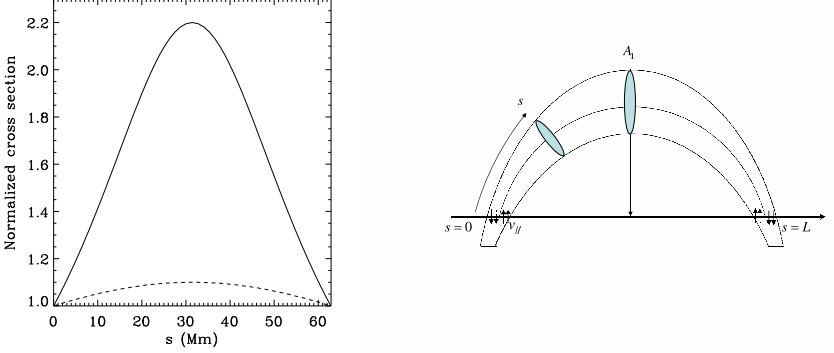


Figure 4.2: Variation of the normalized cross section relative to the footpoint cross section, for $\Gamma = 1.48$ (line) and $\Gamma = 1.04$ (dashed line), shown versus distance along the loop.

and they suffice to enforce local isotropy which can be maintained in an electron-proton plasma loop as we will see in the next section.

4.3 Numerical method

Here, we deal with a system of partial differential equations (4.3), (4.6), (4.12), (4.13) and (4.14) which have to be solved self-consistently at each time step. The reduced VDFs F_0 and F_1 depend on position s_i , velocity coordinate $v_{||,m}$ and time t_j . Fig. 4.3 shows the simulation domain that represent the coronal loop in one spatial dimension in which the velocity coordinates are represented in the perpendicular axis. To obtain the updated functions F_0 and F_1 a finite difference scheme method is used.

The coordinates s and $v_{||}$ are discretized non-equidistantly as sketched in Fig. 4.3. The left and the right bounds are, respectively, located in the left and right footpoint of the loop which are embedded in the relatively cool and dense upper chromosphere. The discretization in space, $\Delta s_i = s_{i+1} - s_i$, and the velocity $\Delta v_{||,m} = v_{||,m+1} - v_{||,m}$ are not equidistant, and the space shells are chosen to be smallest close to those boundaries, while the velocity shells are chosen to be proportional to the absolute value of $v_{||,m}$.

The determination of the space grid points on the space axis, (see Fig. 4.3), is based on the values (N_0, a_s) , where N_0 is the number of the grid space for one half of the loop (with half length, $\frac{L}{2}$), and $a_s = \Delta s_i / \Delta s_{i-1}$ is the factor of the space proportionality. Then, the space shell thickness Δs_0 can easily be obtained from the sum of a geometrical series with a constant factor $a_s \neq 1$ as follows;

$$\Delta s_0 = \frac{L}{2} \frac{1 - a_s}{1 - a_s^{N_0+1}} \quad (4.20)$$

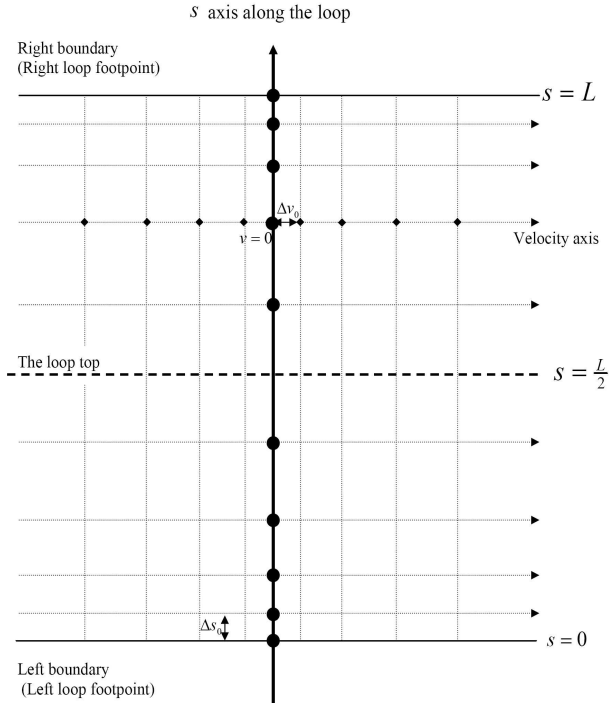


Figure 4.3: Sketch of the simulation box that represents the modeled coronal loop.

The determination of the velocity grid points on the velocity axis (see Fig.4.3) for plasma species j is based on the choice of the factor of the proportionality, $a_v = v_{||,m+1}/v_{||,m}$, and the parameter α such that

$$\Delta v_{||,0} = \alpha v_{th0}, \quad (4.21)$$

where v_{th0} is the initial thermal speed of the species j given at position $s = 0$.

The non-equidistance space discretization is adopted for the reasons of stability in numerical solutions and to guarantee the convergence of the solutions of the wave-energy equations (4.12), (4.13). The stable solutions can be achieved when the Courant–Friedrichs–Lewy (CFL) condition, $|v_{ph}\Delta t/\Delta s| < 1$ is satisfied. In our model, as we will see in the next section, the phase speed, v_{ph} , increases as much as we move toward the loop top due to the decrease in electron density. Thus, an increasing extent of the space shells towards the loop top, $\Delta s > \Delta s_{i-1}$, guarantee more stability in the numerical solutions.

To solve eq. (4.3) we used the same numerical routines used before in Vocks's code which has been developed for a coronal funnel (see Vocks). In the following we summa-

rize the numerical methods used to solve eq. (4.3): First, equation (4.3) has been divided into three main terms, wave-particle term, Coulomb collision term and the advection term. The spatial derivatives, $\partial F_k / \partial s$, which only show up in the advection term, are discretized using central differences method with first order correction in the upwind direction for a non-equidistance grid space;

$$\frac{\partial F_k}{\partial s}(s - v\Delta t) = \frac{\partial F_k}{\partial s} \Big|_1 - v\Delta t \frac{\partial^2 F_k}{\partial s^2} \Big|_2. \quad (4.22)$$

To compute the first and the second spatial derivatives with subscript 1 and 2, a quadratic interpolation approximation has been used at the three points, s_{i-1} , s_i and s_{i+1} , such that

$$f(s) = a(s - s_i)^2 + b(s - s_i) + c, \quad (4.23)$$

with the coefficients a and b being given by

$$a = \frac{\Delta s_{i-1} f_{i+1} + \Delta s_i f_{i-1} - f_i(\Delta s_{i-1} - \Delta s_i)}{\Delta s_{i-1} \Delta s_i (\Delta s_{i-1} + \Delta s_i)}, \quad (4.24)$$

$$b = \frac{(\Delta s_i^2 - \Delta s_{i-1}^2) f_i + \Delta s_{i-1}^2 f_{i+1} - \Delta s_i^2 f_{i-1}}{\Delta s_{i-1} \Delta s_i (\Delta s_{i-1} + \Delta s_i)}, \quad (4.25)$$

where $f_{i-1} = f(s_{i-1})$, $f_i = f(s_i)$ and $f_{i+1} = f(s_{i+1})$, which are needed to compute the first and the second spatial derivative of $F_k(s)$ as:

$$\frac{\partial F_k}{\partial s} \Big|_{1, s=s_i} = b, \quad (4.26)$$

$$\frac{\partial^2 F_k}{\partial s^2} \Big|_{2, s=s_i} = 2a. \quad (4.27)$$

The same technique of the quadratic interpolation given in eqs. (4.23), (4.24) and (4.25) has been used at velocity points v_{m-1} , v_m and v_{m+1} to compute the first and the second velocity derivative of F_k in the advection term and wave-particle interaction term. On the right-hand side of eq. (4.3), the wave-particle interaction term is evaluated using an explicit scheme in time, i.e.,

$$F_k(t + \Delta t) = F_k(t) + \Delta t \frac{\partial F_k(t + \Delta t)}{\partial t}, \quad (4.28)$$

while an implicit method with $F_k(t + \Delta t)$ is considered for the Coulomb collision operator:

$$F_k(t + \Delta t) = F_k(t) + \Delta t \frac{\partial F_k(t)}{\partial t}. \quad (4.29)$$

Now, to we come the explanation of the numerical method used to compute the equation of the electron thermal energy (4.6). Unlike in case of outer corona, the thermal energy of electrons in case of coronal loops (which characterize the main structure of low corona) cannot be neglected due to the enhanced electron density that leads to the energy exchange between ion and electron plasma species. Consequently, thermal energy can be transferred to the electrons, and thus they can be heated.

The electron thermal energy (4.6) has to be solved self-consistently with the rest of the PDE system (4.3), (4.12-4.14). An implicit-scheme method has been employed for the diffusion term of equation (4.8) (term that contains the second spatial derivative), and an explicit-scheme for its rest terms, i.e.,

$$\begin{aligned} \frac{\Delta T(s_i, t_j)}{\Delta t_j} &= \frac{2}{3N_e k_B A(s_i)} \frac{\partial}{\partial s_i} \left(A(s_i) \kappa_e(s_i, t_j + \Delta t) \frac{\partial T_e(s_i, t_j + \Delta t)}{\partial s_i} \right) \\ &+ 2 \sum_i v_{ie}(s_i, t_j) (T_i(s_i, t_j) - T_e(s_i, t_j)) \\ &- \frac{2}{3N_e k_B} L_{rad}(s_i, t_j), \end{aligned} \quad (4.30)$$

where t_j and s_i are the time and space grid points, and $\Delta T(s_i, t_j)$ is the update in electron temperature at $t_j + \Delta t$ (Δt is the time step), i.e.,

$$T_e(s_i, t_j + \Delta t) = T_e(s_i, t_j) + \Delta T(s_i, t_j). \quad (4.31)$$

To calculate the first and the second spatial derivative of the electron temperature T_e , and also the first derivative of $\ln A$ (the cross section), we used the first-order and second-order central differences for non-equidistance schemes as showed in eqs. (4.23-4.27).

Finally, by making use of the spatial derivatives of $\ln A$ and T_e in eq. (4.30), we obtain the following algebraic system of nonlinear equations

$$a_i(T, \Delta T) \Delta T_{i-1,j} + b_i(T, \Delta T) \Delta T_{i,j} + c_i(T, \Delta T) \Delta T_{i+1,j} = X_i, \quad i = 1, \dots, N-1 \quad (4.32)$$

where N is the number of space grid points, and $\Delta T_{i,j}$ denotes the variation in electron temperature at initial time t_j and at position s_i . The coefficients a_i , b_i , c_i and X_i can derived from (4.30).

Since we are dealing with a system with fixed values at the boundaries (i.e., $\Delta T_{e,R,j} = \Delta T_{e,L,j} = 0$), two nonlinear equations at the right and left boundary have to be added to the system of equation (4.32)

$$b_0 \Delta T_{1,j} + c \Delta T_{2,j} = X_0, \quad \text{for } i = 0 \quad (4.33)$$

$$a_N \Delta T_{N-1,j} + b_N \Delta T_{N,j} = X_N, \quad \text{for } i = N. \quad (4.34)$$

Thus, the nonlinear system of equations (4.32-4.34) can be solved by using the successive overrelaxation method (SOR) to determine the vector ΔT at each time step ΔT .

On the other hand, in our coronal loop model we considered the contribution of waves that can propagate in the opposite (or backward) direction which are described by the wave-energy equation (4.13). We solved the wave-energy equation for forward propagating waves (4.12) and backward propagating waves (4.13) self-consistently using an implicit scheme, respectively, with upwind and downwind differences method, depending on the direction of wave propagation. Then, in the case of waves propagating in the

opposite direction ($k < 0$), the implicit scheme in time is adopted as follows:

$$\frac{\partial \mathfrak{B}_\omega^{Rf}(s_i, t_j)}{\partial t} = \frac{1}{A} \frac{\partial}{\partial s} (A |v_{ph}| \mathfrak{B}_\omega^{Rf}(s_i, t_{j+1})) - \mathfrak{B}_\omega^{Rf}(s_i, t_{j+1}) \frac{1}{2A} (AU_m), \quad (4.35)$$

whereby the the first derivative of any quantity in the advection term of this equation is calculated using simple downwind difference method,

$$\frac{\partial f_i}{\partial s_i} = \frac{f_{i+1} - f_i}{\Delta s_i}. \quad (4.36)$$

When we implement this derivative method also a system of linear equations is obtained

$$\alpha_i \Delta \mathfrak{B}_\omega^{Rf}{}_{,i,j} + \beta_i \Delta \mathfrak{B}_\omega^{Rf}{}_{,i+1,j} = \Pi_i, \quad i = 0, \dots, N, \quad (4.37)$$

where $\Delta \mathfrak{B}_\omega^{Rf}{}_{,i,j}$ is the variation in \mathfrak{B}_ω^{Rf} at position s_i , and the coefficients α_i, β_i and Π_i are given at time t_i by the expressions:

$$\alpha_i = 1 + \Delta t \left(\frac{v_{ph}}{\Delta s_i} + 0.5 \left(\frac{\partial v_{ph}}{\partial s} \Big|_{s=s_i} \frac{\partial \ln A}{\partial A} \Big|_{s=s_i} \right) \right), \quad (4.38)$$

$$\beta_i = -1 + \Delta t \frac{v_{ph}}{\Delta s_i}, \quad (4.39)$$

$$\Pi_i = \Delta t \left(\frac{\partial (A v_{ph} \mathfrak{B}_\omega^{Rf})}{\partial s} \Big|_{s=s_i} - 0.5 (A \mathfrak{B}_\omega^{Rf}) \left(\frac{\partial U}{\partial s} \Big|_{s=s_i} + U \frac{\partial \ln A}{\partial A} \Big|_{s=s_i} \right) \right). \quad (4.40)$$

At the left boundary (s_{N+1}) of our simulation box a source of wave energy is assumed. The waves are generated with no time dependence. This means $\Delta \mathfrak{B}_{\omega, N+1, j} = 0$, and then from eq.(4.42) $\Delta \mathfrak{B}_{\omega, N, j}^{Rf}$ can be obtained as

$$\Delta \mathfrak{B}_{\omega, N, j}^{Rf} = \frac{\Pi_N}{\alpha_N}, \quad (4.41)$$

and thus $\Delta \mathfrak{B}_{\omega, i, j}^{Rf}$ for $i = 0, \dots, N-1$ can be extracted.

Also, at each time step the energy gained by particles is well guaranteed to be the same as the energy lost by the waves in order to maintain total energy conservation as given in eq. (4.14).

4.4 Simulation results

4.4.1 General remarks

In our model the energy source for heating is assumed to be associated with dissipation of non-dispersive Alfvén waves via ion-cyclotron resonance. These high-frequency waves may be released from small-scale reconnection leading to microflare-like events occurring in the chromospheric network see (e.g., Axford et al. 1999). Then, they enter the simulation box from the footpoints with a power-law spectrum density $\propto \omega^{-1}$, and fall in

left-hand resonance with the ions of species j obeying the condition, $\omega - k_{\parallel} v_{\parallel j} - \Omega_j = 0$, with the parallel wavevector k_{\parallel} . The ion-cyclotron heating mechanism is intimately connected with the magnetic field structure. For a low plasma β value, only those Alfvén waves with frequencies close to the gyrofrequency of any ion species can become resonant, and then effectively exchange energy with the particles.

The loop geometry, which defines the magnetic field structure, plays an important role in coronal loop heating and determines whether the heating is uniform or non-uniform. According to Watko and Klimchuk (2000), most of the observed loops are not significantly thicker in their middles than at their footpoints. In fact, since an accurate 3d-reconstruction of coronal loops has still not been achieved, studying various heating mechanisms is very interesting, and thus it is quite relevant to study the specific signatures of the ion-cyclotron heating mechanism in coronal loops. In this work, we propose a loop geometry as described in the previous section, whereby the parameter of homogeneity, Γ that determines the thickness in the middle of the loop, will be chosen to have the values 1.04 and 1.48.

In the simulations we shall consider protons as single ionic species (together with electrons) in the plasma of the loop, and for the boundaries we assume that the footpoints are emerging in the transition region. Then the boundary values of the density and temperature can be taken as: $N_0 = 5 \times 10^{15} \text{ m}^{-3}$, and $T_0 = 2 \times 10^5 \text{ K}$. The magnetic field at $s = 0$ is $B_0 = 80 \text{ G}$, which yields for the gyrofrequency at the footpoints $\Omega_0 = 76.65 \times 10^4 \text{ Hz}$. The initial conditions are chosen to be constants, i.e. we have $T(s) = T_0$ and $N(s) = N_0$. At $t = 0$ the waves start to propagate close to the footpoints with a power-law spectrum density $\mathfrak{B}_\omega \approx 2.8 \times 10^{-4} [\omega \log(\Gamma^2)]^{-1} \text{ J m}^{-3} \text{ s}$. In order to achieve coronal temperatures in the loop, the required total wave energy flux has to be about $F_0 \approx 7 \times 10^2 \text{ J m}^{-2} \text{ s}^{-1}$ which can be obtained through the integration of $v_{ph} \mathfrak{B}_\omega$ over the frequency interval from (Ω_0/Γ^2) to Ω_0 . In such a way the loop can, in the final steady state reach a temperature of $T \gtrsim 10^6 \text{ K}$. The value of our model power-law spectrum density was computed in compliance with the energy flux of the observed oscillations in the chromosphere which roughly range between 3×10^{-3} and 0.1 Hz . Within this domain the wave energy flux is about $3 \times 10^3 \text{ J m}^{-2} \text{ s}^{-1}$. This value seems reasonable if we compare it with the wave energy flux (ranging between 10^3 and $10^4 \text{ J m}^{-2} \text{ s}^{-1}$) inferred from the observed chromospheric magnetic and velocity fluctuations (Ulrich (1996)), and the recently the detected Alfvén waves in the corona (Tomczyk et al. (2007)). Still our knowledge about the origin and the properties of the coronal Alfvén waves is not clear (see, e.g. Klimchuk's review (2006)). If the Alfvén waves enter only from one side of the loop, an asymmetric heating occurs, and consequently a quasi-static loop with subsonic mass flow ($v \ll c_s$) can be achieved (here c_s is the local sound speed). In addition, symmetric heating with static solutions is possible if we have Alfvén waves entering from either footpoints with the same energy density so that they heat the loop plasma simultaneously from both legs. In the relaxed final steady state the plasma loop has completely forgotten its initial conditions.

4.4.2 Asymmetric heating

Here we consider the situation that Alfvén waves enter the loop only from the left boundary with ($\mathfrak{B}_\omega^{Rf} = 0$). It is thus possible to heat the protons by wave absorption, through which the wave energy can be transferred to the protons selfconsistently, a process de-

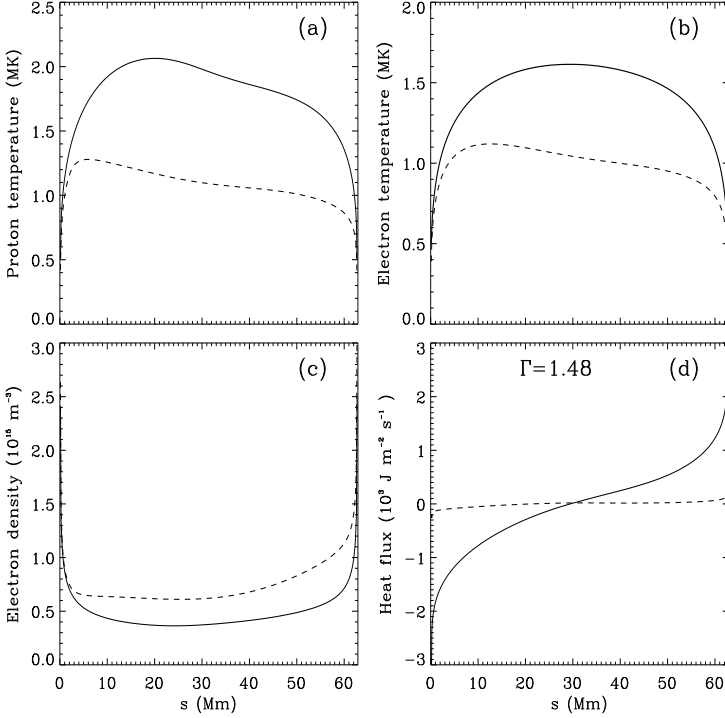


Figure 4.4: The proton temperature (upper left panel), electron temperature (upper right), and density (lower left) for $\Gamma = 1.48$ (line) and $\Gamma = 1.04$ (dashed line) versus distance along the loop; the heat flux conduction (lower right panel) for electron (line) and proton (dashed) versus distance distance along the loop.

scribed by the transport equation of the wave spectrum (6) and (7). As a result asymmetric heating will occur. In Fig. 4.4, the steady profiles of the plasma density and temperature along the loop are given for the different values of the parameters Γ . For $\Gamma = 1.48$, where the cross section of the magnetic flux tube expands more than twice from its footpoints to the middle of the loop, we find that the proton temperature rises smoothly from a minimum at the left boundary at $s = 0$ towards a maximum which is around $\sim 2 \times 10^6$ K at $s \approx 20$ Mm. Then it again decreases to a minimum at the right boundary at $s = L$.

The density profile has the inverse behaviour to the proton temperature, i.e. the density decreases toward its minimum value of $\sim 4 \times 10^{14} \text{m}^{-3}$ at the same position where the proton temperature is at a maximum, and increases afterwards to its boundary value at the right footpoint. Therefore, from these density and temperature profiles it turns out that the loop reveals a quasi-uniform heating in its left leg. This means that the waves entering the simulation box from the left slowly dissipate and heat the protons at different positions in the left leg of the loop. In the case of $\Gamma = 1.04$, however, when the loop is quasi-homogeneous, it is overdense in comparison to a loop having a more expanding cross section. The proton temperature rapidly increases close to the left footpoint and reaches a maximum ~ 1.3 MK at position $s \approx 4$ Mm. Then it weakly decreases and becomes nearly constant in a large part of the loop. This small decrease in temperature is due to ion-electron collisions which can slightly affect the proton temperature in the plasma loop if there is no local wave absorption.

The corresponding electron temperature in steady state and for the different values of the Γ parameter is plotted in Fig. 4.4b. By comparison with the protons, the electrons are cooler for reasons of relatively high radiative losses and strong heat conduction (see Fig. 4.4d), which is more than $\sim 10^2$ times higher than proton heat conduction. All these factors tend to reduce the electron thermal energy gained from proton-electron collisional heat exchange. When $\Gamma = 1.04$, the electron temperature keeps a nearly constant value around $T_e \approx 1$ MK. This flat electron temperature profile seems to be consistent with the observed profiles in most loops showing EUV emission. The rough constancy of the electron temperature is a consequence of thermal diffusion associated with electron heat conduction, working even when the temperature is less than 1 MK.

On the other hand, if the cross section area of the loop is larger on the loop top than at its footpoints (with $\Gamma = 1.48$), then the electron temperature cannot remain constant along the loop but turns out to be much higher because of the temperature difference between electrons and protons, which due to wave heating are much hotter. Thus the electron heating profile in loops with $\Gamma = 1.48$ is more symmetric. This is expected since electron heat conduction, as κ is proportional to $T_e^{5/2}$, is the more efficient the higher the electron temperature is, and consequently hotter electrons can distribute their thermal energy more uniformly along the loop.

It turns out that the nearly isothermal loops in this model are the consequence of a quasi-homogeneous cross section of the magnetic field structure along the loop, in which the waves dissipate faster close to left boundary. Therefore the loop shows footpoint heating which leads to a rapid temperature increase with height, and then no further local heating, and thus the coronal part of the loop becomes nearly isothermal.

In fact, the heating mechanism can, via wave absorption and its connection to the cross section variation, be well explained from Fig. 4.5 which displays the wave spectral energy density of the Alfvén waves in the ion-cyclotron range plotted at different loop positions for the parameter $\Gamma = 1.04$ and $\Gamma = 1.48$. From this figure it becomes clear that the frequency interval of the absorbed waves ranges between the frequencies (Ω_0/Γ^2) and Ω_0 which is the gyrofrequency at the footpoints.

According to the Fig. 4.5 left panel, at the position $s \approx 6$ Mm which is not far from the left footpoint, those waves having frequencies close to $\Omega_p(s)$ have already been absorbed at altitudes lower than $s = 5$ Mm, and below this position the dissipation rate can reach its maximum $1.19 \times 10^{-4} \text{J m}^{-3} \text{s}^{-1}$ (see Table 1). Thus parts of the wave energy spectrum are

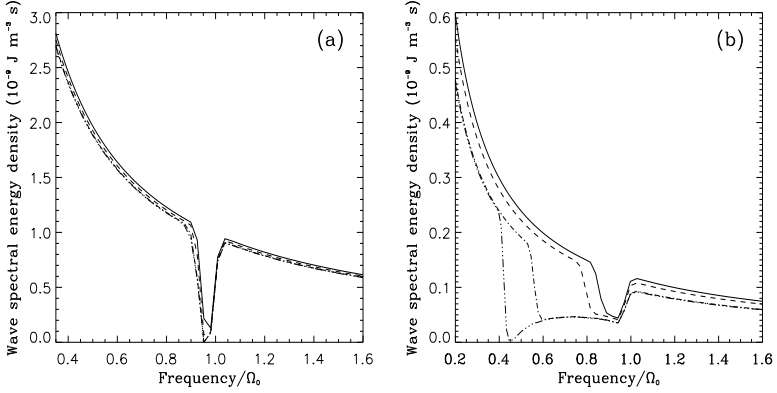


Figure 4.5: The wave spectral energy density plotted in dependence on normalized frequency for $\Gamma = 1.04$ on the left panel and for $\Gamma = 1.48$ on the right panel at different positions $s = 3.3$ Mm (line), $s = 5.3$ Mm (dashed line), $s = 15.6$ Mm (dashed dotted line) and $s = 31.4$ Mm (dashed double-dotted line).

eroded since the waves were strongly dissipated at positions lower than $s = 3$ Mm, as it is indicated by the continuous line in the figure. This implies a small heating scale height that corresponds to footpoint-type heating. Furthermore, the same figure shows in the left panel that the proton gyrofrequency is situated nearly in the same narrow frequency domain at different loop positions, because of small magnetic field variation along the loop.

Thus, from Fig. 4.5 right panel we can infer that the protons can be in resonance with waves over a wider interval of frequencies in the spectrum. The so-called frequency "sweeping mechanism" (Tu and Marsch, 1997) can clearly be seen here. At $s = 3$ Mm the continuous line indicates absorption around the proton gyrofrequency, and since this gyrofrequency decreases toward lower frequencies, as long as we move to the loop top at ~ 31 Mm, the interval of the absorbed frequencies also moves toward the loop top, as it is shown with the other-style lines in this figure. This leads to local heating, and consequently a relatively larger heating scale height that corresponds to a quasi-uniform heating along the left side of the loop (see Table 1.). Therefore, most waves get absorbed, and not enough wave energy is left for the right half of the loop.

The expansion factors considered in this study indicate that in loops (with $L \approx 62$ Mm) which are not much thicker at the top than at the footpoints those waves with $\omega > \Omega_p$ are not allowed to propagate towards the loop top. Due to the rapid absorption of the waves inside the loop close to the local gyrofrequency, the intensity of waves with $\omega > \Omega_p$ becomes negligible. Protons can fall in resonance only with waves having $\omega < \Omega_p$,

Table 4.1: The wave energy flux F_1 and the dissipation rate Q_1 for $\Gamma = 1.04$, and F_2, Q_2 for $\Gamma = 1.48$.

s (Mm)	F_1 ($\text{J m}^{-2} \text{s}^{-1}$)	Q_1 ($\text{J m}^{-3} \text{s}^{-1}$)	F_2 ($\text{J m}^{-2} \text{s}^{-1}$)	Q_2 ($\text{J m}^{-3} \text{s}^{-1}$)
3.33	1.78×10^2	11.98×10^{-5}	4.37×10^2	8.54×10^{-5}
5.37	1.31×10^2	1.64×10^{-5}	3.72×10^2	2.77×10^{-5}
7.23	1.12×10^2	7.15×10^{-6}	3.28×10^2	2.2×10^{-5}
10.56	97.91	2.95×10^{-6}	2.59×10^2	1.87×10^{-5}
15.74	90.39	0.96×10^{-6}	1.72×10^2	1.44×10^{-5}
20.89	87.97	0.3×10^{-6}	1.09×10^2	8.22×10^{-6}
31.41	86.58	0.13×10^{-6}	64.44	4.31×10^{-6}

according to the resonance condition

$$\omega = \Omega_p(s) \frac{v_{ph}}{v_{ph} - v_{\parallel}}, \quad (4.42)$$

which means only protons with negative velocities (if $k > 0$) can resonate with Alfvén-cyclotron waves. This justifies our assumption of dispersionless waves since the constraint $\omega < \Omega_p$ derived from the proton-cyclotron-wave dispersion relation is already satisfied. This consideration also applies to waves that enter the loop from the right side and have a wavenumber $k < 0$ and frequency $\omega > 0$. Thus, only waves $\omega < \Omega_p$ can resonate with protons having positive velocities. Consequently, the waves propagating in opposite directions into the loop from both sides do not interfere.

From the sketch given by Fig. 4.6, we can more explain the resonant wave-particle absorption and the sweeping mechanism. The perpendicular axis in this figure belongs to the frequency of waves that enter from the left footpoint. In this sketch, it is clear that only waves having frequencies close to proton gyrofrequencies are able to interact and transfer a big part of their energy to the protons. The frequency of these waves is ranging between $\Omega - \Delta\omega$ and $\Omega + \Delta\omega$, which denotes the interval of the resonant frequency satisfying the resonant condition (4.42). The estimation of $\Delta\omega$ given in Fig. 4.7 is computed assuming the proton thermal speed, v_{th} , as the typical value for the absolute value of the parallel proton velocity component $|v_{\parallel}| \approx v_{th}$. With $|v_{ph}| \approx v_A$, we thus get $\Delta\omega \approx \frac{v_{th}}{v_A} \Omega$.

The sketch in Fig. 4.6 shows the initial waves entering the loop from the left footpoint. Then only those waves having a resonant frequency close to the proton gyrofrequency Ω_0 get absorbed. At the adjacent position s_1 , the proton gyrofrequency slightly decreases, and thus an opportunity is given to other initial waves having frequencies close to Ω_1 to interact with protons. However, at the position s_1 only resonant waves with $\omega_{res} \lesssim \Omega(s_1)$ efficiently interact and transfer their energy to the protons. This is because the resonant waves with $\omega_{res} \gtrsim \Omega(s_1)$ mostly get eroded at the precedent point. The same explanation of the wave absorption by protons can be applied to the rest of the grid point until the loop top where the proton gyrofrequency stops decreasing.

Notice the wave-particle interaction with $\omega_{res} \lesssim \Omega(s)$ implies that waves interact with protons when only having negative v_{\parallel} . However, in the case of waves entering from the right boundary, the same explanation of the sweeping mechanism given above for waves

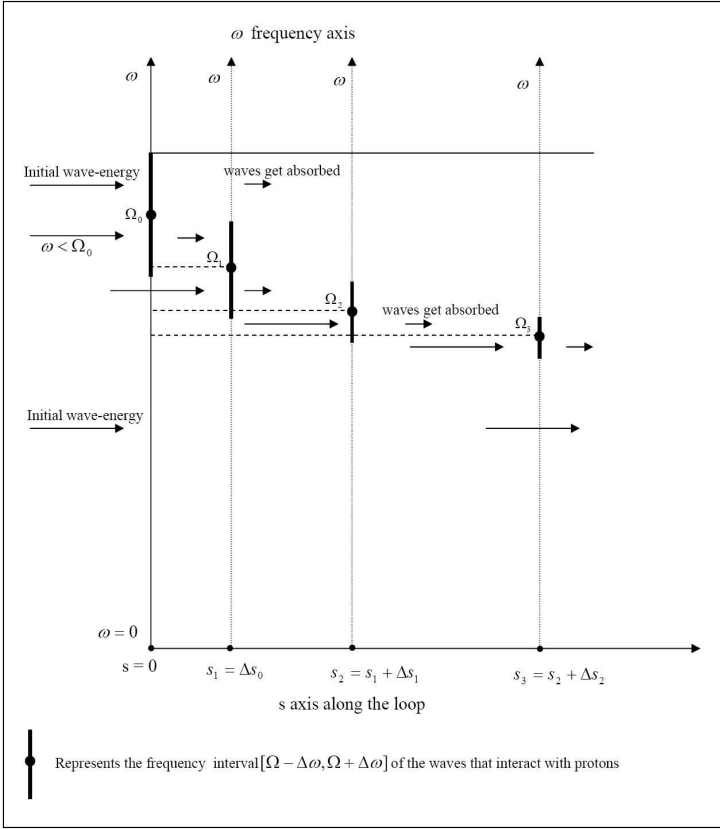


Figure 4.6: The wave-absorption mechanism.

entering from the left footpoint can be valid, but the interaction of waves would now be with protons having $v_{\parallel} > 0$, since $v_{ph} < 0$ when dealing with the resonant condition (4.42).

Furthermore, we deduce from Fig. 4.7 that the interval of the resonant frequency $[\Omega - \Delta\omega, \Omega + \Delta\omega]$ is larger close the boundaries (due to the highest value of $\Delta\omega$). This is because at positions close to the footpoints the Alfvén speed (or phase speed) is decreasing due to the enhancement in electron density, and thus $\Delta\omega$ gets increased. Therefore, the resonant wave interval at positions close to the boundaries are wider. This leads to more wave-particle absorption and a stronger increase of the proton temperature at these positions.

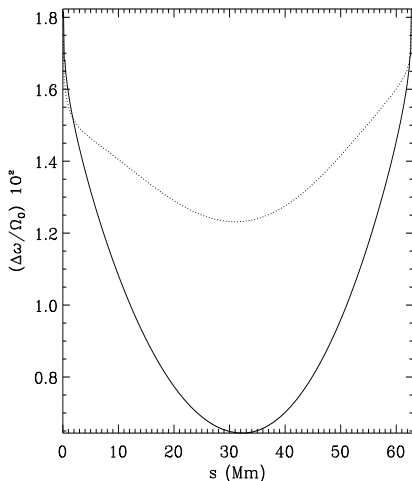


Figure 4.7: The estimated width $\Delta\omega$ for the frequency interval $[\Omega - \Delta\omega, \Omega + \Delta\omega]$ of waves that fall in resonance with proton gyrofrequency at the position s for $\Gamma = 1.04$ (dotted line), $\Gamma = 1.48$ (solid line).

4.4.3 Symmetric heating

Our goal in this simulation is to produce a static loop with symmetric heating. For that purpose we assume that Alfvén waves penetrate with the same wave-power density and wave energy flux ($F_0 \approx 7 \times 10^2 \text{ J m}^{-2} \text{ s}^{-1}$) the simulation domain from both footpoints of the loop and simultaneously heat the plasma. As we argued in the previous subsection, no interference between these two wave spectra has been considered. Here we also deal with two values of the parameter of inhomogeneity, $\Gamma = 1.04$ and 1.48 that defines the magnetic flux tube area along the semi-circle guiding field line of the loop.

As it is shown in Fig. 4.8 for $\Gamma = 1.48$, the loop starts to be heated from either side, and at the initial time $t = 0$ the loop is cooler and denser with homogeneous temperature and density distribution: $T(t = 0) = 2 \times 10^5 \text{ K}$, and $N(t = 0) = 5 \times 10^{15} \text{ m}^{-3}$. Then due to the dynamical effects of the external forces (gravity, electrostatic field, and mirror force) on the proton VDFs and owing to wave energy dissipation, the protons can be heated from both loop sides. Concurrently, the overall density in the loop becomes smaller until the system relaxes within $3 \times 10^4 \text{ s}$ to a final steady state with quiescent symmetric plasma-parameter profiles. The final steady states for all Γ parameters are given in Fig. 4.9.

For $\Gamma = 1.04$ the loop plasma is overdense compared to the plasma in a relatively expanding cross section, and the electron and proton temperatures profile are symmetric. These profiles reflect that the plasma loop is heated from either side. In fact, what is

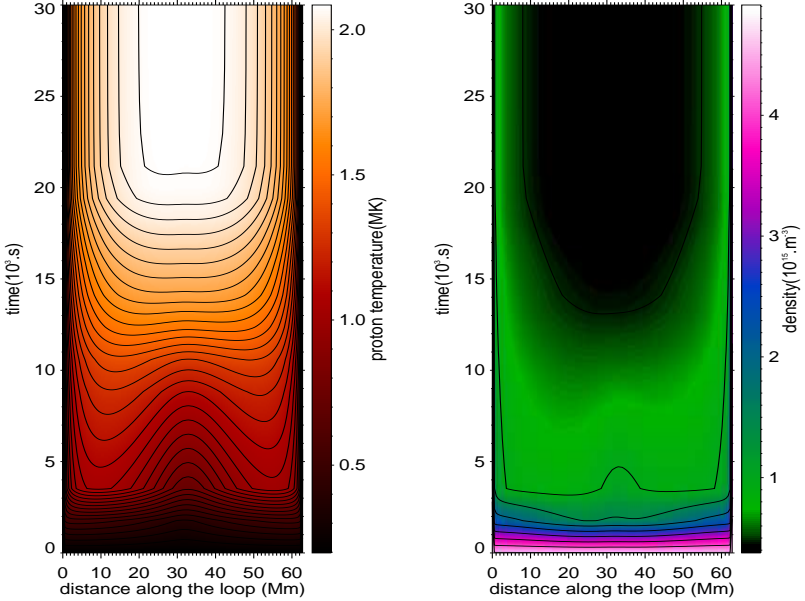


Figure 4.8: The time evolution of the plasma temperature (left) and density (right) for $\Gamma = 1.48$ versus distance along the loop.

important in the case of symmetric heating is that the loop can be more isothermal, with the temperature being ~ 1.3 MK along a large section of the coronal loop in comparison with the asymmetric heating.

Due to the close connection between the wave-energy dissipation scale along the loop and the variation of its cross-section area (see Fig. 4.9d), it turns out that with this loop model it is possible to produce soft X-ray loops, which are the consequence of a more diverging magnetic field in the top parts of the loops. Apparently, these types of loops are hot and have a flat temperature maximum ≥ 2 MK that is centered around the top segment of the loop. Notice that the collisions are relatively strong and suffice to maintain isotropy of the proton VDF, but we expect that with more heating (caused by more strongly expanding magnetic field lines) the effects of the collisions will decrease. The pressure along the loop in this model is not constant, as it is demonstrated in Fig. 4.10, and for the case of asymmetric heating the pressure profile itself shows a small asymmetry. The thermal pressure gradient tries not only to balance the dynamical external forces but also the Alfvén-wave pressure gradient which acts asymmetrically on the left side of the loop. But when the loop is symmetrically heated, the total pressure looks quite symmetric, since the wave pressures acting on the loop at its two legs are equivalent. Notice that no temperature anisotropy appears in the plasma, which means the collisional mean

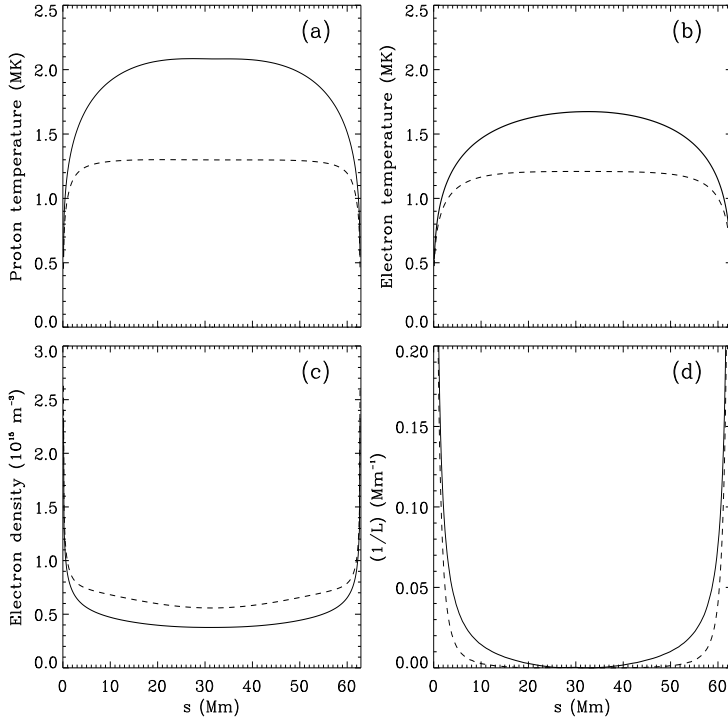


Figure 4.9: The proton temperature (upper left panel), electron temperature (upper right), density (lower left), and heating scale length (lower right) for $\Gamma = 1.48$ (line) and $\Gamma = 1.04$ (dashed line) versus distance along the loop.

free path, λ , is still short enough as compared to the proton temperature scale length, $L = (\frac{1}{T} \frac{\partial T}{\partial s})^{-1}$ in Fig. 4.9d, to maintain a proton VDF close to a Maxwellian.

At this stage, it seems useful to make a comparison between the kinetic and the macroscopic (fluid) transport theory for protons. For this purpose, we compute the proton heat conduction via the third moment of the VDF in (4.4) and compare it with that derived from Braginskii's (1965) formula. The results are given in the three panels of Fig. 4.11, which refers to the two values of $\Gamma = 1.04$ and 1.48. We plot the scale ratio parameter $\alpha(s) = \lambda(s)/L(s)$ in the upper left panel. This plot permits us to judge how small this parameter must be to ensure the validity of the classical proton heat conduction (Fourier's

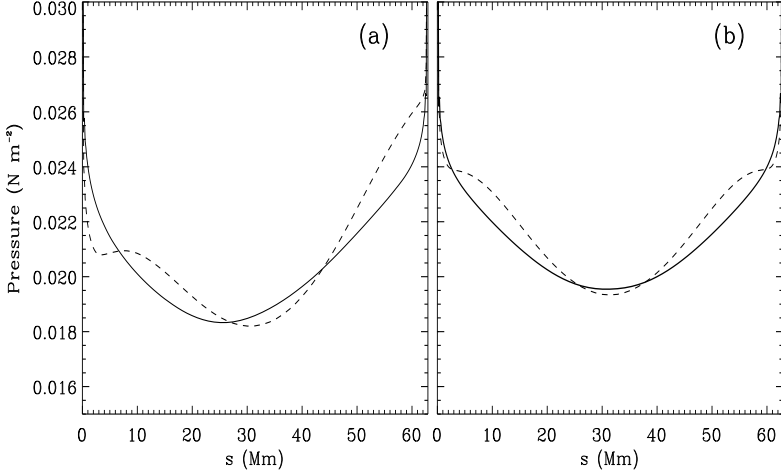


Figure 4.10: The total pressure for asymmetric wave heating (left panel) and for symmetric heating (right panel) for $\Gamma = 1.48$ (line) and $\Gamma = 1.04$ (dashed line) shown versus distance along the loop.

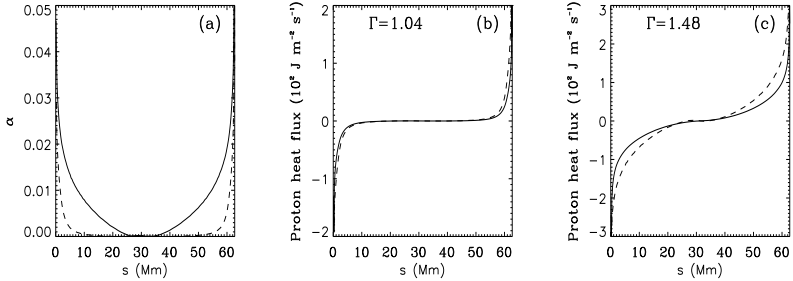


Figure 4.11: The $\alpha(s)$ parameter is plotted (left panel) for $\Gamma = 1.48$ (line) and $\Gamma = 1.04$ (dashed line) versus distance s along the loop. The other two panels give the kinetic proton heat flux (line) and the classical heat flux (dashed line) shown versus distance along the loop.

law) formula, which requires that $\alpha(s) \ll 1$ (Chapman-Enskog regime) at every position s along the loop.

According to these four figures the kinetic proton heat conduction is not far from its classical value for the two Γ parameters, however it seems that the kinetic proton heat flux does clearly differ from the classical one by factor of two close the loop footpoints for a more strongly expanding cross-sectional area along the loop. This situation corresponds to a parameter α which is of the order of 2×10^{-2} . For nearly constant cross sections, e.g. $\Gamma = 1.04$, the kinetic ion heat flux looks quite identical to the classical one (see the right panel of Fig.4.11). A significant difference can only be seen close to the loop footpoints at which remarkable deviations of the kinetic heat flux from the classical one can occur. In fact, this effect is related to the shape of the VDFs. As long as we are close to a Maxwellian VDF, the macroscopic collisional fluid description seems valid, but for any deviation from a local Maxwellian a consistent kinetic description of the various moments is required.

4.5 Conclusion and discussion

In this chapter we studied the wave heating of coronal loops. For that purpose we developed a hybrid model in which the kinetic Vlasov equation for the reduced ion VDFs was used for protons, and electrons were treated as a fluid in hydrostatic equilibrium. The Vlasov equation includes wave-particle interactions as described within the framework of quasilinear theory and Coulomb collisions between the particle species. When considering ion-cyclotron-wave heating, it turns out that the proton heating has a strong spatial connection with the variation of the cross-section-area along the loop. It is deduced that footpoint-type heating with a small scale height is a consequence of a quasi-homogeneous flux tube, in which the proton temperature remains nearly constant in a large section of the loop. However, if the magnetic field of the loop is more diverging from both footpoints to the apex, the heating scale height of the protons is larger. The resulting strong wave absorption at many different positions leads to quasi-uniform loop heating.

In this model, the electrons can be heated through the Coulomb-collision coupling between protons and electrons, and consequently the temperature electrons can reach in a coronal loop depends on the proton heating. However, the electrons while having to power the radiative losses tend to be cooler than the protons, especially close to the footpoints where the electron density is higher. But electrons further cool due to heat conduction which is proportional to $T_e^{5/2}$. Consequently, the heating profile of the electrons is connected with that of the protons as long as their temperature stays below ≈ 1 MK; beyond this value, thermal diffusion associated with the electron heat conduction more strongly reduces the electron temperature and renders the electron temperature profile more uniform.

Therefore, it turns out that the model can produce both types of observed coronal loops, i.e. the EUV as well as X-ray loops, in dependence upon the magnetic flux tube geometry that shapes the plasma loop. The EUV loops can be modelled well if the cross-section area, corresponding to the magnetic field line density in the loop, is more homogeneous with $\Gamma \approx 1.04$. However, the X-ray loops observed with a quasi-uniform heating can arise in our model if the cross section expands, with $\Gamma \approx 1.48$.

In addition to the remote-sensing evidence for ion heating obtained by the Solar and Heliospheric Observatory (SOHO), which is based on spectroscopic determinations of the

widths of extreme ultraviolet emission lines and indicate that the heavy ions are hotter and more accelerated in polar coronal hole, also strong in-situ evidence for ion heating and plateau formation was found in solar wind proton velocity distribution functions (Heuer and Marsch 2007). All these measurements have been interpreted in terms of kinetic wave-particle interactions, and are believed to be mainly caused by resonant diffusion of ions in the Alfvén/ion-cyclotron wave field. These observations relate to the fast solar wind emanating from magnetically open coronal holes.

Here we have for the first time applied similar theoretical concepts to the heating of coronal loops, i.e. the closed magnetic structures on the Sun. Our theory reveals a close connection between the spatial heating (due to resonant wave-particle interaction) along the loop and the magnetic flux tube expansion as measured from the footpoints to the top. In fact, an expanding magnetic flux tube leads to local dissipation of the Alfvén ion-cyclotron waves which is needed for strong heating and acceleration of ions beyond 2 solar radii. Uniform heating can only occur at larger distances since the magnetic field decreases more slowly within the solar wind region. However, in case of coronal loop, where the flux tube is expanding less than a coronal funnel, the heating tends to be more non-uniform. Since the resonant absorption of ion-cyclotron waves is fast process, the waves can dissipate at lower heights close to the transition region, and this heating is efficient for coronal loop heating.

Thus, it turns out that this variation of the cross-sectional area plays an important role in determining the thermodynamic structure of a loop in this model. However, the coronal magnetic field still cannot be directly measured with sufficient accuracy, but rather can be diagnosed and inferred only by using the intensity features observed in coronal loop images. According to some linear force-free magnetic field extrapolation models for loops (see e.g., López Fuentes et al. 2006), in some cases the modeled flux tubes expands twice as much as the observed TRACE loops from the footpoint to the loop apex.

It is therefore surprising that soft X-ray, EUV, and visible-light images all give the impression as if coronal loops are less thick (e.g Golub et al. 1990) but more constricted. Also, some measurements of the expansion of loops (as observed by TRACE in the 171 Å and 195 Å band passes with better spatial resolution) exhibit expansion factors of $\Gamma \approx 1.1$ (Watko and Klimchuk 2000). These results appear to be consistent with the predictions of our model, which produces EUV loops with roughly constant temperature along most segments of the loop. Also, further loop observations made by YOKOH in soft X-rays (Klimchuk 2000) showed expansion factors ranging between 1 and 1.5, which means that most loops are not strongly expanding near their tops. A further comparison of the predictions of this model with observations will be made in the planned future work, in which we shall also include the effects of minor ions on the loop temperature profile.

5 Multi-ions kinetic model for coronal loop

5.1 Introduction

The solar corona is weakly collisional and far from Local Thermal Equilibrium (LTE). Particularly, a coronal loop, although it is denser than the surrounding plasma, might also not be in LTE. Therefore, the coronal loop has to be described more realistically by the kinetic Vlasov equation. Furthermore, the loop heating mechanism presumably acts on a scale smaller than the mean free path of the particles. Consequently, HD or MHD models will not be able to explain the heating of coronal loops, and within fluid theory one cannot understand the origin and location of the heat source along the loop. Thus, in such weakly collisional conditions a kinetic description of the coronal loop plasma is inevitably needed.

Following the same theory given in chapter 4 for the coronal loop modeling, in this chapter, some other minor ions like Helium ions, He^{2+} , and oxygen ions, O^{5+} are included in addition to the electrons and protons in the plasma loop model. Here, we aim to study the heating of these minor ions via the resonant wave-particle absorption, and see their effect on the heating of protons and electrons. Also, we show the circumstances in which the plasma loop can be close to or far from LTE.

Such a study allows us to extract the salient impacts and main effects that small-amplitude cyclotron waves may have on the heating of coronal loops in presence of collisions, which still turn out to be efficient in loops as compared with the more tenuous outer corona and dilute solar wind.

The coronal loop model theory used here is well described in the previous chapter, where an ensemble of PDE equations (4.3), (4.6), (4.12) and (4.14) are involved, and where the ion species are described kinetically in terms of their reduced velocity distribution functions (VDFs). Also, a semicircular cylindrical geometry for the coronal loop flux tube is adopted, whereby the varying loop cross-section is obeying the equation (4.1) (with the total loop length, $L \approx 63$ Mm).

In the model, a power-law spectrum is assumed for the non-dispersive Alfvén waves originating below the transition region. The ion heating is associated with the dissipation of these waves via ion-cyclotron resonance obeying the condition, $\omega - k_{\parallel}v_{\parallel} - \Omega_i = 0$, with the parallel wave vector k_{\parallel} and wave frequency ω , and the ion gyrofrequency $\Omega_i(s) = q_i B(s)/m_i$, which varies along the loop with the spatial coordinate s . At the footpoints (where the boundary conditions are set) we assume the following ion abundances, $N_{\text{He}} = 0.1N_p$ and $N_{\text{O}} = 0.001N_p$, with $N_p = 4.15 \times 10^{15} \text{m}^{-3}$, and the temperature $T_0 = 2 \times 10^5$ K.

The magnetic field at $s = 0$ is $B_0 = 80$ G. The initial conditions are chosen to be constants, i.e., all the species have the same temperature, $T(s) = T_0$, and the abundance for each ion species is assumed to be the same as at the footpoints. Here we also deal with two values of the expansion factor, $\Gamma = 1.04$ for a nearly homogeneous loop and $\Gamma = 1.48$ for a more expanding loop, (see Fig. 4.2). At $t = 0$ the waves start to propagate close to the left footpoint, with the power-law spectrum density given by $\mathfrak{B}_\omega(s = 0) \approx 2.8 \times 10^{-4} [\omega \log(\Gamma^2)]^{-1} \text{ J m}^{-3} \text{ s}$. Generally, the frequency interval used in this study ranges between $\Omega_0(s = 0)/\Gamma^2$ and $\Omega_p(s = 0)$. Notice that for Γ varying between 1.04 and 1.48, the integrated power-law spectrum is equivalent to an overall nonthermal velocity ranging between 14 and 38 km/s, which is consistent with the observational constraints (Wilhelm et al. 2007).

5.2 Results

5.2.1 Plasma loop profiles

The kinetic temperature, which is of prime interest in this study, is plotted for each ion species in Fig. 5.1a and Fig. 5.1b. In case of $\Gamma = 1.48$, protons and He^{2+} ions show the same isotropic temperature profiles along the loop. However, the heating of O^{5+} in the left part of the loop is higher in the perpendicular direction with respect to the mean magnetic field. This leads to a remarkable temperature anisotropy, with $T_\perp/T_\parallel > 1$. The kinetic parallel temperature of O^{5+} , $T_{\parallel, \text{O}^{5+}}$, hardly differs from the temperatures of the other ion species. The perpendicular temperature $T_{\perp, \text{O}^{5+}}$ behaves differently, as it increases rapidly and then reaches values up to 5 MK at $s \approx 16$ Mm, leading to a maximal temperature anisotropy with $T_\perp/T_\parallel \approx 2.5$. On the right side of the loop, at which the wave absorption is negligible, all ion species have the same heating profile, and thus isotropy is well maintained. In this part, the ion temperature decreases at the loop apex to the right boundary at $s = L$ under the effects of ion heat conduction and ion-electron collisions.

When the loop width is nearly homogeneous ($\Gamma = 1.04$), the temperature isotropy is well preserved beyond a distance of 5 Mm, as it becomes clear in Fig. 5.1a. The kinetic temperatures of each species are similar and roughly constant along a big part of the loop. Only a remarkable anisotropy in the oxygen temperature occurs close to the left footpoint, where the wave absorption is relatively stronger than elsewhere.

In Fig. 5.1c the electron density is plotted for both cases of the expansion factor. The loop with a quasi-constant cross section ($\Gamma = 1.04$) has an enhanced density in comparison with the loop having a more expanding cross section ($\Gamma = 1.48$). Furthermore, in both cases the loop is dynamic with a non-thermal subsonic flow speed (see Fig. 5.1d). The flow in the loop is needed to guarantee that particle flux is conserved in the final relaxed state of the plasma (see Fig. 5.1f). Indeed, the non-thermal drift speed can reach $\approx 20 \text{ km s}^{-1}$ in case of $\Gamma = 1.04$. This bulk flow speed ranges within the values often observed in active-region loops (Aschwanden et al. 1999, Chae et al. 2000, Winebarger et al. 2002, Marsch et al. 2004).

In the kinetic multi-ions model, the electrons are found to be cooler than the ions. The electron thermal energy gained from ion-electron collisional heat exchange is reduced by the effect of radiative losses and the strong heat conduction of the electrons. The latter

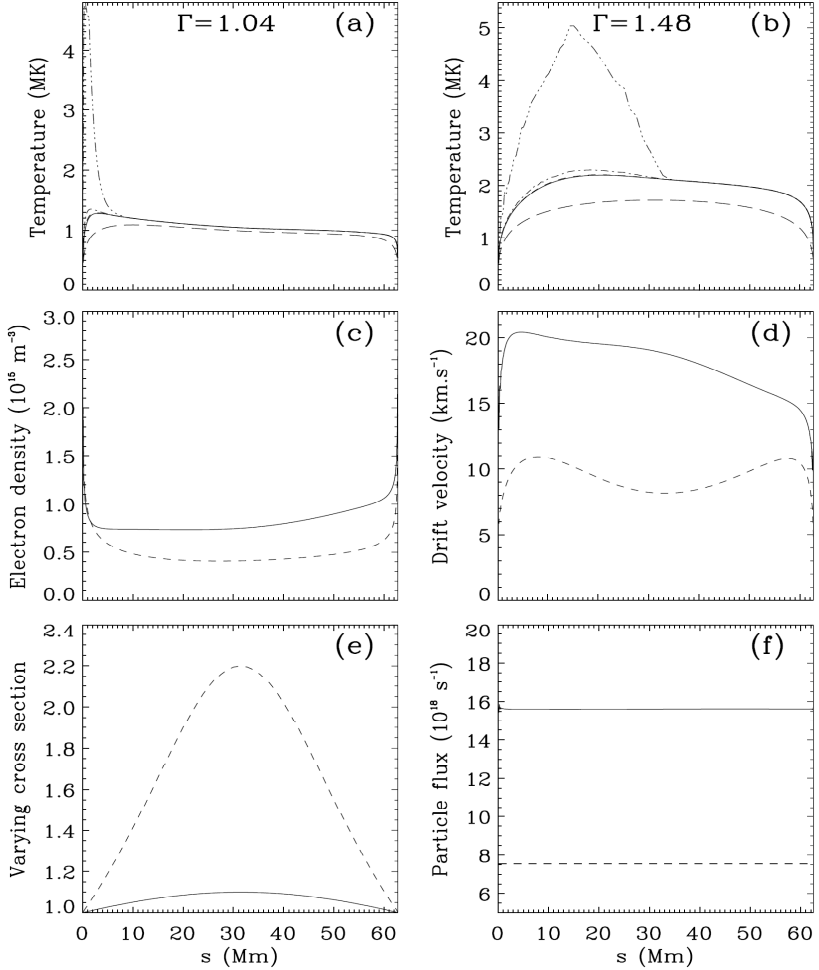


Figure 5.1: (a),(b) Proton and helium temperature (line), $T_{\parallel, O^{5+}}$ (dashed dotted line), $T_{\perp, O^{5+}}$ (dashed double-dotted line) and electron temperature (dashed line) are plotted for $\Gamma = 1.04$ in panel (a) and $\Gamma = 1.48$ in (b) as a function of distance s along the loop. (c) Electron density, (d) flow speed, (e) varying cross-section, and (f) the particle flux are all plotted for $\Gamma = 1.04$ (line) and $\Gamma = 1.48$ (dashed line) as a function of distance along the loop.

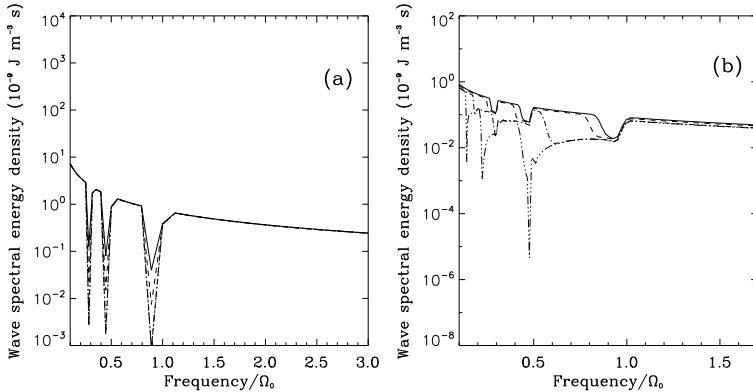


Figure 5.2: The wave spectral energy density plotted in dependence on the normalized frequency for $\Gamma = 1.04$ on the left panel and for $\Gamma = 1.48$ on the right panel at different positions $s = 3.3$ Mm (line), $s = 5.3$ Mm (dashed line), $s = 15.6$ Mm (dashed dotted line), and $s = 31.4$ Mm (dashed double-dotted line). Here $\Omega_0 = \Omega_p(s = 0)$

process, in which the heat conductivity is proportional to $T_e^{5/2}$, is more efficient when the electron temperature T_e exceeds 1 MK. This will result in a loop having a more expanding loop width (see Fig. 5.1b) and a situation in which the electron temperature is much higher and more uniform than in the constricted loop. However, when the loop width is nearly uniform the electron and ion temperatures are almost identical in a big part of the loop.

5.2.2 Wave-absorption mechanism

The coronal heating mechanism in loops can well be explained as being due to wave absorption of the ions (as shown in Fig. 5.2). When starting with a loop having a larger expansion factor (see Fig. 5.2b), it turns out that the ions can be in resonance with waves over a wider interval of frequencies in the wave spectrum. At $s \approx 3$ Mm the solid line indicates absorption around the three ion gyrofrequencies. Since these gyrofrequencies decrease as long as the flux tube keeps opening up to the loop apex, those frequencies at which absorption occurs move to ever lower values in the spectrum. This change is now leading to quasi-local heating, with a relatively larger heating length scale on the left (where the waves are injected) side of the loop. It is noteworthy that the protons can strongly be heated by wave energy absorption until a distance $s \approx 20$ Mm at which the proton gyrofrequency becomes close to the helium one at the footpoint ($\Omega_p(s \approx 20) \approx \Omega_{He}(s = 0)$). Beyond this distance those waves that could interact with protons were already absorbed by helium at lower heights in the left part of the loop. Similarly for helium ions, these ions can more strongly be heated within distances below $s \approx 13$ Mm. Beyond this distance, most of the power of those waves that could fall in resonance with helium ions was

already decimated by wave-oxygen interactions at lower positions in the loop. Despite this fact, the heating profiles of protons and He^{2+} overlap, because of efficient energy exchange by proton-helium collisions.

However, oxygen ions can be heated from lower positions up to the loop apex, as it is clear in Fig. 5.2b, since they have the lowest gyrofrequency ($\Omega_{\text{O}} = 0.312 \Omega_{\text{p}} = 0.624 \Omega_{\text{He}}$). Therefore, oxygen ions can interact with waves that have more wave power, and due to the small abundance of O^{5+} , the absorbed wave energy is distributed over a much lower number of oxygen ions than is the case for protons. Stronger perpendicular than parallel heating is the basic result of ion-cyclotron-resonance absorption. Therefore, the oxygen ions will finally attain the highest perpendicular temperature of all ions considered here.

Because of the small variation of the magnetic field along the loop in case of $\Gamma = 1.04$, ions can be in resonance with waves only over a narrow interval of frequencies close their gyrofrequencies $\Omega_i(s = 0)$ (see Fig. 5.2a). These waves have already been absorbed at altitudes lower than $s \approx 5$ Mm. Below this position the three ions can be heated, with a preferential heating for oxygen, since its ions have the lowest gyrofrequency and a very small abundance in the coronal plasma. This model shows that most of the resonant waves have been absorbed by the ions via the "frequency-sweeping mechanism", as described previously by Tu and Marsch (1997) and Vocks and Marsch (2002). Therefore, most of the waves get already absorbed at lower heights, and not enough wave energy is left for heating the right half of the loop.

In comparison to the heating profile found in the previous chapter for a loop consisting of electrons and protons, it seems that the additional minor ions hardly affect the temperature of electrons and protons. Their collisional energy exchange with the heavy ions has no measurable thermal impact because of the very low minor ion density, and also because of the proton temperature which exceeds 1 MK. This makes their collisions weaker in comparison with the case when the protons are cooler.

5.2.3 Ion VDFs in case of $\Gamma = 1.48$

The temperature anisotropy of the heavy ions, which is represented here by O^{5+} , implies that their usual VDFs is not Maxwellian. Assuming a Maxwellian in v_{\perp} , a two-dimensional gyrotropic VDF $f(v_{\parallel}, v_{\perp})$ can be obtained (see equation (3.13)).

Figs. 5.3-5.5 display the time evolution of VDFs of the three ions species, proton, helium and oxygens at the position $s = 16$ Mm. At the initial time, $t = 0$, the VDFs of the ions are Maxwellian describing a local thermal equilibrium system with $T_p = T_{\text{He}} = T_{\text{O}} = T_0 = T_e = 2.10^5$ K. It turns out that the VDFs of proton and helium species remain isotropic during the time evolution to the relaxing steady state. The circles, which represent the contour plots of the Maxwellian distribution, expand with time, implying ion heating locally in space (here at position $s=16$ Mm far from the left footpoint). Therefore, the diffusion of protons and helium ions is more isotropic due to the efficiency of the Coulomb collisions comparing to ion heating process.

However, the oxygen VDFs behaves differently in Fig. 5.5. At the initial time, $t = 0$, this VDFs is isotropic have a shape like a Maxwellian distribution that is represented by circular contour centred at the normalized drift speed. Then at $t = 800$ s, these circles expand more due to the diffusion process of the oxygen ions under the effect of the wave-particle absorption.

Notice that, at time $t < 800$ s, the oxygen VDFs is still isotropic due to the efficiency of the Coulomb collisions when the ion temperature is still below 1 MK. As long as the kinetic thermal energy of the oxygen increases in time, the collisions will not be able to thermalize efficiently these ions. Consequently, their VDF are shaped asymmetrically via the wave-particle diffusion process. This asymmetric form starts to appear at $t = 2000$ s (see Fig. 5.5d) when the contour plots deviated from their initial circular shapes and thus indicate a preferential perpendicular heating.

The resonant wave-particle interaction term by diffusion drives the particle's VDF to attain vanishing pitch-angle gradients in the wave frame of reference according to quasi-linear theory, which is supported by solar wind in situ observations (Marsch and Tu 2001, Heur and Marsch 2007), while the Coulomb collision operator tends to thermalize the plasma, and to make the particle VDFs isotropic.

At $t = 10^4$ s, the oxygen VDF reaches its steady final state, and it is plotted for several positions along the loop as shown in Fig. 5.6. The VDF, at the lower position around 3 Mm, is close to Maxwellian, and around the positions $s = 7.2$ and $s = 10.5$ Mm, the oxygen VDFs expand more asymmetrically leading to a remarkable oxygen temperature anisotropy. Furthermore, when the heating of oxygen is in its maximum at $s \approx 18$ Mm, the VDF is very far from a Maxwellian and shows a preferential perpendicular heating with respect to the local magnetic field. Then at larger distances ($s > 20$ Mm), the oxygen VDF shrinks again towards a more symmetric form, as shown in Fig. 5.6f for the case of $s = 30$ Mm. This is expected since the wave dissipation process stops at position $s \approx 20$ Mm along the loop for the reasons mentioned in the previous subsection. Consequently, in the remaining part of the loop (at $s > 30$), the collisions will be more efficient to thermalize the plasma again, a process leading to a Maxwellian VDFs for the all ion plasma species.

In the diffusion process, ions having ($v_{\parallel} < 0$) on the tails of the VDF are much more spread. These particles while moving inward ($v_{\parallel} < 0$) can fall in resonance with waves having frequencies $\omega < \Omega_p(s)$, but have a negligible interaction with waves at frequencies $\omega > \Omega_p(s)$, since these waves will reach the position s with low wave energy. The reason is that their energy was already eroded at lower heights in the loop. This means the model assumption of dispersionless Alfvén/cyclotron waves is also well justified.

5.3 Conclusion and discussion

In this chapter the heating of a coronal loop is modelled by using the kinetic description and including wave-particle interactions which are based on the quasi-linear approximation of the Vlasov equation. Alfvén/cyclotron waves are assumed to penetrate the plasma in the coronal loop from one footpoint, and thus to heat the ions asymmetrically via resonant wave absorption. Consequently, asymmetric heating occurs, with the spatial dissipation scale being connected with the variation of the loop width. In this way dynamical loops with a moderate non-thermal drift speed (subsonic bulk flow) can be produced.

We neglected in our model possible dissipation caused by plasma inhomogeneity across the loop. We are aware of theoretical considerations suggesting that cross-field plasma nonuniformity might be crucial also for the dissipation of high-frequency Alfvén-cyclotron waves, which can undergo nonlinear processes and suffer strong phase mixing, thus leading to fast Landau damping (see, e.g., Voitenko and Goossens 2000a,b,

and references therein). Even though Landau damping, in the circumstance when the loop is nonuniform and of filamentary nature across the magnetic field, can occur it will have a minor effect as long as the related dissipation length z_{\perp} is comparatively large, i.e. $z_{\perp} \gtrsim 100$ km which is the characteristic length scale of field-aligned ion-cyclotron damping in our model. This condition on z_{\perp} means that Landau damping only matters if $L_{\perp} \leq 10$ km, an inequality that is obtained by using equations (11) and (30) as given in the paper of Voitenko and Goossens (2000b). The required short filamentation length L_{\perp} is roughly 100 times smaller than the typical thin-loop diameter of about 1 Mm, which can be observed within the resolution of TRACE yields the smallest scale that can presently be resolved.

In the present model it is found that the footpoint-type loop heating with a small scale length is the consequence of a quasi-homogeneous magnetic flux tube, in which the electron density is enhanced and stays roughly uniform in the loop. Apart from the region close to left footpoint, the plasma can remain close to LTE with a uniform temperature around 1 MK along the loop. These loop features seem to be consistent with those observed in the emission of so-called EUV loops.

However, if the loop width expands more strongly from its footpoints to the apex, the heating scale length for the ions becomes larger. In such case, the plasma can evolve to a state far from LTE, and a considerable temperature anisotropy occurs in O^{5+} (minor heavy ions), where the strong wave dissipation is taking place in the loop. The electrons, which can be heated through the Coulomb-collision coupling between ions and electrons, still remain cooler than the ions, due to their high heat conduction as well as sizable radiation losses.

These plasma loop features, i.e. the electron temperature and density profiles as well as the plasma flow driven by ion dynamics, may together explain the hot dynamical loops as they are observed at wavelengths between soft X-rays and the EUV. These kind of loop features were in the literature (e.g., Klimchuk 2000) usually reproduced by using hydrostatic models, which yet are not able to explain the existence of gentle flows as observed in such loops.

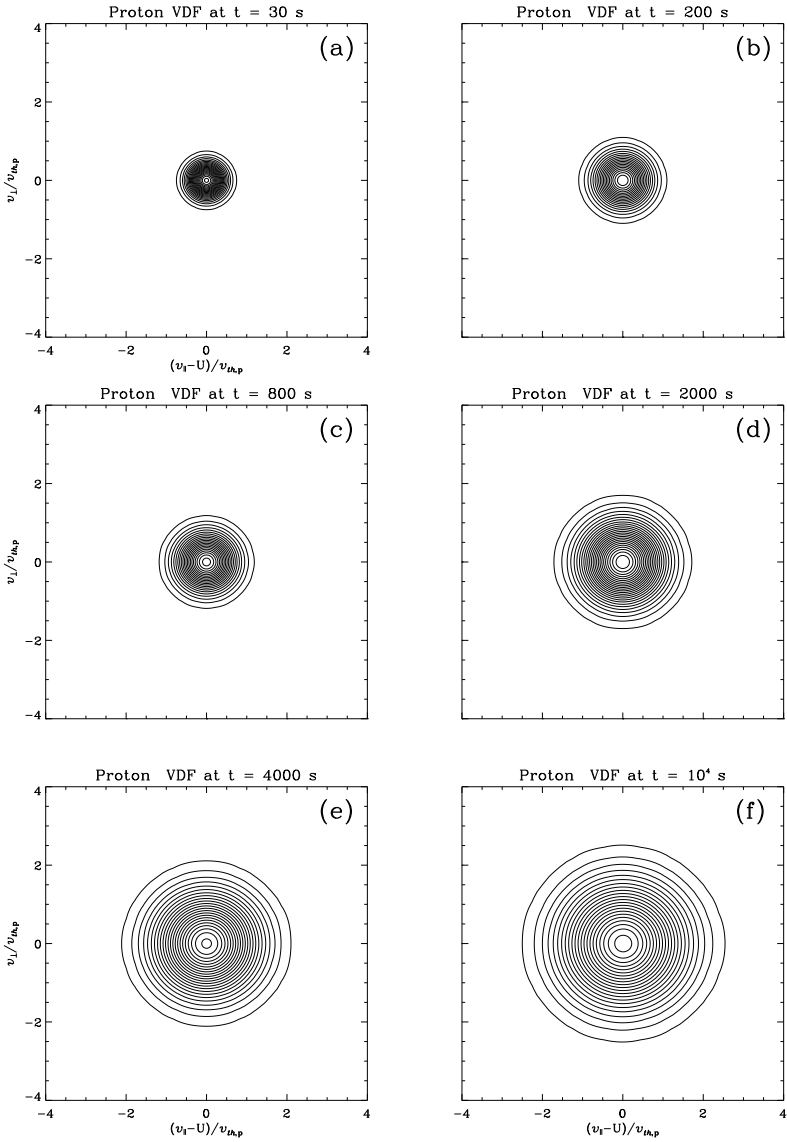


Figure 5.3: Time evolution of proton VDFs at position 16 Mm along the loop for $\Gamma = 1.48$. $v_{th,p}$ is the proton thermal speed at $s = 0$, and U the drift speed.

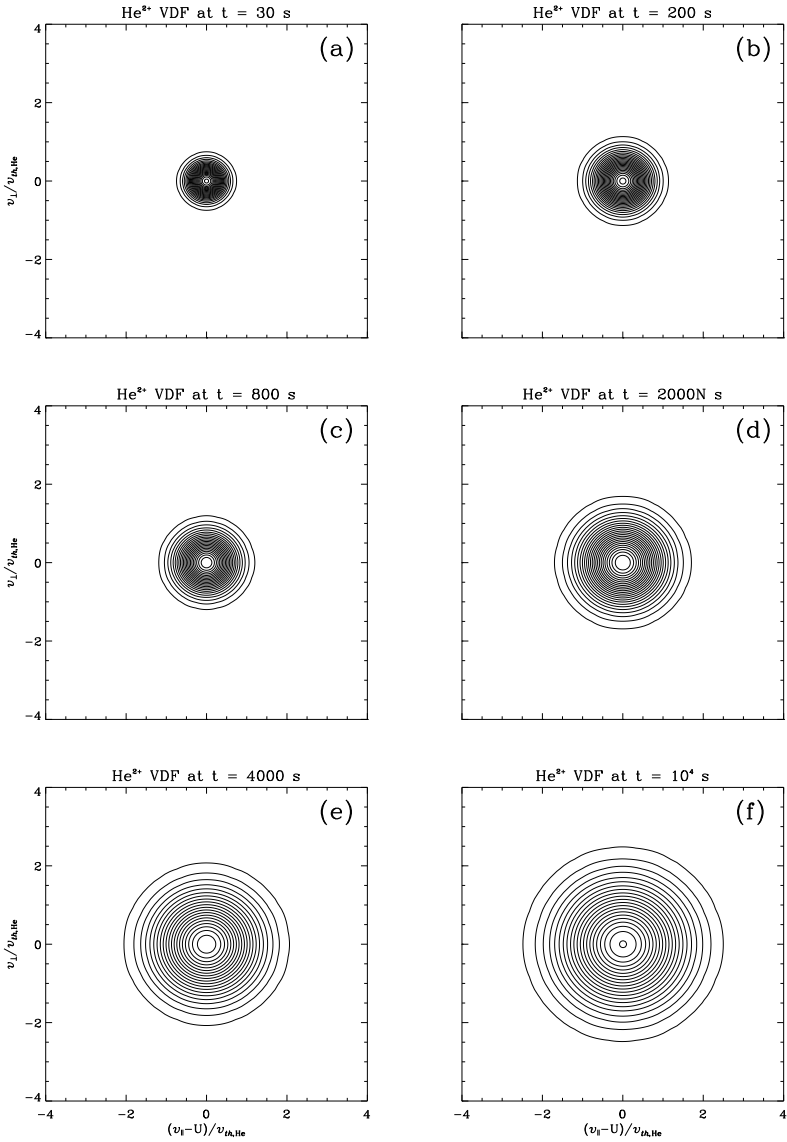


Figure 5.4: Time evolution of Helium VDFs at position 16 Mm along the loop for $\Gamma = 1.48$. $v_{th,He}$ is the helium thermal speed at $s = 0$.

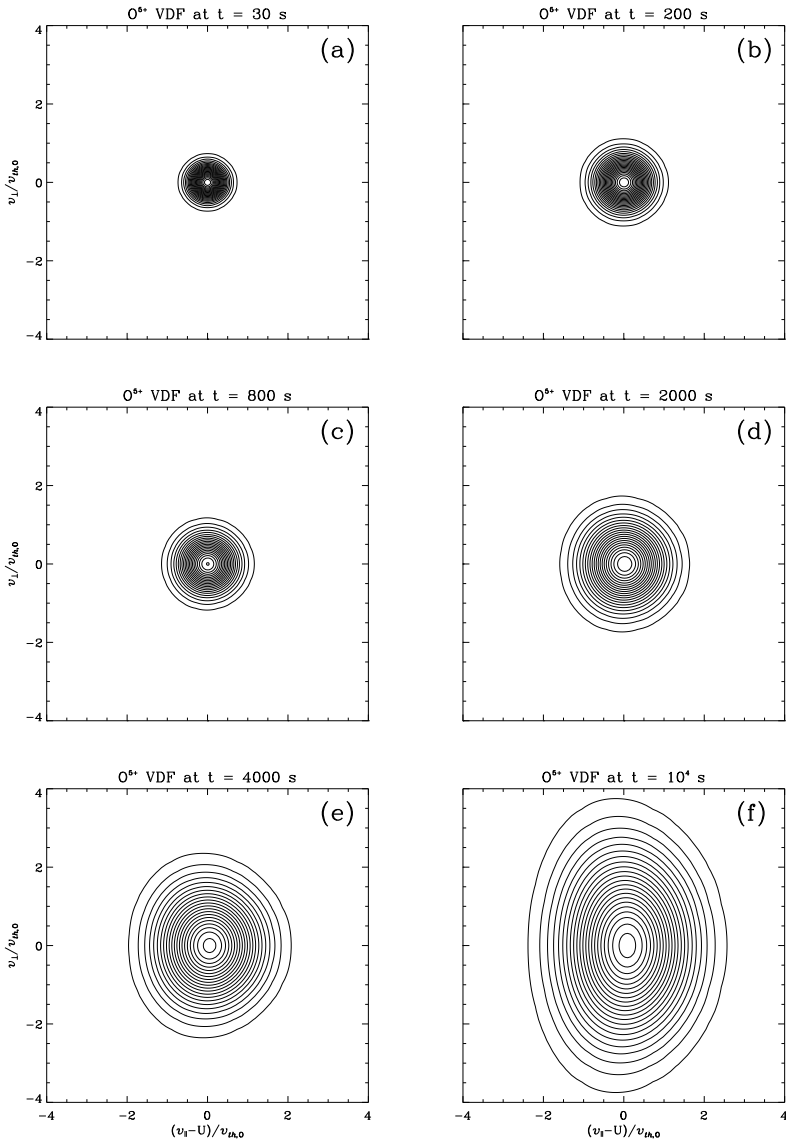


Figure 5.5: Time evolution of oxygen VDFs at position 16 Mm along the loop for $\Gamma = 1.48$. $v_{th,p}$ is the oxygen thermal speed at $s = 0$.

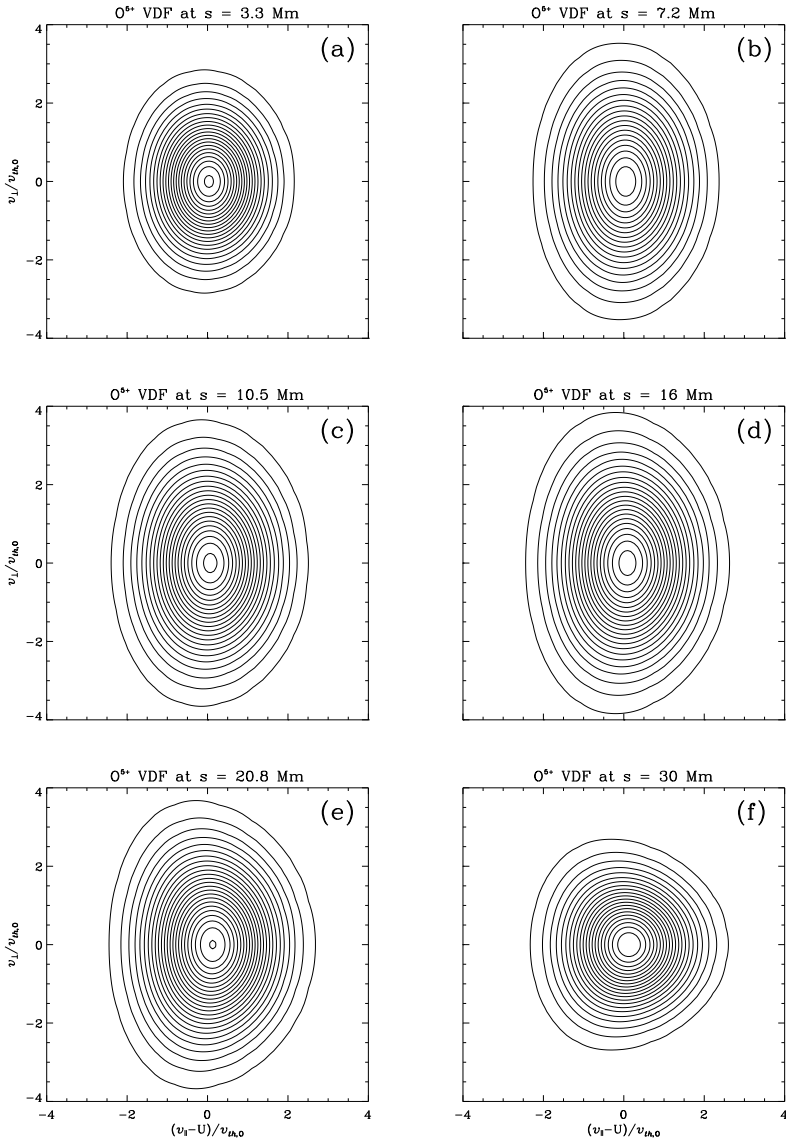


Figure 5.6: Steady final VDFs of oxygen plotted for several positions along the loop for $\Gamma = 1.48$.

6 Multi-strand loop modeling and filter-ratio analysis

6.1 Introduction:

In Chap. 4 we modeled a coronal loop as one single flux tube (or monolithic loop) in which the confined plasma is heated by ion-cyclotron/Alfvén waves via the resonant absorption mechanism. It turned out from this model that the warm loop has the roughly constant temperature profile and enhanced density (relative to static model Serio et al. 1981) is a consequence of uniform cross-section of the flux tube along the loop. Producing this type of loop profile with uniform temperature was motivated by many recent observations of EUV loop emissions (using high spatial resolution imaging provided by TRACE; see Lenz et al. 1999, Aschwanden et al. 1999, 2000a). Under the assumption that the loops have a single cross-field temperature, the TRACE 195:171 filter ratio implies that these loops have temperatures of 1-1.5 MK which are constant along much of their lengths. Furthermore, it was found that the densities of these warm loops are much more enhanced than the densities predicted by static models with uniform heating (see e.g., Aschwanden et al. 2001, Winebarger et al. 2003a). However, it was concluded that static loop models with footpoint heating may produce flat temperature profiles and enhanced apex densities, but the enhancement in density was found to be not large enough in case of long loops.

It is believed that the difficulty of reproducing the observed properties of TRACE loops with static models is that they are not in equilibrium. Therefore, it was suggested that the impulsive heating caused by nanoflare events could explain these observed loop properties. In this mechanism, the coronal loops are first strongly heated by a burst of thermal energy released when the reconnection occurs. Then the heating is followed by a strong evaporation of chromospheric material into the coronal loops. During the cooling phase, and when loop temperatures span between 1 and 1.5 MK, the loops can be denser than in the equilibrium case (see e.g., Warren et al. 2002, Cargill and Klimchuk 1997).

However, hydrodynamics simulations showed that the cooling loop would appear simultaneously in both TRACE 171 and 195 Å filters for only about 800 s (see e.g., Reeves and Warren 2002). This cooling time is much smaller than the lifetime of the observed TRACE active region loops which generally live for several hours, while maintaining their interesting features of high densities and flat temperature profiles. Therefore, the scenario of a temporal evolution of the loop cooling in time seems inconsistent with the observations.

It was shown that the existence of nanoflare heating models relies heavily on the as-

sumption of a multi-strand or multi-thread loop concept. In this concept, the observed coronal loops are composed of myriads of unresolved loop strands, and thus should exhibit a broad differential measure (DEM) distribution. This concept is recently endowed by many observations exploiting the high spatial resolution of TRACE, and indicating that the observed "fat" single loop could be composed of many small-scale filaments which most probably have different temperatures across the field (Schmelz et al. 2001, 2003, 2005, Martens et al. 2002). The lack of the observation of very fine scale structures beyond TRACE resolution leads to a possibility that the observed loops may be composed of very thin "strands or threads" that have different temperature and density profiles. Therefore, the loop intensity could represent an ensemble of emissions of many unresolved strands.

Adopting this concept of multi-strand loops, Reeves and Warren (2002) have produced the features of the observed warm loops by assuming a bundle of static, uniformly heated strands. Their model, however, implements dense and hot strand (~ 5 MK) to reproduce the flat TRACE filter ratios. This seems to contradict previous observations which indicate that, generally, hot loops are not cospatial with relatively cool loops (e.g., Sheeley 1980, Habbal et al. 1985). Recently, Warren et al. (2002) also suggested a multi-strand loop model where the strands are at random stages of impulsive heating and cooling. The authors synthesized the TRACE 171 and 195 Å intensities of the modeled strands, and obtained a flat 171:195 filter ratio along the loop resulting in larger emissions relative to those estimated by static heating.

Following the concept of a multi-strand structure of coronal loops, we now will also model the observed TRACE loop as a bundle of seven isolated strands. However, concerning loop heating we propose here that the strands are heated through the dissipation of parallel propagating ion-cyclotron/Alfvén waves via resonant wave absorption. The same kinetic model used in Chap. 4 to describe the heating of a monolithic loop now is applied to the heating of an individual small-scale strand. Thus various fine structures can have different temperatures and density profiles. Therefore, an observation of a neighbouring set of filaments with a low-resolution instrument could lead to an apparently fat loop, which yet is simply composed of a finite number of strands. Since in the corona the cross-field heat transport is very weak, and as the plasma is dominated by the magnetic pressure, we can assume that separate loop strands are thermally isolated.

Once we have determined the different plasma profiles of single loop strands, we can synthesize the total emission of the composite model loop, thereby assuming its observation as a monolithic loop in the TRACE/EIT filters, and thus we can extract its temperature by adopting the filter-ratio technique. We will show that in any case, when the coronal loop is composed of unresolved filaments having different temperatures and roughly identical emission measures across the coronal loop, a quasi-uniform temperature can be inferred along the loop length.

The chapter is organized as follows: in Sec. 6.2 we model a TRACE/EIT coronal loop as a bundle of seven separate filaments heated through the dissipation of high-frequency Alfvén waves. We assume different wave energy inputs at the footpoints of the different strand. Then in Sec. 6.3, we synthesize the emission of the modeled coronal loop in the three TRACE passbands, and thus we can derive the loop temperature from two filter ratios 171:195 and 171:284. Finally, we discuss the obtained results and conclude in Sec. 6.4.

6.2 Multi-strand coronal loop model:

It is believed that the small-scale reconnection events which occur in the lower corona (or chromosphere) can be an ultimate source of high-frequency waves, namely waves having scales comparable to the ion inertial length (also called ion-cyclotron waves) (see Axford et al. 1999, Axford and McKenzie 1995). Many theoretical works showed that the propagation of such waves in the corona may lead to an efficient ion heating, and can thus explain the rapid temperature increase in the transition region and corona (see, e.g., Vocks 2002, Vocks and Marsch 2002). Therefore, we also believe that the formation of coronal loops can be a consequence of the dissipation of ion-cyclotron waves along the closed magnetic field lines that confine the plasmas of these coronal loops (Bourouaine et al. 2008a,b). Furthermore, intuitively we think that the random spatial occurrence of the reconnection events may generate ion-cyclotron waves with different amounts of energy. The dissipation of these waves along the closed field lines leads to heating and plasma evaporation, thus producing a kind of small-scale filaments or strands (very fine loops beyond the TRACE resolution). These filaments may have differential temperature and density profiles. Therefore, the observation of these sets of filaments with low-resolution instruments shows fat loops that are simply composed of a finite number of these strands. Since in the coronal medium the cross-field heat transport is very weak, and as the plasma is dominated by the magnetic pressure, all the loop strands are thermally and dynamically isolated.

In this model, we will represent a coronal loop as an ensemble of seven separated loop strands or filaments (see Fig. 6.1). Each strand is modeled as an electron-proton plasma confined within a semi-circular cylindric and symmetric flux tube. All the strands (numbered by index i) are assumed to have the same length ($L = 63$ Mm) and the same local width, $w_i(s)$. We suggest that these strands are close to each other and situated in planes that are perpendicular to the solar surface. The flux tubes of these strands expand similarly with height, i.e., the filaments have the same expansion factor, $\Gamma = 1.48$. This means that each strand has a varying cross-section which expands from the strand footpoints (situated at the transition region) to the strand top and satisfies formula (4.1).

The loop strands are heated through the dissipation of nondispersive Alfvén/ion-cyclotron waves propagating along the field lines. These waves are assumed to be injected at the left footpoints of the strands and heat the ions via resonant wave-particle interactions. More details about this dissipation mechanism are given in Chap. 4 in case of monolithic coronal loop modeling. Here, for each strand, a power-law spectrum is assumed for the Alfvén waves at the left strand-footpoint, i.e.,

$$\mathfrak{B}_\omega^i(s=0) = \alpha_i \left[\omega \ln(\Gamma^2) \right]^{-1} \text{J m}^{-3} \text{s}^{-1}, \quad i = 1, 2..7 \quad (6.1)$$

where \mathfrak{B}_ω^i is the wave spectral energy density of the waves entering the strand. The parameter α_i which corresponds to each loop strand is listed in Tab. 6.1

All the loop strands have the same boundary conditions, i.e., their electron densities at the footpoints ($s = 0, s = L$) are given by $N_e(s = 0) = N_e(s = L) = 5 \times 10^{15} \text{ m}^{-3}$, and their electron temperatures by $T(s = 0) = T(s = L) = 2 \times 10^5 \text{ K}$. Also, at $t = 0$ (the initial condition) we consider a similar initial state for all the strands, i.e., the strands are cooler and have relatively small apex densities. After about ten thousands of seconds

Table 6.1: The parameter α_i corresponds to strand "i" defined by its maximum proton temperature shown in Fig. 1a

Strand	T_{Max} (MK)	$\alpha_i \times 10^4$
1	0.7	0.5
2	0.84	0.7
3	1.2	1.1
4	1.4	1.4
5	1.66	1.9
6	1.95	2.5
7	2.1	3.0

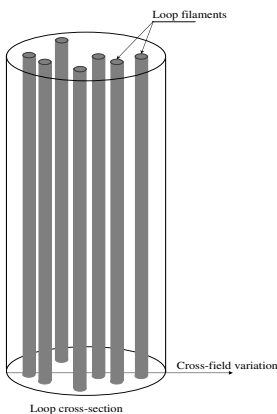


Figure 6.1: Coronal loop that consists of many small-scale filaments

all the strands reach their steady final states, and they get filled with plasma due to the evaporation process and particle acceleration and thus form an unresolved TRACE or SOHO/EIT loop.

The temperature and density profiles of the species of each strand are plotted in Fig. 6.2. As expected, the higher the wave energy input the more energy is transferred to the plasma loop strand. The Alfvén waves heat the protons via ion-cyclotron-wave absorption, and thus due to proton-electron collisions also the electrons can be heated. The proton temperatures increase up to their maximum values close to a distance of ≈ 20 Mm where the dissipation of the waves ceases. The proton temperatures tend to decrease under the effect of heat conduction and electron-proton energy exchange by collisions.

However, the electron temperature is roughly equal to the proton temperature as long as the latter is smaller than one mega kelvin. But when the proton temperature exceeds this value, the electron temperature remains at smaller values due to strong electron heat conduction. Therefore, the electron and proton temperatures in the strands "1, 2" roughly overlap. While, in the case of strands "3, 4, 5, 6, 7", the protons are hotter than the electrons, and electrons show a quasi-uniform heating.

In this kinetic model, the loop strands can be filled with plasma via two mechanisms, wave-induced particle acceleration and chromospheric plasma evaporation (caused by heat conduction from the corona). However, wave-particle acceleration is the dominant process to fill the loop-like structures with protons, since the proton heat conduction is small, and the electron inertia is neglected in our approximation. Thus, the plasma dynamics of the loop is only related to the proton inertia. As a result, we see that the densities in big parts of the loop strands do not differ by much. Consequently, the strands have a roughly similar emission measure ($EM = N^2w$) across the loop.

Therefore, the modeled coronal loop (represented by a multi-stranded coronal loop) has a varying cross-field electron temperature, which spans between 0.6 to 1.6 MK at its top (and between 0.6 to 2 MK), but only a small cross-field density variation (or slight cross-field emission-measure variation). The next section is devoted to the analysis of the emission of the modeled coronal loop, as it would be observed in the three EUV channels at 171, 195 and 284 Å available in the TRACE imager or SOHO/EIT.

6.3 Filter-ratio analysis:

In the following section we introduce the term "isothermal temperature", T_{iso} , which simply means the observationally inferred loop temperature when assuming a single cross-field temperature and using filter-ratio technique.

It is possible to synthesize the total emission of the modeled fat loop from the seven strand emissions. The emission of each strand can easily be computed from its modeled density and temperature profiles using the following emission measure relation

$$\zeta_i(s) = N_i^2(s)G(T_i^{eff}(s)), \quad i = 1, 2..7 \quad (6.2)$$

where $\zeta_i(s) = I_i(s)/w_i(s)$ (the intensity over the width) is the emission of the strand "i" given per unit optical length (units of DN s⁻¹ pixel⁻¹ cm⁻¹) at position s along the strand (or is the intensity over the width). T_i and N_i are respectively, its effective temperature (units of Kelvin) and density (units cm⁻³). $G(T)$ is the response function given for each filter as plotted in Fig. 6.3a.

Now we study the emission of the loop strands considering, first the proton temperature to be an effective temperature ($T^{eff} = T_p$) of the emissions. Then, in the second case $T^{eff} = T_e$, where T_e is the electron temperature.

The strand emissions in the three filters are plotted in Fig. 6.4 in the case of $T^{eff} = T_p$. It seems that the strands brightest in the 171 Å emission are those labeled with numbers 3, 2, 4, and 1 (ordered from the highest to lowest intensity). However, in this filter, the remaining strands are less visible due to their relatively high temperatures which exceed 1.1 MK. Therefore, the first fourth strands mainly contribute to the total emission $\zeta_{tot}(s)$ of the total loop in the 171 Å passbands (see Fig. 6.4d). Moreover, Fig. 6.4b shows that

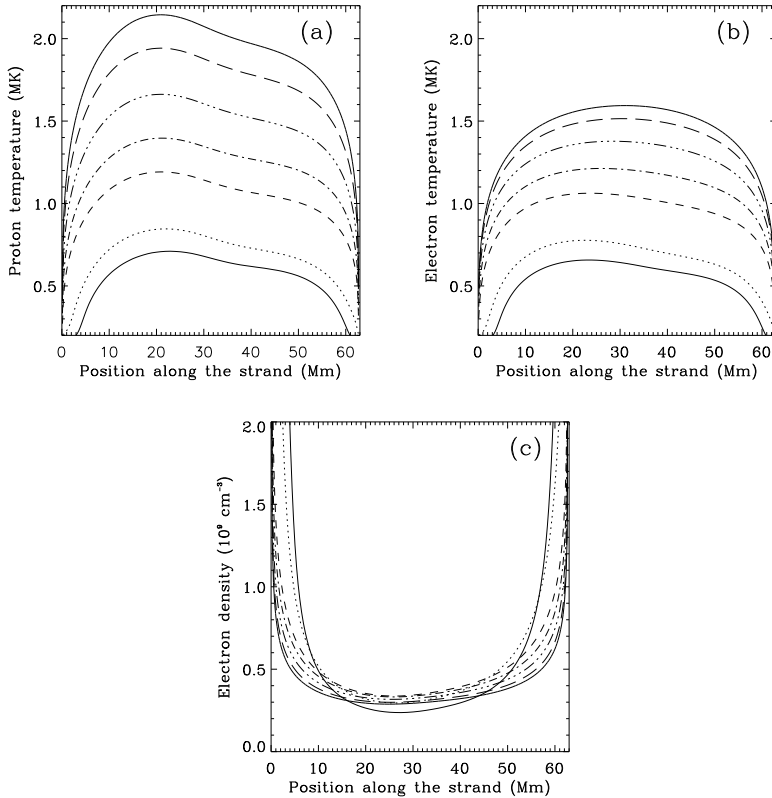


Figure 6.2: Plasma profile for each loop strands, (a): Proton temperature, (b) electron temperature and (c) electron density. All parameters are plotted as function of strand position such that (solid line) refer to strand "1", (dotted line) strand "2", (dashed line) strand "3", (dash-dotted line) strand "4", (dash-triple dotted line) strand "5", (long dashed line) strand "6" and (thick solid line) strand "7".

the 195 \AA filter is more sensitive to the strands labeled with number 4, 5 and 3 (from the highest to lowest intensity). This is because the maximum temperatures of these strands range between 1 and 1.4 MK which is the temperature interval of the response of the filter in the 195 \AA passbands. Overall, these mentioned strands mostly dominate the emission of the total loop in the 195 \AA passbands shown in Fig. 6.4d.

It turns out from Fig. 6.4c that the modeled fat loop is less visible in the 284 \AA emission. This is because this filter is more sensitive to hot loops (having temperatures higher

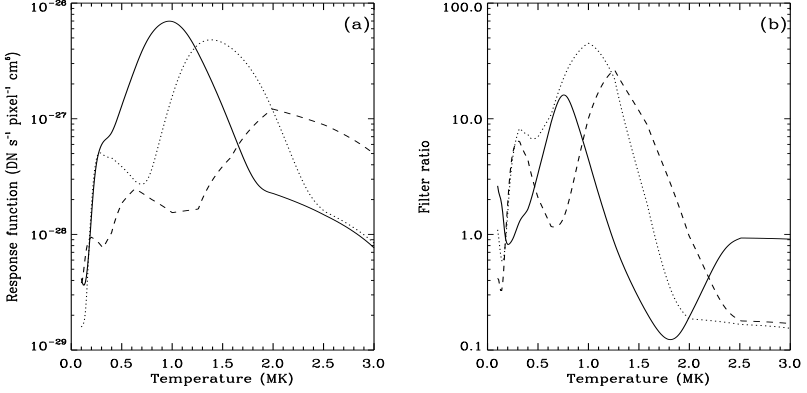


Figure 6.3: (a): The response function for each TRACE filter; filter with 171 Å passbands (solid line), filter with 195 Å passbands (dotted line) and filter with 284 Å passbands (dashed line). (b): The ratio between two filters; (171:195) (solid line), (171:284) (dotted line) and (195:284) (dashed line).

than 2 MK). Only hotter strands having apex temperature $\gtrsim 1.3$ MK can slightly be visible in this passbands, therefore, the whole "fat" loop appears at lower intensity which is smaller by about one order of magnitude than its emission in the filter with the 171 Å wavelength (Fig. 6.4d). Furthermore, in the more realistic case when the background has to be accounted for, this modeled loop can hardly be seen in the 284 Å passbands, since its emission would strongly be contaminated by the background effect.

When we consider the electron temperature as an effective temperature for the loop strand emissions which are shown in Fig. 6.6, the total loop will be more visible in the 171 Å filter. According to the Fig. 6.6a, all the strands, except of the strand "7", contribute in the total emission of the loop in the filter 171 Å. Also the loop would be more visible in the 195 Å filter, since the cross-field electron temperature ranges between 0.5 and 1.6 MK. However, less visibility of the loop is expected in the filter 284 Å. Therefore, in both cases of the effective temperature consideration, the total coronal loop is more visible in the two filters with 171 and 195 Å. We can then classify our modeled multi-strand loop as warm EUV loop in terms of visibility in TRACE filters.

In Fig. 6.5 and Fig. 6.7 the different emission ratios for each strand are computed for both cases of the effective temperature. Generally, it seems that the strands have varying filter ratios, which implies a varying temperature along their lengths. Now, by making use of the total-emission ratio of the fat coronal loop, 171:195 and 171:284, we can extract the assumed single cross-field temperature (also called isothermal temperature) by assuming that the total emission is given by

$$\zeta(s) = N^2 G(T_{iso}), \quad (6.3)$$

where N is the assumed single cross-field density.

Fig. 6.5c and Fig. 6.7c display the ratio between the different the total loop emissions plotted versus the loop length. Interestingly, for both cases of the effective temperature, the total-emission ratio (171:195) (indicated by solid line) varies slightly between two values, 1 and 3 inside the loop. However, the total-emission ratio (171:284) (indicated by dot lines) spans between the values 10 and 12 when $T^{eff} = T_e$, and between the values 8 and 10 in the case of $T^{eff} = T_p$. As we will show, these variations in the different filter-ratios are still not large enough to produce varying temperatures along the loop.

Based on the obtained results of the total-intensity ratios, and by making use of the ratios between the response functions plotted in Fig. 6.3b, we can extract the isothermal temperature that corresponds to each filter ratio. Here, we deal with two filter ratios, 171:195 and 171:284 since they provide unique values of T_{iso} unlike the filter 195:284 that may not provide a unique T_{iso} . For example the value 4 in the filter ratio 195:284 corresponds to two possible isothermal temperatures when assuming the temperature ranges between 0.6 and 2 MK (see Fig. 6.3b). Figs. 6.8a, 6.9a show different isothermal temperatures obtained from the two filter ratios. This result gives a good indication that we are dealing with an unresolved multithermal loop which contradicts the isothermality assumption across the field.

Interestingly, the obtained isothermal temperatures are quasi-uniform along the loop length for both cases of effective temperatures. Moreover, the obtained T_{iso} from the intensity ratio 171:195 is more uniform along the loop length when we consider $T^{eff} = T_p$. This seems to fit the TRACE coronal loop features (see e.g., Lenz et al. 1999) as discussed in the introduction. Most of the observed warm EUV loops cannot clearly appear in the filter (284 Å) because their emissions can strongly be affected by the background emission. Thus, one may think that these loops are isothermal across their field lines when only using the filter ratio (171:195). But in fact when we consider their emission in the 284 Å filter, the temperatures obtained from two different filter-ratios may not overlap. Therefore, the use of multiple filters is inevitably needed to determine whether the isothermality assumption across the field is correct or not. This conclusion may explain the recent results obtained by Schmelz et al. (2003). The authors analysed 10 coronal loops that were clearly visible in the 171, 195 and 284 Å passbands of the EIT. They showed that in each case of the used background subtraction method two different uniform temperatures were obtained, one from the 171:195 ratio and the second for the 195:284 ratio. The authors suggested that the single cross-field temperature assumption could provide a misleading loop temperature.

However, we argue here that, in case of warm loops ($T \leq 1.5$ MK), it is difficult to infer the temperature from the filter ratio 195:284. This is because the ratio function 195:284 in Fig. 6.3b peaks at a temperature $T \sim 1.26$ MK, and for any ratio value that spans between ~ 1 and ~ 26 , there are two corresponding temperatures; one is above 1.26 MK and the other below it (non-unique solution). Therefore, in the case of warm coronal loops, it is difficult to constrain the temperature value to be chosen. For that reason, we did not use here the filter ratio 195:284 to determine the loop temperature.

By assuming a line-of-sight depth of 10^{10} cm, as considered by Lenz et al. (1999), we estimate the emission measure from the filter ratio (171:195) and (171:284) (see Fig 6.8-6.9). The emission measure profile implies an enhanced density inside the loop, and the estimated EM for the first filter ratio is comparable to the one obtained by Lenz et al.

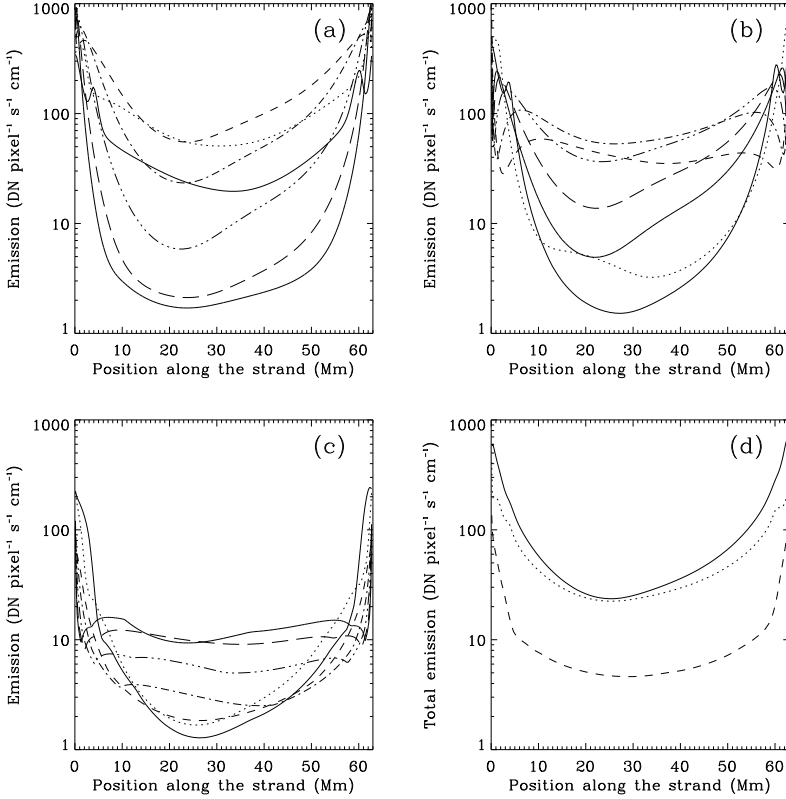


Figure 6.4: Here $T^{eff} = T_p$. (a): Emission of each strand through the filter (171 Å). (b): Emission of each strand through the filter (195 Å). (c): Emission of each strand through the filter (284 Å). All plotted as function of the strand position. Each strand is represented by the same type of line as given in Fig. 6.1. (d): Total loop emission through the filters (171 Å) (solid line), (195 Å) (dot line) and (284 Å) dashed line.

(1999), however, a higher EM could be obtained if we considered the filter ratio (171:284).

Notice that the obtained isothermal temperatures in our model have nothing to do with the computed average temperatures as shown in Fig. 6.8a and Fig. 6.9a. The average temperatures, in both cases of effective temperatures, vary along the loop and do not show any flat profiles.

The question is, why often flat temperature profiles are obtained when using the filter-ratio technique? Weber et al. (2005) suggested that the flatness of the temperature profile

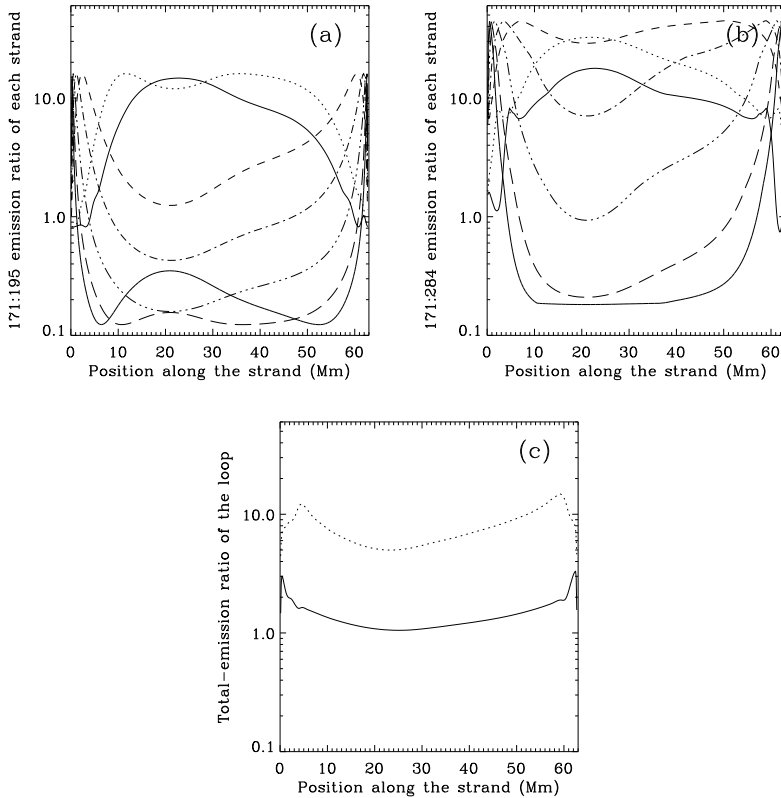


Figure 6.5: Here $T^{eff} = T_p$. Emission ratios 171:195 (a), 171:284 (b), plotted for each strand represented by the same type of line as given in Fig. 6.1. (c): Loop-emission ratio of the loop, (171:195) (solid line) and (171:284) (dot line).

is due to a varying cross-field temperature (broad differential emission measure (DEM)) in loop, such that the emission ratio method is biased toward the ratio of the integrated response functions over a broad temperature interval. The authors concluded that this ratio is about 0.81, which correspond to the TRACE temperature of ~ 1.2 MK. A TRACE-loop temperature around this value is interpreted to be consistent with multi-thermal plasma, and therefore with results obtained with the Coronal Diagnostic Spectrometer (CDS).

However, here we argue that the flat temperature profile can even occur in the case when the loop consists of a finite number of strands (forming a real discrete loop structure), and if these strands have roughly a similar EM_i but different temperatures across

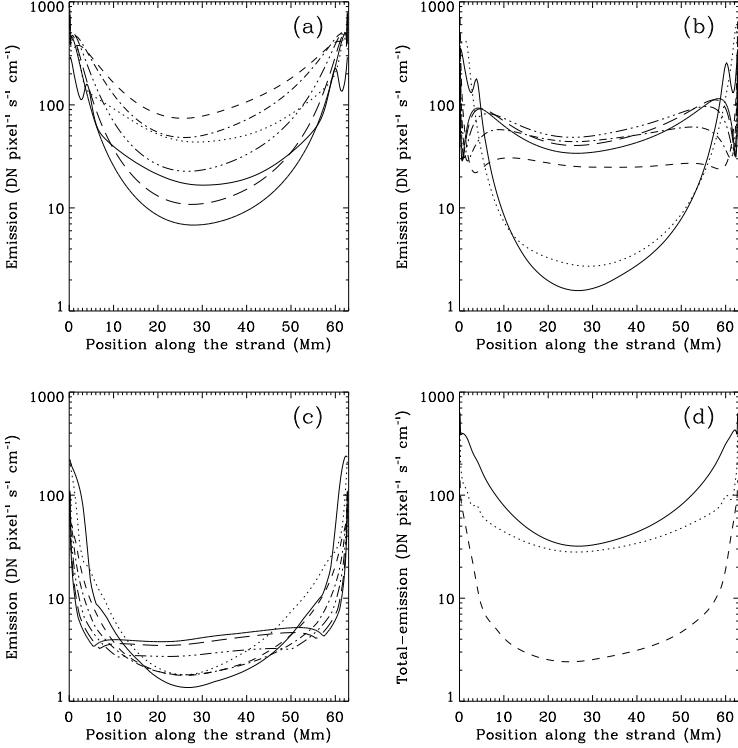


Figure 6.6: Here $T^{eff} = T_e$. (a): Emission of each strand through the filter (171 Å). (b): Emission of each strand through the filter (195 Å). (c): Emission of each strand through the filter (284 Å). All plotted as function of the strand position. Each strand is represented by the same type of line as given in Fig. 6.1. (d): Total loop emission through the filters (171 Å) (solid line), (195 Å) (dot line) and (284 Å) dashed line.

the loop (as in the case of our modeled coronal loop). Consequently, the overall loop intensity ratios, at a given loop position, simply would reduce to the ratios of the response functions summed over the number of the loop strands within this coronal loop position, i.e., to the ratios

$$R_1 = \frac{\sum_{i=1}^{N_s} G^{171}(T_i)}{\sum_{i=1}^{N_s} G^{195}(T_i)}, \quad (6.4)$$

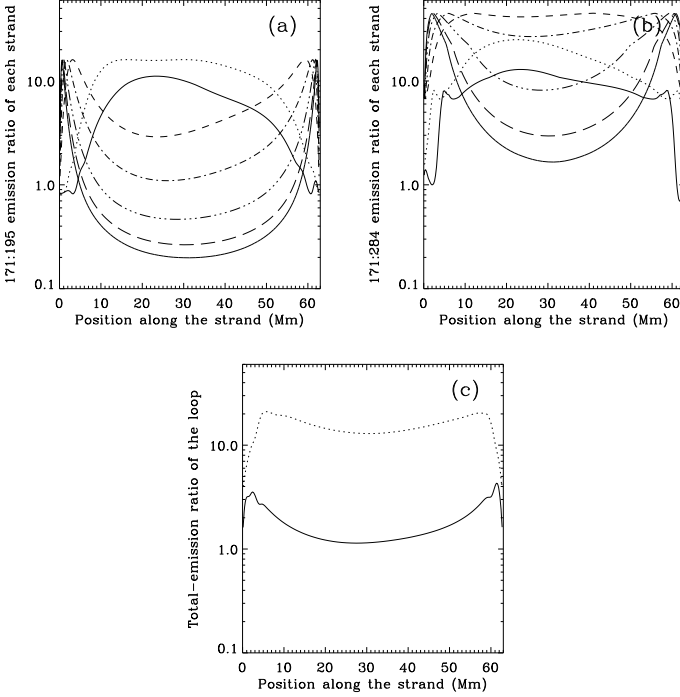


Figure 6.7: Here $T^{eff} = T_e$. Emission ratios 171:195 (a), 171:284 (b), plotted for each strand represented by the same type of line as given in Fig. 6.1. (c): Total-emission ratio of the loop, (171:195) (solid line) and (171:284) (dot line).

$$R_2 = \frac{\sum_{i=1}^{N_s} G^{171}(T_i)}{\sum_{i=1}^{N_s} G^{284}(T_i)}, \quad (6.5)$$

where, N_s is the total number of the loop strands. Now by assuming a number of strands, N_s , and making use of eqs. (6.4) and (6.5) we can infer the coronal loop temperature. The strands are assumed to have temperatures equally distributed over the interval $[T_{min}, T_{max}]$. In Fig. 6.10 and Fig. 6.11, we plot the temperature contour plots for some values of N_s and varying interval $[T_{min}, T_{max}]$.

Overall, in case of the filter ratio R_1 when $0.5 \leq T_{min} \leq 1$ MK, Fig. 6.10 shows that the obtained temperatures are generally ranging between 0.9 and ~ 1.25 MK for all of the proposed number of the strands, N_s . For a fixed value of T_{max} below 1.5 MK (as in the case of warm coronal loops) the inferred temperature hardly depends on the varying T_{min} for all N_s . This may explain the flat temperature profile often observed in TRACE and

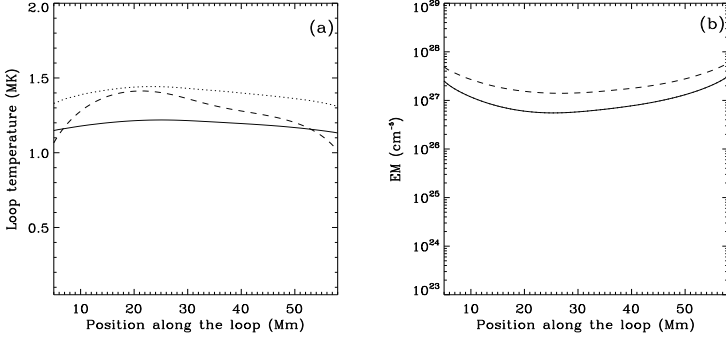


Figure 6.8: (a) and (b): Loop temperatures and loop emissions plotted when $T^{eff} = T_p$. (a): Isothermal temperature, T_{iso1} that corresponds to the filter ratio (171:195) (solid line), T_{iso2} that corresponds to the filter ratio (171:284) (dot line) and the average temperature (dash line). (b): Emission measures correspond to filter-ratio (171:195) (solid line), filter-ratio (171:284) (dash line).

EIT warm loops when using the filter ratio 171:195.

Also, in the case of the filter ratio R_2 , when $0.5 \leq T_{min} \leq 1$ MK, the results of Fig. 6.11 show that the obtained temperatures are ranging between 1.0 MK and 1.4 MK for all N_s . For a given values of $T_{max} \gtrsim 1.4$ MK, the inferred temperatures hardly vary with respect to T_{min} for all N_s .

In general, the values of the temperature obtained from R_2 do not coincide with those obtained from R_1 for the same coordinates (T_{min}, T_{max}). However in the case of warm loops, if the temperature uncertainty is accounted for, the two temperatures may overlap. Therefore, we expect that the use of the triple TRACE/EIT filters may not help in answering if a loop is isothermal or multi-thermal.

Finally, we may say that the flatness in temperature profile often obtained in warm EUV loops using TRACE/EIT filters can be produced by a simulated coronal loop that consists of a small or large number of filaments (having scales below the TRACE resolution) that have different temperatures and roughly similar emission measures across the loop. Therefore, one would expect that only when the multi-thermal coronal loops have strong cross-field EM gradients, the flat temperature profile may not occur.

One of the consequences of our conclusion is that, in the transversal direction of the coronal loop, the widths of the loop strands that compose this coronal loop are inversely proportional to the square of their densities, $w_i \propto 1/N_i^2$, since their EM_i are equivalent. If we assume that the electron temperature is inversely proportional to the density therefore when the loop strand is hot, one expect that its width is larger comparing with cooler loop strands. This means that the coronal loops appear wider in the hot emission lines than in the cooler ones, since the hot strands that contribute to the hot emission are wider. This may explain the fuzziness in the loops when observed in hot emission lines.

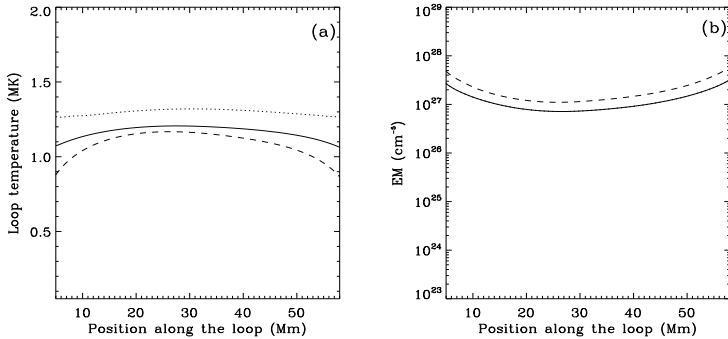


Figure 6.9: (a) and (b): Loop temperatures and loop emissions plotted when $T^{eff} = T_e$. (a): Isothermal temperature, T_{iso1} that corresponds to the filter ratio (171:195) (solid line), T_{iso2} that corresponds to the filter ratio (171:284) (dot line) and the average temperature (dash line). (b): Emission measures correspond to filter-ratio (171:195) (solid line), filter-ratio (171:284) (dash line).

6.4 Conclusion

In this work we synthesized the emission of seven strands which together are assumed to constitute a coronal loop as seen in a low-resolution TRACE or SOHO/EIT observation. Each of the loop strands used in the model is heated by Alfvén/ion-cyclotron waves via wave-particle interactions. This process leads to proton heating in the electron-proton plasma, and due to electron-proton collisions the electrons can then be heated as well up to a certain temperature which is below or equal to the proton temperature. It turns out that the plasma, in case of hot loop strands (where the proton temperature exceeds > 1 MK) is not in local thermal equilibrium and the electrons are cooler than the protons.

In our model, the Alfvén waves, which are assumed to penetrate the strands from their footpoints, are there generated with different intensity. Consequently, different heating profiles occur within each strand due to the wave absorption or heating process. Therefore, this differential heating leads to a varying cross-field temperature in the total coronal loop. The simulated TRACE/SXT observation of this model loop implies two different quasi-uniform temperature profiles along the loop length, one derived from the filter-ratio 171:195 and the other for the 171:284. The flatness in the derived temperature profiles is due to the property of a roughly constant EM of the loop strands in the cross-field loop direction.

Furthermore, for different cases of loop strands with different temperatures and the same EM, we showed that the loop temperatures inferred from both filter ratios (171:195 and 171:284) span a narrow interval. In the case of the filter-ratio R_1 , the obtained loop temperatures range between ~ 1 and 1.2 MK, and for R_2 the temperature spans between 1 and 1.4 MK.

Here we claim that the uniform loop temperature ~ 1.3 MK as obtained from 171:195

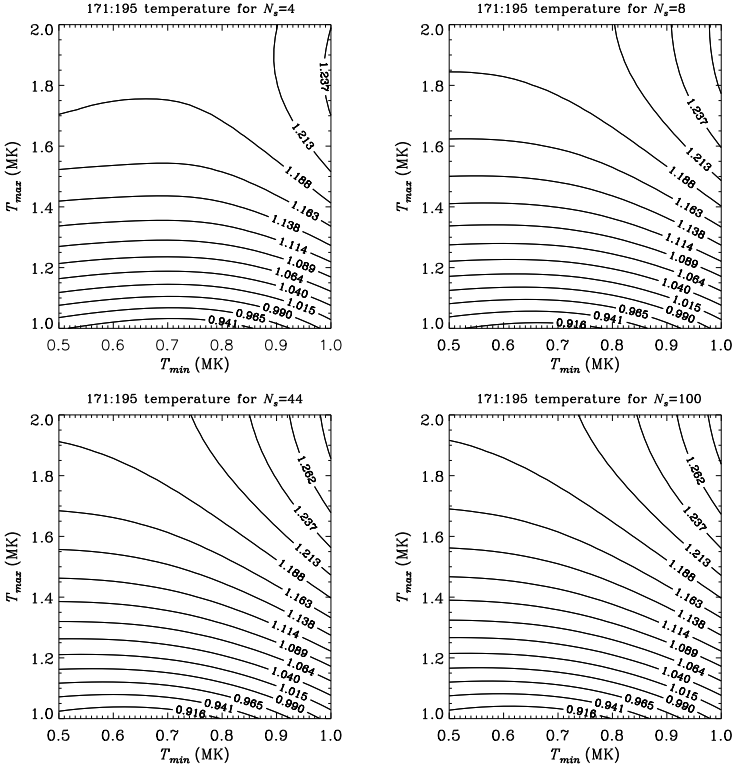


Figure 6.10: Isothermal temperature obtained from the filter ratio R_1 for some indicated values of N_s .

ratio for the observed TRACE loop studied by Lenz et al. (1999) cannot be produced from the multi-thermal loop assumption for a warm loop (with $T \lesssim 1.5$ MK) as proposed in our work. Except if this observed loop is classified as a hot loop (if it is quite visible in the 284 filter), then it would be possible if the minimum temperature of the strands obey: $T_{\min} > 1.1$ MK and $T_{\max} > 1.5$ MK. Otherwise it is a warm loop, and we then need loop strands having temperatures that vary within a narrow interval (quasi-isothermal loop).

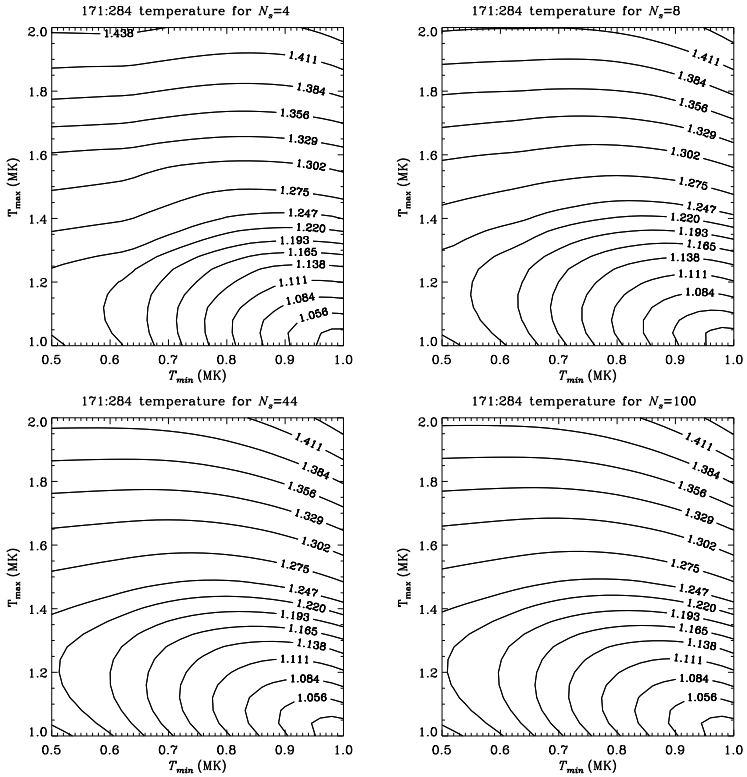


Figure 6.11: Isothermal temperature obtained from the filter ratio R_2 for some indicated values of N_s .

7 Conclusion and outlook

The linear dispersion of the fast waves in a magnetized, homogeneous and collisionless plasma (consisting of electrons and protons in thermal equilibrium) has been studied in chapter 1. It has been shown that the damping of the fast mode can be achieved via the first three harmonic proton-cyclotron resonances. By using the quasi-linear theory we studied the heating of the protons via the dissipation of the obliquely propagating fast waves through ion-cyclotron resonance, and we have shown that these waves can efficiently heat the protons perpendicularly to the direction of the mean magnetic field.

In chapter 2, the nonresonant wave-particle interactions are studied within the framework of quasi-linear theory for the reduced velocity distribution functions of coronal ions. It turned out that Alfvén waves at low-frequencies (with $\omega_k \ll \Omega_i$, where Ω_i is ion gyrofrequency) can heat ions perpendicularly to the direction of the mean magnetic field leading to a temperature anisotropy in collisionless plasma. This heating process is efficient in low-beta plasma, and the heavy ions are heated more strongly, by a factor of the mass ratio, than the protons. This mechanism may be responsible for the heating of the lower corona and the upper chromosphere where the magnetic pressure is expected to dominate the gas pressure. But at these lower coronal altitudes, such wave-induced features will be destroyed by the collisions that are still strong there. Furthermore, although the coronal plasma β is small at lower altitudes, Alfvén waves may efficiently heat the ions only if their energy is relatively large. When assuming a power law spectrum, the heuristic values of the wave energy needed for strong heating are, however, much larger than the ones assumed in previous models and obtained from recent observations. Nevertheless, heating of the ions by low-frequency Alfvén waves can contribute to raising the temperature of the lower solar transition region.

In Chapter 3, we modeled the heating of a coronal loop, consisting of electrons and protons, by using a semi-kinetic model. The model is based on the quasi-linear treatment of the Vlasov equation for the reduced velocity distribution functions of the protons. The collisions are included and they are described by the Fockker-Planck operator. The coronal loop is heated through the dissipation of linear Alfvén waves. These waves are assumed to be injected at the footpoints of the loop and heat the protons via wave-particle interactions and wave absorption. Since the electron density in the coronal loop is relatively higher than in coronal holes, the electrons can be heated via the energy exchange with protons due to the Coulomb collisions.

It turns out that in such a model protons are hotter than electrons, and the scale length for proton heating along the loop is determined by the dissipation scale of the ion-cyclotron waves. Through the gyrofrequency this scale is connected to the cross section area of the loop and, thus, to the spatial variation of the magnetic field shaping the coronal loop. Furthermore, it has been shown that footpoint-type heating with a small

scale height is a consequence of a quasi-homogeneous flux tube, in which the temperature profile remains nearly constant along the loop and the density is relatively higher than in the case of loops in hydrostatic equilibrium with uniform heating. These plasma features are consistent with those inferred from the TRACE loops that have temperatures ~ 1.2 MK (or called warm coronal loops).

However, if the magnetic field lines are more strongly diverging from the footpoints to the loop apex, the proton heating is found to be more uniform, resulting in a higher temperature and lower density along the loop. These profiles are similar to those observed in X-ray loops. In this situation, the proton temperature is higher (can exceed 2 MK), the collisions become then less efficient, and thus the electrons cannot be more heated and their thermal energy is strongly reduced due to heat conduction which is proportional to $T_e^{5/2}$ and to radiative losses especially at the footpoints.

By including other heavy ions in the plasma loop, we studied in chapter 5 the temperature anisotropy and the preferential ion heating. Also in this multi-ion kinetic model for a coronal loop, the ions in the magnetically confined plasma are heated by absorption of ion-cyclotron waves. The linear Alfvén/cyclotron waves which penetrate the loop from its footpoint can heat the ions, and the amount of the wave-energy transferred to each ion mainly depends of the loop expansion. Depending on the spatial variation of the mean magnetic field, the model is able to produce warm and hot model loops having features similar to the ones observed in extreme-ultraviolet and soft X-ray emissions in real coronal loops. Furthermore, it is found that a loop with high expansion factor is not in local thermal equilibrium (LTE) and shows remarkable temperature differences between electrons and ions. Also in such case, the heavy ions (minor ions) are, via resonant wave absorption, heated more than the protons and helium ions (major background ions), whereby the cyclotron-resonance effect leads to a temperature anisotropy with $T_{\perp} > T_{\parallel}$. However, if the flux tube cross section is nearly homogeneous, temperature isotropy of the ions is maintained in most parts of the loop, and the plasma is nearly in LTE. Unlike in coronal holes, the temperature anisotropy of the oxygen ions is very small in coronal loops. This is because the electron density in the coronal loop is higher than in the open coronal field. Therefore, the collisions in coronal holes are too weak to maintain an isotropic VDF (or Maxwellian).

Briefly, the semi-kinetic model can produce both types of observed coronal loops. The EUV loops can be modelled well if the cross-section area, corresponding to the magnetic field line density in the loop, is more homogeneous with $\Gamma \approx 1.04$. However, the X-ray loops observed with a quasi-uniform heating can arise in our model if the cross section expands, with $\Gamma \approx 1.48$.

When assuming that the observed coronal loops are composed of many strands or fine filaments having differential heating profiles, we may obtain a misleading coronal loop temperature by using the filter-ratio technique. In chapter 6 we considered a fat loop composed of seven strands or filaments. Each of the loop strands used in the model can independently be heated by Alfvén/ion-cyclotron waves via wave-particle interactions. These waves are suggested to enter the loop filaments with different energy inputs. Therefore, different heating profiles occur within each strand, and this differential heating leads to a varying cross-field temperature in the total coronal loop. It has been shown that the simulated TRACE/SXT observation of this model loop implies flat temperature profiles. The flatness in the temperature profiles often observed in TRACE/SXT coro-

nal loops can be a signature that these loops are multithermal and have small cross-field density variation.

As outlook, we plan to continue focusing on the role of the microphysics in the coronal heating. It is necessary to scale the results obtained from the semi-kinetic model and the wave-particle interactions. The scaling law of the ion-cyclotron heating process in the coronal loop could help to describe the heating by a simple function that could be included as heating source in the fluid equations. Furthermore, the scaling law of the heating rate has to address the connection between the expansion of the coronal loop and its heating profile. An other plan is to include the other modes e.g., fast and slow waves, in the wave-particle interactions.

Also, as another future work, we plan to study an other kinetic heating mechanism that relies on the dissipation of low-frequency waves via weak collisions. It seems that the collisions existing in the lower corona may strongly dissipate those electromagnetic fluctuations having wavelengths smaller than the MHD scales. This new heating mechanism can be relevant for the heating of the upper chromosphere and transition region.

Bibliography

- Acton, L., Tsuneta, S., Ogawara, Y., Bentley, R., Bruner, M., Canfield, R., Culhane, L., Doschek, G., Hiei, E., Hirayama, T., 1992, The YOHKOH mission for high-energy solar physics, *Science*, 258, 618–625
- Aschwanden, M. J., 2004, *Physics of the Solar Corona. An Introduction*, Physics of The Solar Corona
- Aschwanden, M. J., Newmark, J. S., Delaboudinière, J.-P., Neupert, W. M., Klimchuk, J. A., Gary, G. A., Portier-Fozzani, F., Zucker, A., 1999, Three-dimensional Stereoscopic Analysis of Solar Active Region Loops. I. SOHO/EIT Observations at Temperatures of $(1.0-1.5) \times 10^6$ K, *Astrophys. J.*, 515, 842–867
- Aschwanden, M. J., Alexander, D., Hurlburt, N., Newmark, J. S., Neupert, W. M., Klimchuk, J. A., Gary, G. A., 2000a, Three-dimensional Stereoscopic Analysis of Solar Active Region Loops. II. SOHO/EIT Observations at Temperatures of 1.5-2.5 MK, *Astrophys. J.*, 531, 1129–1149
- Aschwanden, M. J., Nightingale, R. W., Alexander, D., 2000b, Evidence for Nonuniform Heating of Coronal Loops Inferred from Multithread Modeling of TRACE Data, *Astrophys. J.*, 541, 1059–1077
- Aschwanden, M. J., Schrijver, C. J., Alexander, D., 2001, Modeling of Coronal EUV Loops Observed with TRACE. I. Hydrostatic Solutions with Nonuniform Heating, *Astrophys. J.*, 550, 1036–1050
- Axford, W. I., McKenzie, J. F., 1995, The origin of the solar wind, in *Solar Wind Eight*, pp. 31–+
- Axford, W. I., McKenzie, J. F., Sukhorukova, G. V., Banaszekiewicz, M., Czechowski, A., Ratkiewicz, R., 1999, Acceleration of the High Speed Solar Wind in Coronal Holes, *Space Science Reviews*, 87, 25–41
- Banaszkiewicz, M., Axford, W. I., McKenzie, J. F., 1998, An analytic solar magnetic field model, *Astron. Astrophys.*, 337, 940–944
- Baumjohann, W., Treuman, R. A., 1996, *Basic of Space Plasma Physics*, Imperial College Press
- Benz, A., 2003, *Kinetic Processes in Solar and Stellar Coronae*, Kluwer Academic Publishers, Dordrecht, The Netherlands.

Bibliography

- Berger, M. A., 1991, Generation of coronal magnetic fields by random surface motions. I - Mean square twist and current density, *Astron. Astrophys.*, 252, 369–376
- Berger, M. A., 1993, Energy-crossing number relations for braided magnetic fields, *Physical Review Letters*, 70, 705–708
- Berger, T. E., Title, A. M., 1996, On the Dynamics of Small-Scale Solar Magnetic Elements, *Astrophys. J.*, 463, 365–+
- Biskamp, D., Müller, W.-C., 2000, Scaling properties of three-dimensional isotropic magnetohydrodynamic turbulence, *Physics of Plasmas*, 7, 4889–4900
- Bourouaine, S., Vocks, C., Marsch, E., 2008a, Coronal Loop Model Including Ion Kinetics, *Astrophys. J.*, 676, 1346–1355
- Bourouaine, S., Vocks, C., Marsch, E., 2008b, Multi-Ion Kinetic Model for Coronal Loop, *Astrophys. J. Lett.*, 680, L77–L80
- Braginskii, S. I., 1965, Transport Processes in a Plasma, *Reviews of Plasma Physics*, 1, 205–+
- Brković, A., Landi, E., Landini, M., Rüedi, I., Solanki, S. K., 2002, Models for solar magnetic loops. II. Comparison with SOHO-CDS observations on the solar disk, *Astron. Astrophys.*, 383, 661–677
- Brosius, J. W., Davila, J. M., Thomas, R. J., Monsignori-Fossi, B. C., 1996, Measuring Active and Quiet-Sun Coronal Plasma Properties with Extreme-Ultraviolet Spectra from SERTS, *Astrophys. J. Suppl. Series*, 106, 143–+
- Cargill, P. J., 1994, Some implications of the nanoflare concept, *Astrophys. J.*, 422, 381–393
- Cargill, P. J., Klimchuk, J. A., 1997, A Nanoflare Explanation for the Heating of Coronal Loops Observed by YOHKOH, *Astrophys. J.*, 478, 799–+
- Cargill, P. J., Klimchuk, J. A., 2004, Nanoflare Heating of the Corona Revisited, *Astrophys. J.*, 605, 911–920
- Chae, J., Wang, H., Qiu, J., Goode, P. R., Wilhelm, K., 2000, Active Region Loops Observed with SUMER on Board the SOHO, *Astrophys. J.*, 533, 535–545
- Cirtain, J. W., Del Zanna, G., DeLuca, E. E., Mason, H. E., Martens, P. C. H., Schmelz, J. T., 2007, Active Region Loops: Temperature Measurements as a Function of Time from Joint TRACE and SOHO CDS Observations, *Astrophys. J.*, 655, 598–605
- Cranmer, S. R., 2000, Ion Cyclotron Wave Dissipation in the Solar Corona: The Summed Effect of More than 2000 Ion Species, *Astrophys. J.*, 532, 1197–1208
- Cranmer, S. R., 2001, Ion cyclotron diffusion of velocity distributions in the extended solar corona, *J. Geophys. Res.*, 106, 24 937–24 954

- Cranmer, S. R., van Ballegooijen, A. A., 2003, Alfvénic Turbulence in the Extended Solar Corona: Kinetic Effects and Proton Heating, *Astrophys. J.*, 594, 573–591, arXiv: astro-ph/0305134
- Cranmer, S. R., van Ballegooijen, A. A., 2005, On the Generation, Propagation, and Reflection of Alfvén Waves from the Solar Photosphere to the Distant Heliosphere, *Astrophys. J. Suppl. Series*, 156, 265–293, arXiv: astro-ph/0410639
- Cranmer, S. R., Field, G. B., Kohl, J. L., 1999a, Spectroscopic Constraints on Models of Ion-cyclotron Resonance Heating in the Polar Solar Corona, *Space Science Reviews*, 87, 149–152
- Cranmer, S. R., Field, G. B., Kohl, J. L., 1999b, Spectroscopic Constraints on Models of Ion Cyclotron Resonance Heating in the Polar Solar Corona and High-Speed Solar Wind, *Astrophys. J.*, 518, 937–947
- Cranmer, S. R., Kohl, J. L., Noci, G., Antonucci, E., Tondello, G., Huber, M. C. E., Strachan, L., Panasyuk, A. V., Gardner, L. D., Romoli, M., Fineschi, S., Dobrzycka, D., Raymond, J. C., Nicolosi, P., Siegmund, O. H. W., Spadaro, D., Benna, C., Ciavarella, A., Giordano, S., Habbal, S. R., Karovska, M., Li, X., Martin, R., Michels, J. G., Modigliani, A., Naletto, G., O’Neal, R. H., Pernechele, C., Poletto, G., Smith, P. L., Suleiman, R. M., 1999c, An Empirical Model of a Polar Coronal Hole at Solar Minimum, *Astrophys. J.*, 511, 481–501
- Dahlburg, R. B., Klimchuk, J. A., Antiochos, S. K., 2003, Coronal energy release via ideal three-dimensional instability three-dimensional instability, *Advances in Space Research*, 32, 1029–1034
- Dahlburg, R. B., Klimchuk, J. A., Antiochos, S. K., 2005, An Explanation for the “Switch-On” Nature of Magnetic Energy Release and Its Application to Coronal Heating, *Astrophys. J.*, 622, 1191–1201
- De Pontieu, B., McIntosh, S. W., Carlsson, M., Hansteen, V. H., Tarbell, T. D., Schrijver, C. J., Title, A. M., Shine, R. A., Tsuneta, S., Katsukawa, Y., Ichimoto, K., Suematsu, Y., Shimizu, T., Nagata, S., 2007, Chromospheric Alfvénic Waves Strong Enough to Power the Solar Wind, *Science*, 318, 1574–
- Dolla, L., Solomon, J., 2008, Solar off-limb line widths: Alfvén waves, ion-cyclotron waves, and preferential heating, *Astron. Astrophys.*, 483, 271–283, 0804. 2987
- Fontenla, J. M., Avrett, E. H., Loeser, R., 1990, Energy balance in the solar transition region. I - Hydrostatic thermal models with ambipolar diffusion, *Astrophys. J.*, 355, 700–718
- Frazin, R. A., Cranmer, S. R., Kohl, J. L., 2003, Empirically Determined Anisotropic Velocity Distributions and Outflows of O^{5+} Ions in a Coronal Streamer at Solar Minimum, *Astrophys. J.*, 597, 1145–1157
- Gabriel, J. H., 1976, , *Phil. Trans. R. Soc. Lond. A.*, 281

Bibliography

- Galsgaard, K., Nordlund, Å., 1996, Heating and activity of the solar corona 1. Boundary shearing of an initially homogeneous magnetic field, *J. GeoPhys. Res.*, 101, 13 445–13 460
- Gary, G. A., 2001, Plasma Beta above a Solar Active Region: Rethinking the Paradigm, *Sol. Phys.*, 203, 71–86
- Gary, S. P., Borovsky, J. E., 2004, Alfvén-cyclotron fluctuations: Linear Vlasov theory, *Journal of Geophysical Research (Space Physics)*, 109, 6105–+
- Golub, L., Nystrom, G., Herant, M., Kalata, K., Lovas, I., 1990, Sub-arcsecond observations of the solar X-ray corona, *Nature*, 344, 842–844
- Grall, R. R., Coles, W. A., Klingsmith, M. T., Breen, A. R., Williams, P. J. S., Markkanen, J., Esser, R., 1996, Rapid acceleration of the polar solar wind, *Nature*, 379, 429–+
- Habbal, S. R., Ronan, R., Withbroe, G. L., 1985, Spatial and temporal variations of solar coronal loops, *Sol. Phys.*, 98, 323–340
- Helander, P., Sigmar, D. J., 2002, Collisional Transport in Magnetized Plasmas
- Heuer, M., Marsch, E., 2007, Diffusion plateaus in the velocity distributions of fast solar wind protons, *Journal of Geophysical Research (Space Physics)*, 112, 3102–+
- Heyvaerts, J., Priest, E. R., 1983, Coronal heating by phase-mixed shear Alfvén waves, *Astron. Astrophys.*, 117, 220–234
- Hollweg, J. V., 1986, Transition region, corona, and solar wind in coronal holes, *J. GeoPhys. Res.*, 91, 4111–4125
- Hollweg, J. V., 1999a, Potential wells, the cyclotron resonance, and ion heating in coronal holes, *J. GeoPhys. Res.*, 104, 505–520
- Hollweg, J. V., 1999b, Cyclotron resonance in coronal holes: 2. A two-proton description, *J. GeoPhys. Res.*, 104, 24 793–24 806
- Hollweg, J. V., 1999c, Kinetic Alfvén wave revisited, *J. GeoPhys. Res.*, 104, 14 811–14 820
- Hollweg, J. V., 2000, Cyclotron resonance in coronal holes: 3. A five-beam turbulence-driven model, *J. GeoPhys. Res.*, 105, 15 699–15 714
- Hood, A. W., Gonzalez-Delgado, D., Ireland, J., 1997a, Heating of coronal loops by phase-mixing., *Astron. Astrophys.*, 324, 11–14
- Hood, A. W., Ireland, J., Priest, E. R., 1997b, Heating of coronal holes by phase mixing., *Astron. Astrophys.*, 318, 957–962
- Hu, Y. Q., Habbal, S. R., Li, X., 1999, On the cascade processes of Alfvén waves in the fast solar wind, *J. GeoPhys. Res.*, 104, 24 819–+

- Ji, H., Carter, T., Hsu, S., Yamada, M., 2001, Study of local reconnection physics in a laboratory plasma, *Earth, Planets, and Space*, 53, 539–543
- Kano, R., Tsuneta, S., 1996, Temperature Distributions and Energy Scaling Law of Solar Coronal Loops Obtained with YOHKOH, *Pub. Astron. Soc. Japan*, 48, 535–543
- Klimchuk, J. A., 2000, Cross-Sectional Properties of Coronal Loops, *Sol. Phys.*, 193, 53–75
- Klimchuk, J. A., 2006, On Solving the Coronal Heating Problem, *Sol. Phys.*, 234, 41–77, [arXiv:astro-ph/0511841](#)
- Klimchuk, J. A., Cargill, P. J., 2001, Spectroscopic Diagnostics of Nanoflare-heated Loops, *Astrophys. J.*, 553, 440–448
- Klimchuk, J. A., Tanner, S. E. M., De Moortel, I., 2004, Coronal Seismology and the Propagation of Acoustic Waves along Coronal Loops, *Astrophys. J.*, 616, 1232–1241, [arXiv:astro-ph/0412085](#)
- Kohl, J. L., Noci, G., Antonucci, E., Tondello, G., Huber, M. C. E., Gardner, L. D., Nicolosi, P., Strachan, L., Fineschi, S., Raymond, J. C., Romoli, M., Spadaro, D., Panasyuk, A., Siegmund, O. H. W., Benna, C., Ciaravella, A., Cranmer, S. R., Giordano, S., Karovska, M., Martin, R., Michels, J., Modigliani, A., Naletto, G., Pernechele, C., Poletto, G., Smith, P. L., 1997, First Results from the SOHO Ultraviolet Coronagraph Spectrometer, *Sol. Phys.*, 175, 613–644
- Kohl, J. L., Noci, G., Antonucci, E., Tondello, G., Huber, M. C. E., Cranmer, S. R., Strachan, L., Panasyuk, A. V., Gardner, L. D., Romoli, M., Fineschi, S., Dobrzycka, D., Raymond, J. C., Nicolosi, P., Siegmund, O. H. W., Spadaro, D., Benna, C., Ciaravella, A., Giordano, S., Habbal, S. R., Karovska, M., Li, X., Martin, R., Michels, J. G., Modigliani, A., Naletto, G., O’Neal, R. H., Pernechele, C., Poletto, G., Smith, P. L., Suleiman, R. M., 1998, UVCS/SOHO Empirical Determinations of Anisotropic Velocity Distributions in the Solar Corona, *Astrophys. J. Lett.*, 501, L127+
- Landi, E., Landini, M., 2004, Models for Solar Magnetic Loops. III. Dynamic Models and Coronal Diagnostic Spectrometer Observations, *Astrophys. J.*, 608, 1133–1147
- Lenz, D. D., Deluca, E. E., Golub, L., Rosner, R., Bookbinder, J. A., 1999, Temperature and Emission-Measure Profiles along Long-lived Solar Coronal Loops Observed with the Transition Region and Coronal Explorer, *Astrophys. J. Lett.*, 517, L155–L158, [arXiv:astro-ph/9903491](#)
- Li, X., Habbal, S. R., 2001, Damping of fast and ion cyclotron oblique waves in the multi-ion fast solar wind, *J. Geophys. Res.*, 106, 10 669–10 680
- Li, X., Habbal, S. R., 2003, Coronal Loops Heated by Turbulence-driven Alfvén Waves, *Astrophys. J. Lett.*, 598, L125–L128
- Li, X., Habbal, S. R., Kohl, J., Noci, G., 1998, The Effect of Temperature Anisotropy on Observations of Doppler Dimming and Pumping in the Inner Corona, *Astrophys. J. Lett.*, 501, L133+, [arXiv:astro-ph/9805021](#)

Bibliography

- Li, X., Habbal, S. R., Hollweg, J. V., Esser, R., 1999, Heating and cooling of protons by turbulence-driven ion cyclotron waves in the fast solar wind, *J. Geophys. Res.*, 104, 2521–2536
- Li, X., Lu, Q., Li, B., 2007, Ion Pickup by Finite Amplitude Parallel Propagating Alfvén Waves, *Astrophys. J. Lett.*, 661, L105–L108, [arXiv:astro-ph/0703683](https://arxiv.org/abs/astro-ph/0703683)
- Lopez Fuentes, M. C., Mandrini, C. H., Klimchuk, J. A., 2004, Evolution of Coronal Loops Observed by GOES-SXI, in *Bulletin of the American Astronomical Society*, vol. 36 of *Bulletin of the American Astronomical Society*, pp. 761–+
- López Fuentes, M. C., Klimchuk, J. A., Démoulin, P., 2006, The Magnetic Structure of Coronal Loops Observed by TRACE, *Astrophys. J.*, 639, 459–474, [arXiv:astro-ph/0507462](https://arxiv.org/abs/astro-ph/0507462)
- López Fuentes, M. C., Démoulin, P., Klimchuk, J. A., 2008, Are Constant Loop Widths an Artifact of the Background and the Spatial Resolution?, *Astrophys. J.*, 673, 586–597, [0704.0637](https://arxiv.org/abs/0704.0637)
- Marsch, E., 1998, Closure of multi-fluid and kinetic equations for cyclotron-resonant interactions of solar wind ions with Alfvén waves, *Nonlinear Processes in Geophysics*, 5, 111–120
- Marsch, E., 2002, On resonant interactions of ions with plasma waves in a reduced quasi-linear theory, *Nonlinear Processes in Geophysics*, 9, 69–74
- Marsch, E., 2006, Kinetic Physics of the Solar Corona and Solar Wind, *Living Reviews in Solar Physics*, 3, 1–+
- Marsch, E., Tu, C.-Y., 1990, On the radial evolution of MHD turbulence in the inner heliosphere, *J. Geophys. Res.*, 95, 8211–8229
- Marsch, E., Tu, C.-Y., 1997, Solar Wind and Chromospheric Network, *Sol. Phys.*, 176, 87–106
- Marsch, E., Tu, C.-Y., 2001, Heating and acceleration of coronal ions interacting with plasma waves through cyclotron and Landau resonance, *J. Geophys. Res.*, 106, 227–238
- Marsch, E., Wiegmann, T., Xia, L. D., 2004, Coronal plasma flows and magnetic fields in solar active regions. Combined observations from SOHO and NSO/Kitt Peak, *Astron. Astrophys.*, 428, 629–645
- Martens, P. C. H., Cirtain, J. W., Schmelz, J. T., 2002, The Inadequacy of Temperature Measurements in the Solar Corona through Narrowband Filter and Line Ratios, *Astrophys. J. Lett.*, 577, L115–L117
- Mecheri, R., Marsch, E., 2007, Coronal ion-cyclotron beam instabilities within the multi-fluid description, *Astron. Astrophys.*, 474, 609–615, [0706.0752](https://arxiv.org/abs/0706.0752)

- Mecheri, R., Marsch, E., 2008, Drift instabilities in the solar corona within the multi-fluid description, *Astron. Astrophys.*, 481, 853–860, 0802.0340
- Mendoza-Briceño, C. A., Erdélyi, R., Di G. Sigalotti, L., 2002, Coronal Loop Heating by Random Energy Releases, *Astrophys. J. Lett.*, 579, L49–L52
- Muller, R., Roudier, T., Vigneau, J., Auffret, H., 1994, The proper motion of network bright points and the heating of the solar corona, *Astron. Astrophys.*, 283, 232–240
- Nakariakov, V. M., Ofman, L., Deluca, E. E., Roberts, B., Davila, J. M., 1999, TRACE observation of damped coronal loop oscillations: Implications for coronal heating, *Science*, 285, 862–864
- Narain, U., Ulmschneider, P., 1996, Chromospheric and Coronal Heating Mechanisms II, *Space Science Reviews*, 75, 453–509
- Ofman, L., 2005, MHD Waves and Heating in Coronal Holes, *Space Science Reviews*, 120, 67–94
- Ofman, L., Davila, J. M., Steinolfson, R. S., 1994, Coronal heating by the resonant absorption of Alfvén waves: The effect of viscous stress tensor, *Astrophys. J.*, 421, 360–371
- Ofman, L., Davila, J. M., Steinolfson, R. S., 1995, Coronal heating by the resonant absorption of Alfvén waves: Wavenumber scaling laws., *Astrophys. J.*, 444, 471–477
- Ofman, L., Nakariakov, V. M., Deforest, C. E., 1999, Slow Magnetosonic Waves in Coronal Plumes, *Astrophys. J.*, 514, 441–447
- Ofman, L., Viñas, A., Gary, S. P., 2001, Constraints on the O^{+5} Anisotropy in the Solar Corona, *Astrophys. J. Lett.*, 547, L175–L178
- Ofman, L., Gary, S. P., Viñas, A., 2002, Resonant heating and acceleration of ions in coronal holes driven by cyclotron resonant spectra, *Journal of Geophysical Research (Space Physics)*, 107, 1461–+
- O’Neill, I., Li, X., 2005, Coronal loops heated by turbulence-driven Alfvén waves: A two fluid model, *Astron. Astrophys.*, 435, 1159–1167
- Parker, E. N., 1988, Nanoflares and the solar X-ray corona, *Astrophys. J.*, 330, 474–479
- Pasachoff, J. M., Kimmel, S. B., Druckmüller, M., Rušin, V., Saniga, M., 2006, The April 8, 2005, Eclipse White-Light Corona, *Sol. Phys.*, 238, 261–270
- Patsourakos, S., Klimchuk, J. A., MacNeice, P. J., 2004, The Inability of Steady-Flow Models to Explain the Extreme-Ultraviolet Coronal Loops, *Astrophys. J.*, 603, 322–329
- Petrie, G. J. D., 2006, Coronal Loop Widths and Pressure Scale Heights, *Astrophys. J.*, 649, 1078–1083, arXiv:astro-ph/0607011

Bibliography

- Priest, E. R., 1984, Solar magneto-hydrodynamics, Geophysics and Astrophysics Monographs, Dordrecht: Reidel, 1984
- Reeves, K. K., Warren, H. P., 2002, Modeling the Cooling of Postflare Loops, *Astrophys. J.*, 578, 590–597
- Rosenbluth, M. N., MacDonald, W. M., Judd, D. L., 1957, Fokker-Planck Equation for an Inverse-Square Force, *Physical Review*, 107, 1–6
- Rosner, R., Tucker, W. H., Vaiana, G. S., 1978, Dynamics of the quiescent solar corona, *Astrophys. J.*, 220, 643–645
- Schmelz, J. T., Scopes, R. T., Cirtain, J. W., Winter, H. D., Allen, J. D., 2001, Observational Constraints on Coronal Heating Models Using Coronal Diagnostics Spectrometer and Soft X-Ray Telescope Data, *Astrophys. J.*, 556, 896–904
- Schmelz, J. T., Beene, J. E., Nasraoui, K., Blevins, H. T., Martens, P. C. H., Cirtain, J. W., 2003, The Effect of Background Subtraction on the Temperature of EIT Coronal Loops, *Astrophys. J.*, 599, 604–614
- Schmelz, J. T., Nasraoui, K., Richardson, V. L., Hubbard, P. J., Nevels, C. R., Beene, J. E., 2005, All Coronal Loops Are the Same: Evidence to the Contrary, *Astrophys. J. Lett.*, 627, L81–L84, [arXiv:astro-ph/0505593](https://arxiv.org/abs/astro-ph/0505593)
- Schrijver, C. J., Title, A. M., Berger, T. E., Fletcher, L., Hurlburt, N. E., Nightingale, R. W., Shine, R. A., Tarbell, T. D., Wolfson, J., Golub, L., Bookbinder, J. A., Deluca, E. E., McMullen, R. A., Warren, H. P., Kankelborg, C. C., Handy, B. N., de Pontieu, B., 1999, A new view of the solar outer atmosphere by the Transition Region and Coronal Explorer, *Sol. Phys.*, 187, 261–302
- Serio, S., Peres, G., Vaiana, G. S., Golub, L., Rosner, R., 1981, Closed coronal structures. II - Generalized hydrostatic model, *Astrophys. J.*, 243, 288–300
- Sheeley, Jr., N. R., 1980, Temporal variations of loop structures in the solar atmosphere, *Sol. Phys.*, 66, 79–87
- Spadaro, D., Lanza, A. F., Lanzafame, A. C., Karpen, J. T., Antiochos, S. K., Klimchuk, J. A., MacNeice, P. J., 2003, A Transient Heating Model for Coronal Structure and Dynamics, *Astrophys. J.*, 582, 486–494
- Stein et al., 1991, *Mechanisms of Chromospheric and Coronal Heating*, Springer-Verlag, Berlin
- Stix, T. H., 1992, *Waves in Plasmas*, Waves in Plasmas, New York: American Institute of Physics
- Telloni, D., Antonucci, E., Dodero, M. A., 2007, Outflow velocity of the O⁺⁵ ions in polar coronal holes out to 5 R_ò, *Astron. Astrophys.*, 472, 299–307

- Testa, P., Peres, G., Reale, F., Orlando, S., 2002, Temperature and Density Structure of Hot and Cool Loops Derived from the Analysis of TRACE Data, *Astrophys. J.*, 580, 1159–1171
- Testa, P., Peres, G., Reale, F., 2005, Emission Measure Distribution in Loops Impulsively Heated at the Footpoints, *Astrophys. J.*, 622, 695–703, [arXiv:astro-ph/0412482](https://arxiv.org/abs/astro-ph/0412482)
- Tomczyk, S., McIntosh, S. W., Keil, S. L., Judge, P. G., Schad, T., Seeley, D. H., Edmondson, J., 2007, Alfvén Waves in the Solar Corona, *Science*, 317, 1192–
- Tu, C.-Y., 1987, A solar wind model with the power spectrum of Alfvénic fluctuations, *Sol. Phys.*, 109, 149–186
- Tu, C.-Y., 1988, The damping of interplanetary Alfvénic fluctuations and the heating of the solar wind, *J. Geophys. Res.*, 93, 7–20
- Tu, C.-Y., Marsch, E., 1997, Two-Fluid Model for Heating of the Solar Corona and Acceleration of the Solar Wind by High-Frequency Alfvén Waves, *Sol. Phys.*, 171, 363–391
- Ulmschneider, P., Kalkofen, W., 2003, Heating of the solar chromosphere, Cambridge University Press, Cambridge, U.K
- Ulrich, R. K., 1996, Observations of Magnetohydrodynamic Oscillations in the Solar Atmosphere with Properties of Alfvén Waves, *Astrophys. J.*, 465, 436–
- Vesecy, J. F., Antiochos, S. K., Underwood, J. H., 1979, Numerical modeling of quasi-static coronal loops. I - Uniform energy input, *Astrophys. J.*, 233, 987–997
- Vocks, C., Thesis: Ein kinetisches Modell der Ionen in koronalen Lochern mit Welle-Teilchen-Wechselwirkung und Coulomb -Stoessen. ISBN 3-89744-159-4
- Vocks, C., 2002, A Kinetic Model for Ions in the Solar Corona Including Wave-Particle Interactions and Coulomb Collisions, *Astrophys. J.*, 568, 1017–1029
- Vocks, C., Marsch, E., 2001, A semi-kinetic model of wave-ion interaction in the solar corona, *Geophys. Res. Lett.*, 28, 1917–1920
- Vocks, C., Marsch, E., 2002, Kinetic Results for Ions in the Solar Corona with Wave-Particle Interactions and Coulomb Collisions, *Astrophys. J.*, 568, 1030–1042
- Voitenko, Y., Goossens, M., 2000a, Nonlinear decay of phase-mixed Alfvén waves in the solar corona, *Astron. Astrophys.*, 357, 1073–1085
- Voitenko, Y., Goossens, M., 2000b, Competition of damping mechanisms for the phase-mixed Alfvén waves in the solar corona, *Astron. Astrophys.*, 357, 1086–1092
- von Steiger, R., Geiss, J., Gloeckler, G., Galvin, A. B., 1995, Kinetic Properties of Heavy Ions in the Solar Wind From SWICS/Ulysses, *Space Science Reviews*, 72, 71–76
- Walsh, R. W., Bell, G. E., Hood, A. W., 1997, Discrete Random Heating Events in Coronal Loops, *Sol. Phys.*, 171, 81–91

Bibliography

- Wang, C. B., Wu, C. S., Yoon, P. H., 2006, Heating of Ions by Alfvén Waves via Nonresonant Interactions, *Physical Review Letters*, 96, 125 001–+
- Warren, H. P., Winebarger, A. R., Hamilton, P. S., 2002, Hydrodynamic Modeling of Active Region Loops, *Astrophys. J. Lett.*, 579, L41–L44
- Warren, H. P., Ugarte-Urra, I., Doschek, G. A., Brooks, D. H., Williams, D. R., 2008, Observations of Active Region Loops with the EUV Imaging Spectrometer on Hinode, *Astrophys. J. Lett.*, 686, L131–L134, 0808. 3227
- Watko, J. A., Klimchuk, J. A., 2000, Width Variations along Coronal Loops Observed by TRACE, *Sol. Phys.*, 193, 77–92
- Weber, M. A., Schmelz, J. T., DeLuca, E. E., Roames, J. K., 2005, Isothermal Bias of the “Filter Ratio” Method for Observations of Multithermal Plasma, *Astrophys. J. Lett.*, 635, L101–L104
- Wiegelmann, T., Inhester, B., Sakurai, T., 2006, Preprocessing of Vector Magnetograph Data for a Nonlinear Force-Free Magnetic Field Reconstruction, *Sol. Phys.*, 233, 215–232, [arXiv:astro-ph/0612641](https://arxiv.org/abs/astro-ph/0612641)
- Wilhelm, K., Marsch, E., Dwivedi, B. N., Hassler, D. M., Lemaire, P., Gabriel, A. H., Huber, M. C. E., 1998, The Solar Corona above Polar Coronal Holes as Seen by SUMER on SOHO, *Astrophys. J.*, 500, 1023–+
- Wilhelm, K., Marsch, E., Dwivedi, B. N., Feldman, U., 2007, Observations of the Sun at Vacuum-Ultraviolet Wavelengths from Space. Part II: Results and Interpretations, *Space Science Reviews*, 133, 103–179
- Winebarger, A. R., Warren, H., van Ballegooijen, A., DeLuca, E. E., Golub, L., 2002, Steady Flows Detected in Extreme-Ultraviolet Loops, *Astrophys. J. Lett.*, 567, L89–L92
- Winebarger, A. R., Warren, H. P., Mariska, J. T., 2003a, Transition Region and Coronal Explorer and Soft X-Ray Telescope Active Region Loop Observations: Comparisons with Static Solutions of the Hydrodynamic Equations, *Astrophys. J.*, 587, 439–449
- Winebarger, A. R., Warren, H. P., Seaton, D. B., 2003b, Evolving Active Region Loops Observed with the Transition Region and Coronal Explorer. I. Observations, *Astrophys. J.*, 593, 1164–1173
- Wu, C. S., Yoon, P. H., 2007, Proton Heating via Nonresonant Scattering Off Intrinsic Alfvénic Turbulence, *Physical Review Letters*, 99, 075 001–+

Acknowledgements

My first words are dedicated to my parents who have always encouraged and supported me with their continuing wishes for a successful completion of my Ph.D. thesis.

My special thanks to my supervisor Prof. Eckart Marsch for his support and valuable advises. Thanks to the fruitful discussions with him I could achieve the fulfillment of this work in very nice conditions. Also, I would like to thank my supervisor Prof. Wolfgang Glatzel at Goettingen University for his valuable help and for accepting me to be his Ph.D student.

I would like to thank the Max Planck Institute for Solar System Research (MPS) and the International Max Planck Research School (IMPRS) for giving me the opportunity and the financial support to carry out this thesis work.

I will not forget also the enjoyable days I have spent at the Astrophysical Institute of Potsdam working with Dr. Christian Vocks, I am very grateful to all the staff there, Prof. G. Mann, Prof. H. Aurass, Dr. R. Miteva, and H. Önel.

My friends at the Max Planck Institute have helped me enormously to make the life in Lindau very enjoyable, many thanks to my algerian friends Redouane, Khalil, Lotfi, Yacine, Amine. Also, many thanks to my best friends (brothers), Philippe and Michal, I will never forget the beautiful time that we have spent together. I would like to thank all the administration staff of the Max-Planck Institute, especially Frau Bierwirth and Frau Fahlbusch and Julia Müller for their enormous efforts, help and permanent availability.

I express my special gratitude to Dr. Dieter Schmitt for his substantial efforts to make the IMPRS successful and to create a nice scientific and social environment for the students.

Finally, I am happy to dedicate my thesis work to all my family, my sisters and brothers.

Scientific contributions

Conference contributions :

[1] **Bourouaine, S.** & Marsch, E. 2008, Solar-Cycle 24 meeting, NAPA, "*Multi-Strand Coronal Loop Model and Filter-Ratio Analysis*".

[2] **Bourouaine, S.** & Marsch, E. 2008, Solar-Cycle 24 meeting, NAPA, "*Multi-Ion Coronal Loop Model*".

[3] **Bourouaine, S.**, Marsch, E. & Vocks, C. 2008, DPG meeting, Freiburg, "*Semi-Kinetic Model for Coronal Loop*".

Publications in refereed journals :

[1] **Bourouaine, S.**, Marsch, E. & Vocks, C. 2008, ApJL, 684, L119, "*On the Efficiency of Ion Heating by Coronal Alfvén Waves*".

[2] **Bourouaine, S.**, Vocks, C. & Marsch, E. 2008, ApJL, 680, L77, "*Multi-Ion Kinetic Model for Coronal Loop*".

[3] **Bourouaine, S.**, Vocks, C. & Marsch, E. 2008, ApJ, 676, 1346, "*Coronal Loop Modelling Including Ion Kinetic*".

[4] **Bourouaine, S.** & Benslama, A. 2007, Phys. Lett. B (PLB), 650, 90, "*MHD waves within Noncommutative Maxwell Theory*".

[5] **Bourouaine, S.** & Benslama, A. 2005, Journal of Phys. A (JPhA), 38, 7397, "*Noncommutative Quantum Electrodynamics in Path Integral Framework*".

[6] **Bourouaine, S.** 2005, Eur. Journal of Physics C (EPJC), 44, 131, "*Dirac particle in the Presence of a Plane-wave and Constant Magnetic Fields: Path Integral Approach*".

[7] **Bourouaine, S.** & Benslama, A. 2005, Modern Phys. Lett. A (MPLA), 20, 1997, "*Influence of Gravity on Noncommutative Dirac Equation*".

[8] **Bourouaine, S.** 2005, Annalen der Phys., 14, 207, "*Dirac particle in a Plane-wave Field and the Semi-classical Approximation*".

Lebenslauf

Persönliche Daten

Name: Sofiane Bourouaine
Geburtstag: 25.06.1977
Geburtssort: Constantine, Algerien
Staatsbürgerschaft: Algerisch

Schulbildung

09/1983-06/1991: Lycée (Gymnasium) und abschliessendes
Bacalaureate (Abitur) mit Intensivkurs Mathematik,
Constantine, Algerien

Studium

09/1994-06/1999: Diplom in Physik, Arbeit in Theoretische Physik,
Mentouri Universität, Constantine, Algerien
09/1999-06/2002: Magister in Physik, Arbeit in Theoretische Physik,
Mentouri Universität, Constantine, Algerien

Promotion

02/2006-02/2009: Doktorarbeit am dem Max-Planck-Institut für
Sonnensystemforschung, Katlenburg-Lindau,
und der George-August Universitäts, Göttingen.